UNIVERSITY OF OKLAHOMA

GRADUATE COLLEGE

# Multiwavelength Analyses of a Small Sample of Nearby Spiral Galaxies: The Radio and X-Ray Connection

A Dissertation

Submitted to the Graduate Faculty

in partial fullfillment of the requirements for the

degree of

Doctor of Philosophy

By

LARRY ALLEN MADDOX
Norman, Oklahoma
2006

Downloaded from SHAREOK. Persistent Handle URL: https://hdl.handle.net/11244/1076

UMI Number: 3222155

UMI®

UMI Microform 3222155

Copyright 2006 by ProQuest Information and Learning Company.
All rights reserved. This microform edition is protected against
unauthorized copying under Title 17, United States Code.

ProQuest Information and Learning Company
300 North Zeeb Road
P.O. Box 1346
Ann Arbor, MI 48106-1346

# Multiwavelength Analyses of a Small Sample of Nearby Spiral Galaxies: The Radio and X-Ray Connection

A Dissertation Approved for the
Homer L. Dodge Department of Physics and Astronomy

By

John J. Cowan (Chair)

Karen M. Leighly

David Branch

Deborah K. Watson

Rüdiger Landes (Department of Mathematics)

© Copyright LARRY ALLEN MADDOX, 2006
All Rights Reserved.

## Acknowledgements

There are many people who I would like to thank.

First of all, I would like to thank my family. While there are too many to name them all, I would like to name a few: My parents, Michael and Carol Maddox, my grandparents, Don and Marie Westman, and my sister, Michelle Renn. Without the constant badgering from these people, I would not have made it this far. Other family members I would like to thank are Donna and Mark Goodale, Brenda and Dwayne Strickland, and Charles Westman. So as not to leave out my father's relatives, I would like to thank Glenda Stage, Randy Maddox and Gary Maddox.

To my friends outside of the physics world: Jeremy and Heather Smith, Jay and Elizabeth Stone, Heather Moody-Hall, Jack Carter, Dianna LaFerry, and Mike Engle. I am sure that I have forgotten others, but they should not be offended.

To many classmates along the way that have felt my pain: Darrin Casebeer, Rollin Thomas, Jim Hicks, Isaac Hall, Aida Nava, Thushari Jayasekara, Bobby Fleshman, Hamed Baghepour, Bah'man Roosteai, Sebastien Bongard, Christopher Stockdale, Jackie Milingo, Taroshani Kasturiarachchi, Skankar Sachithanandam, Kuloth Shajesh, and Poopalasingam Sivakumar.

To various teachers and professors that I have learned from: Joanie Brown, Jenny Davis and Robin Roper (Cherokee High School); Cleon Dean, Marvin Payne, Mark Edwards, and Arthur Woodrum (Georgia Southern University); Will Burgett (University of Texas at Dallas); Eddie Baron, Dick Henry and Bill Romanishin (University of Oklahoma).

I have been lucky to work with many talented scientist during my time at OU: Andrea

Prestwich and Roy Kilgard (Harvard-Smithsonian Center for Astrophysics), Christina Lacey (University of South Carolina), Michael Rupen (National Radio Astronomy Observatory), Chiho Matsumoto (now at Nagoya University), Dirk Grupe (Penn State University) and Steven Tingay (Swinburne University of Technology).

I have also had many intersting and useful conversations with scientists over the years. These include: Joe Shields (Ohio University), Roger Chevalier (University of Virginia), Jay Lockman (NRAO, Charlottesville), Kristy Dyer (University of New Mexico), Casey Law (Northwestern University), Mike Crenshaw (Georgia State Unviersity), Mike Corcoran (Goddard Space Flight Center), Doug Schwarz (Marshall Space Flight Center), Knox Long (Space Telescope Science Institute), Bill Blair (Johns Hopkins University), Mike Eracleous (Penn State), and many more.

I especially like to thank my Doctoral Committee: Rüdiger Landes, Deborah Watson, David Branch, Karen Leighly, and John Cowan. Your support has meant a lot to me. Without it, I might not have completed my doctoral work.

# Contents

**Abstract** **xiii**

**1 Introduction** **1**
1.1 Background and Motivation . . . 1
1.2 X-Ray Sources in Normal Galaxies . . . 3
1.2.1 X-Ray Binaries . . . 3
1.2.2 Ultraluminous X-Ray Sources . . . 5
1.2.3 Source Classification . . . 5
1.3 Emission Mechanisms . . . 6
1.3.1 Thermal Bremsstrahlung . . . 6
1.3.2 Synchrotron Emission . . . 8
1.3.3 Inverse-Compton Emission . . . 9
1.4 The Sample . . . 10
1.4.1 M83 . . . 10
1.4.2 M51 . . . 12
1.4.3 M101 and NGC 3184 . . . 13
1.4.4 NGC 6300 . . . 17

**2 A Study of Compact Radio Sources in Nearby Face-on Spiral Galaxies. I. Long Term Evolution of M83** **20**
2.1 Introduction . . . 20
2.2 Observations and Data Reduction . . . 21
2.3 Data Analysis . . . 23
2.4 Discussion . . . 24
2.4.1 Radio Point Sources . . . 24
2.4.2 Nuclear Emission . . . 32
2.5 Conclusions . . . 34

**3 A Study of Compact Radio Sources in Nearby Face-on Spiral Galaxies. II. Multiwavelength Analyses of Sources in M51** **55**
3.1 Introduction . . . 55
3.2 Observations and Data Reduction . . . 56
3.3 Data Analysis . . . 57
3.4 Discussion . . . 58
3.4.1 Radio Point Sources . . . 58
3.4.2 Nuclear Emission . . . 65
3.5 Conclusions . . . 67

**4 A Study of Compact Radio Sources in Nearby Face-on Spiral Galaxies. III. Multiwavelength Analyses of M101 and NGC 3184** **93**
4.1 Introduction . . . 93
4.2 Data . . . 94
4.3 Reduction and Analysis . . . 96

4.4 Discussion . . . 96
4.4.1 M101 . . . 96
4.4.2 NGC 3184 . . . 99
4.5 Forthcoming Work . . . 100

**5 An *XMM-Newton* Observation of the Seyfert 2 Galaxy NGC 6300: II. Multiwavelength Analysis of Non-nuclear Sources 109**
5.1 Introduction . . . 109
5.1.1 Ringed, Barred Spiral Galaxies . . . 109
5.1.2 NGC 6300 . . . 110
5.2 Observations . . . 113
5.2.1 X-ray Observations . . . 113
5.2.2 Optical Imaging Observation . . . 114
5.2.3 Infrared Imaging Observation . . . 116
5.2.4 Radio Observations . . . 117
5.3 Multiwavelength Analysis . . . 119
5.3.1 X-ray Spectral Analysis . . . 119
5.3.2 Ultraviolet Analysis . . . 121
5.3.3 Optical Analysis . . . 123
5.3.4 IR Analysis . . . 123
5.3.5 Radio Analysis . . . 124
5.4 Results . . . 125
5.4.1 Source 1 . . . 125
5.4.2 Source 2 . . . 127
5.5 Conclusion and Future Work . . . 128

**6 Conclusions and Future Work 132**
6.1 M83 . . . 132
6.2 M51 . . . 133
6.3 M101 and NGC 3184 . . . 134
6.4 NGC 6300 . . . 134
6.5 General Conclusions . . . 135
6.6 Future Work . . . 136
6.7 Future Prospects in Radio Astronomy . . . 138

**Bibliography 140**

**A The Very Large Array and the Processing Radio Interferometry Observations 145**
A.1 The VLA . . . 145
A.2 Processing VLA Data . . . 147
A.3 AIPS History File . . . 158

**B The *Chandra* X-ray Observatory 178**
B.1 *ACIS*: the Advanced CCD Imaging Spectrometer . . . 179

**C Rules of Reasoning in Philosophy** **185**

# List of Tables


2.1 VLA Radio Observations of M83 . . . . . 36
2.2 Radio Positions and Peak Flux Densities of Sources in M83 . . . . . 37
2.2 Radio Positions and Peak Flux Densities of Sources in M83 . . . . . 38
2.3 Spectral Indices of Sources in M83 . . . . . 39
2.3 Spectral Indices of Sources in M83 . . . . . 40
2.3 Spectral Indices of Sources in M83 . . . . . 41
2.3 Spectral Indices of Sources in M83 . . . . . 42
2.4 Optical Supernova Remnants . . . . . 42
2.5 Radio Sources with Associated HII Regions . . . . . 43
2.5 Radio Sources with Associated HII Regions . . . . . 44
2.6 X-Ray Counterparts to Radio Sources in M83 . . . . . 45
2.7 Nuclear Mass Concentrations in M83 . . . . . 46

3.1 M51 Observations . . . . . 68
3.2 Positions, Flux Densities and Spectral Indices of Point Sources in M51 . . . 69
3.2 Positions, Flux Densities and Spectral Indices of Point Sources in M51 . . . 70
3.2 Positions, Flux Densities and Spectral Indices of Point Sources in M51 . . . 71
3.2 Positions, Flux Densities and Spectral Indices of Point Sources in M51 . . . 72
3.2 Positions, Flux Densities and Spectral Indices of Point Sources in M51 . . . 73
3.2 Positions, Flux Densities and Spectral Indices of Point Sources in M51 . . . 74
3.2 Positions, Flux Densities and Spectral Indices of Point Sources in M51 . . . 75
3.3 Excitation Parameters for H$\alpha$ Sources . . . . . 76
3.3 Excitation Parameters for H$\alpha$ Sources . . . . . 77
3.3 Excitation Parameters for H$\alpha$ Sources . . . . . 78
3.4 Properties of Coincident IR/UV/Radio Emission . . . . . 79
3.4 Properties of Coincident IR/UV/Radio Emission . . . . . 80
3.4 Properties of Coincident IR/UV/Radio Emission . . . . . 81
3.5 X-ray Counterparts to Radio Sources . . . . . 82

4.1 Observational Details, M101 . . . . . 95
4.2 Observational Details, NGC 3184 . . . . . 95
4.3 Fluxes and Spectral Indices of Point Sources in M101 . . . . . 98
4.3 Fluxes and Spectral Indices of Point Sources in M101 . . . . . 99
4.4 Flux Densities and Spectral Indices of Point Sources in NGC 3184 101

5.1 Model Fit Parameters for Sources 1 and 2 . . . . . 122
5.2 IRIS2 Upper Limits and Fluxes for Region Around Source 2 . . . . . 124

# List of Figures


1.1 Color-color classification scheme . . . . . 7
1.2 DSS image of M83. . . . . 12
1.3 DSS image of M51. . . . . 14
1.4 DSS image of M101. . . . . 15
1.5 DSS Image of NGC 3184 . . . . . 16
1.6 B-band image of NGC 6300 from the CTIO 1.5m. This image was used for reference in Ryder et al. (1996). The bar and ring structure is evident. Prominent dust lanes can be seen lacing through the ring. . . . . 17

2.1 Sources in M83 . . . . . 47
2.2 Contours of M83 . . . . . 48
2.3 Time Evolution of SN 1957D . . . . . 49
2.4 Time Evolution of SN 1950B . . . . . 50
2.5 X-ray color-color diagram for M83 . . . . . 51
2.6 Nuclear 20cm Contours . . . . . 52
2.7 Profile Plot of M83 Nucleus . . . . . 53
2.8 Optical and Hidden Nucleus . . . . . 54

3.1 Radio images of M51 . . . . . 83
3.2 Three color optical image of M51 from HST/ACS. *Image Credit:* NASA, ESA, S. Beckwith, and The Hubble Heritage Team (STScI/AURA) . . . . . 84
3.3 I Band image of M51 with radio sources overlayed. The radio sources have been binned according to their spectral index: steep spectrum sources in green, flat spectrum sources in yellow, inverted spectrum sources in blue, and indeterminate flat/steep spectrum sources in red. . . . . 85
3.4 A DSS optical image of M51. The crosses indicate the positions of the historical supernovae in the galaxy . . . . . 86
3.5 Radio contours of 6 cm emission overlayed on an optical HST image of the central 3.7 kpc M51. The position of SN 1994I is marked. . . . . 87
3.6 Blowup of a small area within M51. The H II image shows the positions of radio sources, indicated by circles, associated with optical emission. Two of the H II sources indicate shell structure indicative of SNRs. The remaining images show no shell emission. The emission in the other optical bands are predominantly due to starlight. . . . . 88
3.7 Many sources, like source 89 shown above lie in dense stellar clusters. Source 89 (circled in the H II image) is a flat spectrum radio source which is coincident with a large H II region. In I, V, and B bands it is quite evident that the photoionization of the H$\alpha$ cloud is powered by the stars in the cluster. . 89
3.8 Model Color-color diagram . . . . . 90
3.9 M51 Color-color diagram . . . . . 91
3.10 An enlargement of the nuclear region of M51. The colors represent X-ray emission, while the contours represent 20 cm radio emission. The smallest point-like feature in each image is $\sim 1.0''$. Overlay of 20 cm contours onto X-ray emission from the nucleus of M51. . . . . 92

4.1 20 cm Radio map for M101. Greyscale is linear from -1 to 500 $\mu$Jy. . . . . 103
4.2 Same as Figure 4.1 for NGC 3184. Greyscale is linear from -1 to 321 $\mu$Jy. . 104
4.3 Radio sources overlayed on a DSS image M101. Yellow circles are flat spectrum sources. Green are steep spectrum. Blue are inverted spectrum. Red are undetermined due to uncertainty. Red crosses show the positions of historical supernovae SN 1951H and SN 1970G. The SNe lie outside our radio field. . . . . 105
4.4 NGC 5461 in M101 . . . . . 106
4.5 Same as Figure 4.3 for NGC 3184. Historical SN 1909A lies outside the DSS field and our radio field. . . . . 107
4.6 Two sources near NGC 3184 . . . . . 108

5.1 B-band image of NGC 6300 from the CTIO 1.5m. This image was used for reference in Ryder et al. (1996). The bar and ring structure is evident. Prominent dust lanes can be seen lacing through the ring. . . . . 111
5.2 (*top*) Adaptively smoothed image ($1-2$ keV) of NGC 6300 showing three primary sources. (*bottom*) Raw image ($0.4-2$ keV) taken from MOS1 & MOS2 CCDs. The nucleus and two serendipitous sources are clearly indicated by arrows. Evidence in the raw photons indicate the presence of other faint sources along the ring structure. The faint sources near Source 1 are likely the origin of a "shelf" of emission seen in adaptively smoothed images of the galaxy. . . . . 115
5.3 Closeup of HST field of NGC 6300. Contours are from a smoothed $1-2$ keV *XMM-Newton* image. Several star clusters are seen along a prominent dust lane. . . . . 116
5.4 Closeup of area near Source 2. The background image is the H-band image from AAT. Contours are from a smoothed $1-2$ keV *XMM-Newton* image. There is a faint IR source just to the northeast of the center of the X-ray contours. . . . . 117
5.5 Smoothed *XMM-Newton* image of NGC 6300. Circles show the location of the background extraction regions used in the spectral analysis of the eastern point source. . . . . 120
5.6 XMM spectrum of source 1. This spectrum utilized one of several background regions shown in Figure 5.5. . . . . 121
5.7 MOS ( *red*) and PN (*black*) spectra of Source 2. Solid lines denote model fits. Spectra are grouped such that there are 20 counts per bin. . . . . 122
5.8 Radio contour maps of NGC 6300. The upper map shows 20cm emission and the lower shows 13cm emission. Contour levels are the multiple values (2.83, 4 5.66, 8, 11.31, 16, 22.63, 32, 45.25, 64, 90.51, 128, 181.0, and 256) of 0.05 mJy. Triangles show the position of the X-ray point sources. The size of the triangles reflect the $4.1''$ resolution of *XMM-Newton*. . . . . 126

5.9 A constructed spectral energy distribution for Source 2. Triangles indicate measured upper flux limits. Red symbols are radio, maroon symbols are infrared points, green denotes OM point, and the black line denotes unabsorbed X-ray spectral model. Additionally, photometry points for a faint nearby IR source are shown. Colored lines have been added to guide the eye. The precipitous drop in the SED from the "nearby" IR source makes it highly unlikely that this source is associated with Source 2. . . . . 129
5.10 Distribution of BL Lac objects from Padovani & Giommi (1995). The shaded region denotes the range of $\alpha_{rx}$ for source 2. . . . . 130
5.11 Observed spectral energy distribution of the ULX described in Foschini et al. (2002) (Figure 5). The object was identified as a $z = 0.43$ BL Lac object through optical spectra and observations at multiple frequencies. . . . . 130

A.1 Schematic of a basic two dish radio interferometer. . . . . 148
A.2 Printed output of AIPS task LISTR with OPTYPE='SCAN'. . . . . 153
A.3 Antenna layout from PRTAN. The data file this is from is the same as the LISTR output above. The antenna numbers are in parentheses while the associated antenna pad (e.g., N36 for antenna 1) is listed beside it. . . . . 154
A.4 An example of a TVFLG run. The menu (in the boxes) and status lines (at the bottom) are displayed in a graphics plane which is normally colored light green. Data along the horizontal axis is baseline order, and time runs from bottom to top. The horizontal gaps in the display are times when the telescope was slewing to a new pointing position. The vertical bars correspond to baselines associated with each antenna, beginning with 01-02 (antenna 1 to antenna 2). Each bar is narrower as to prevent over counting of baselines. . . . . 156
A.5 *(left)* Un-calibrated *uv*-data and *(right)* calibrated *uv*-data from a C-band snapshot of 3C 48. Default VLA gains are a tenth of the actual gains and can show significant scatter. Only wild *uv* points $\sim 50\%$ greater than the average can be detected before calibration. . . . . 158

B.1 The *Chandra* Observatory with certain subsystems labeled. LGA is an acronym for the Low Gain Antenna. From the *Chandra* Proposer's Observatory Guide, v8.0. . . . . 179
B.2 The *Chandra* High Resolution Mirror Assembly (HRMA) is a set of 4 nested grazing -incidence mirrors. From *Chandra Proposer's Observatory Guide, v.8.0*180
B.3 Diagram of the *ACIS* instrument. At top is the *ACIS-I* array and at bottom the *ACIS-S*. The X and + symbols denote the nominal aimpoints of each array in imaging mode. From POG (2006), figure 6.1 . . . . . 181

# Abstract

What follows is a detailed report of the doctoral work that I have performed as a graduate student at the University of Oklahoma. The catalog of information is meant to be useful for future targeted studies of the zoo of objects that are seen in nearby galaxies. With the development and commissioning of new observational tools, the use of multi-wavelength observations for the study of astrophysical phenomena is becoming very common in the pursuit of the understanding of our universe.

We present analyses of deep radio observations of M83 taken with the Very Large Array spanning fifteen years, including never before published observations from 1990 and 1998. We report on the evolution of 55 individual point sources, which include four of the six known historical supernovae in this galaxy. A total of 10 sources have X-ray counterparts from a *Chandra* survey. Each of these sources show non-thermal spectral indices, and most appear to be X-ray supernova remnants. Comparing the radio source list to surveys in optical and X-ray, we identify three optical/X-ray supernova remnants. Nearly half of the detected radio sources in these observations are coincident with known HII regions lying in the spiral arm structures of the galaxy. We also report on changes in emission from the complex nuclear region, which has shown variability at 20cm wavelengths. We confirm that the peak radio emission from the nucleus is not coincident with the known optical center. One lesser nuclear peak is consistent with the optical/IR nucleus. Previous dynamical studies of a "dark" nuclear mass indicate a possible match to other radio nuclear emission regions in M83.

We report the analyses of deep radio observations of the interacting galaxy system M51

from the Very Large Array. We detect emission from the Type Ic SN 1994I nearly a decade after explosion. We find that the emission ($160 \pm 22$ $\mu$Jy beam$^{-1}$ at 20 cm, $46 \pm 11$ $\mu$Jy beam$^{-1}$ at 6cm, $\alpha = -1.02 \pm 0.28$) is consistent with light curve models for Type Ib/Ic supernovae. We detect X-ray emission from the supernova, but no optical counterpart is detected. We compare our radio maps with a deep H$\alpha$ image from a Hubble Space Telescope observations using the Advanced Camera for Surveys. We find that six of the associated H$\alpha$ sources are young SNRs with resolved shells. Most of the SNRs exhibit steep continuum radio spectra consistent with synchrotron emission. Based on a Cas A expansion velocity, we estimate the age of the SNRs to be $\sim 2000 - 3300$ yr. A brief discussion of IR/UV emission coincident with compact radio sources is presented. We find thirteen radio sources in M51 have X-ray counterparts, 8 of which appear to be SNRs. We report on the analysis of the Seyfert 2 nucleus in this galaxy, including the evidence for bipolar outflows from the central black hole.

Included is a preliminary report on radio analyses of M101 and NGC 3184. The deep radio observations of M101 yield 28 compact radio sources. A shorter set of observations for NGC 3184 yield the detection of 10 radio sources. Six were seen at both 6 cm and 20cm, all with non-thermal continuum spectra.

We report the results of a day long observation of the ringed, barred spiral galaxy NGC 6300 by *XMM-Newton*. We present an analysis of non-nuclear emission and report the discovery of two non-nuclear point sources. We present analysis of these point sources in multiple wavelengths using data from Anglo-Australian Observatory, Australia Telescope and HST.

# Chapter 1

# Introduction

## 1.1 Background and Motivation

Since Karl Jansky's discovery of radio emission from the Galactic center in 1933, astronomers have been using multiwavelength observations to learn about the Universe we call home. The first published maps of the radio sky were presented by Reber (1944) using a telescope he built in his backyard. This coincided with the prediction of the 21 cm emission line of neutral hydrogen. The discovery of the hydrogen line in 1951 by Ewan and Purcell and noted by van de Hulst (1951) ushered in a new era in astronomy. Within a decade new radio observatories were being built around the world to study the first new window in the electromagnetic spectrum.

The development of radio receivers and observing techniques has enabled scientists to discover a wealth of new types of objects: pulsars, quasars, huge jets emanating from the centers of galaxies, etc. This has led to new theoretical models for the formation and evolution of these objects. The radio window has revealed details about familiar objects (like planets and nearby galaxies) that might never have been seen.

Not long after radio astronomy took off, scientists began working on telescopes to explore other spectral windows that were not previously observed. The advancing space program led to the launch of X-ray satellites in the 1970s. Data from these early telescopes led to the discovery of Galactic X-ray binaries. It was also discovered that the nucleus of active galaxies were intense and often variable X-ray sources. As X-ray telescopes improved, many

objects were seen to emit in this high energy region of the spectrum, including ordinary stars.

The importance of multiwavelength studies has increased as technology has improved. Although the information received differs in different observing bands, each is part of the whole picture. An astrophysicist studying a specific object must use all of the tools available to develop a complete picture.

This is where the work in this dissertation comes in. Rather than a targeted, specific study of one type of object (e.g., supernovae), the work presented in this dissertation comprises more of a survey of compact radio sources which will be useful to the general astronomy community. The collection of properties may be used in the future for targeted studies of SNe, SNRs, X-ray binaries, and H II regions in nearby galaxies. They will be useful in expanding the knowledge of spectral energy distributions for many of these objects, which will help to improve theoretical models of the emission mechanisms, galaxy evolution, and the global properties of the individual systems presented within those galaxies.

Using the National Radio Astronomy Observatory's Very Large Array, a 27-element interferometer located in the desert of New Mexico, I have conducted a deep survey of a sample of nearby, face-on, spiral galaxies: M83 (NGC 5236), M51 (NGC 5194/5), M101 (NGC 5457), and NGC 3184. These galaxies were chosen by John Cowan, David Branch and Christopher Stockdale based upon the wealth of supernova (SN) activity over the last century. Each galaxy hosts a variety of objects and phenomena that make them excellent laboratories to study star formation, nuclear outflows, supernova remnant (SNR) evolution, and radio SNe. As will be shown in the pages to follow, each galaxy is different. M83 and M51 each provide numerous sources to study.

The last galaxy that will be discussed in this dissertation will be the ringed, barred, spiral galaxy NGC 6300. My participation in the study of this galaxy began as an analysis of two X-ray point sources seen in an *XMM-Newton* observation. My analysis expanded to include a search for optical, infrared (IR) and radio counterparts to the sources in the X-ray image.

In the following section, I will give a brief introduction to all of the galaxies, in order, that will be presented in this dissertation. Included in the discussions will be optical images of each object. Looking at radio images of these galaxies, it can be hard to believe that one is actually observing a spiral.

I would like to make a note about the titles of the chapters. Most of the chapters in this dissertation have rather straightforward titles. The one exception is Chapter 5, whose title seems out of place with the rest of the work presented here. The work presented in that chapter is a continuation of the work presented in Matsumoto et al. (2004), a paper that I worked on just before its publication. The title reflects the continuing nature of the project.

## 1.2 X-Ray Sources in Normal Galaxies

### 1.2.1 X-Ray Binaries

With the advent of X-ray telescopes, there have been many types of X-ray sources discovered in the universe. Many of the brightest sources originate from supermassive black holes in the centers of galaxies. In galaxies there also exists a myriad of smaller X-ray point sources. Some have been identified as young X-ray supernova remnants (SNRs). Many more have

been discovered to be binary systems involving a neutron star or black hole orbiting another body, usually a star, and accreting matter from the companion. These systems are called X-ray binaries (XRBs).

We can divide XRBs further into low-mass X-ray binaries (LMXRBs) and high-mass X-ray binaries (HMXRBs). The distinction lies in the mass of the companion object.

In low-mass X-ray binaries, the companion is usually a spectral type A star or later[1]. The X-rays form when the black hole or neutron star accretes mass from the star as it evolves. These objects tend to be transient sources, going through periods of high and low emission.

In high-mass X-ray binaries, the companion is an O or B star. These hot massive stars have high stellar winds that can shed mass at rates of $10^{-10} - 10^{-4}\ M_{\odot}\ yr^{-1}$ (Lewin et al., 1995). The compact object in this system can take up enough of this wind to power X-ray production. The systems exhibit continuous emission with longer lifetimes than the emission from the LMXBs.

XRBs can emit in the radio through the production of bipolar jets from the accretion disk. These jets can be beamed toward the observer resulting in the detection of high radio luminosity. Other XRBs spend most of the time in a quiescent radio state. These experience radio flaring on occasion where the radio luminosity may rise by a factor of $10^2$ or more. At the distance of nearby galaxies, the detection of quiescent XRBs is not possible.

[1]Spectral type of stars (O,B,A,F,G,K,M) is a measure of the surface temperature of the star. In main-sequence stars, when they fuse hydrogen to helium in the core, the spectral type also gives an indication of mass. O stars are the hottest and most massive, while M stars are cooler and less massive.

### 1.2.2 Ultraluminous X-Ray Sources

While many bright X-ray sources are associated with galactic nuclei, there have been many observed non-nuclear sources which have high X-ray luminosities. Some have been identified as young X-ray supernova remnants, but others prove to be another type of object all together. These ultraluminous X-ray sources (ULXs) are defined as non-nuclear objects with luminosities $L \geq 10^{39}$ erg s$^{-1}$(Makishima et al., 2000).

As to the nature of these sources there are many competing scenarios. Fabbiano (2004) contends that ULXs may constitute a wide range of astrophysical phenomena. Four of these are summarized in Soria et al. (2004) (and references therein). They include: (1) intermediate-mass black holes with masses $\sim 10^2 - 10^3 M_\odot$; (2) stellar mass black holes XRBs ($M \lesssim 20 M_\odot$) with mild geometrical beaming, during phases of super-Eddington mass accretion; (3) microquasars with a relativistic jet pointing towards us; (4) BH XRBs with super-Eddington emission from inhomogeneous disks. Each scenario implies its own observable feature.

### 1.2.3 Source Classification

The goal of the study presented in this dissertation is to classify sources through the use of complementary observations in multiple bands. For sources with X-ray and radio detections, this is aided by a general scheme devised by Prestwich et al. (2003) using X-ray colors. X-ray counts are determined in three bands: the soft band (0.3-1 keV), medium band (1-2 keV) and hard band (2-8 keV). Then X-ray colors are calculated as "hard color" and "soft color" using the formulae

$$HC = \frac{(H - M)}{(H + M)} \tag{1.1}$$

$$SC = \frac{(M - S)}{(M + S)}, \tag{1.2}$$

where *H, M,* and *S* are the hard, medium and soft counts, respectively.

Figure 1.1 shows resulting classification scheme using real data. While there will be overlap between the regions of color-color space, due to absorption and similarities between low-mass and high-mass XRB with black holes, the color classifications give a good starting point to application in extragalactic population studies.

## 1.3 Emission Mechanisms

The purpose of this section is to provide a description of the theory behind the different forms of radiation produced in the compact sources described in this dissertation. Radio emission generally falls into two categories: thermal emission (primarily thermal bremsstrahlung) and non-thermal emission (synchrotron). In the X-ray, emission comes through the heating of gas to temperatures of $\sim 10^7$ K. At these temparatures, thermal Bremsstrahlung can produce X-ray emission. Another mechanism is the scattering of photons off of electrons, with the photons gaining energy in the collision (inverse-Compton scattering).

### 1.3.1 Thermal Bremsstrahlung

Bremsstrahlung (literally "braking radiation," also known as "free-free" emission) arises when one particle interacts with another particle, slowing down in the process, and emitting a photon. While electron-electron collisions can redistribute energy more efficiently, collisions between identical particles have no net dipole radiation (Longair, 1994). The

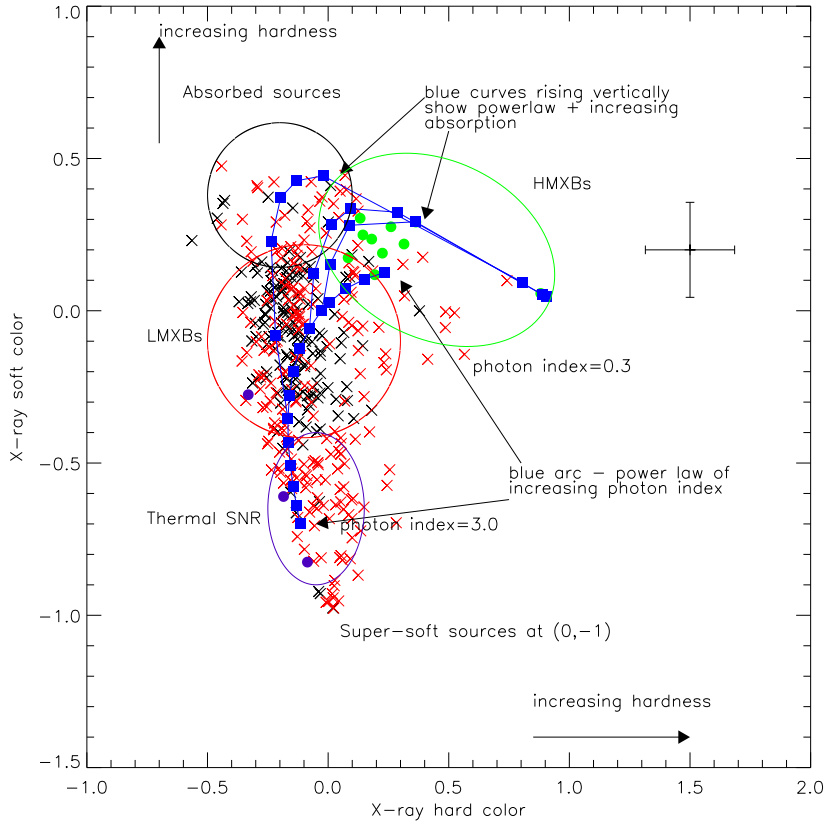



Figure 1.1 Classification scheme form Prestwich et al. (2003). The red circle outlines the area of the color-color diagram which is probably dominated by LMXBs, the purple ellipse the region occupied by thermal SNRs, and the green ellipse the region occupied by HMXBs. The black circle delineates the most absorbed sources, and is probably a mixture if types. The blue arc of points stretching from (0.3,0.15) to (-0.1,-0.7) show the colors of a simple power law spectral model with photon index increasing from 0.7 to 3.0. The blue curves rising vertically show the effect of adding absorption to power law slopes of photon index 1.0, 1.2 and 2.0.

primary source of Bremsstrahlung in astrophysics are electrons interacting with protons.

For a single particle the power generated in non-relativistic Bremsstrahlung is

$$P = -\frac{dW}{dt} = \frac{16\pi^6}{3\sqrt{3}c^3 m_e^2 v}\nu N Z^2 g_f \tag{1.3}$$

where, in cgs units, $e$ is the elementary charge, $c$ is the speed of light, $m_e$ is the mass of the electron, $v$ is the speed of the electron, $\nu$ is the frequency of the radiation, $N$ is the total number of ions, $Z$ is the ionic number, and $g_f$ is the Gaunt Factor.

Bremsstrahlung has the property that electrons of energy $E$ produce photons at typical energy $< h\nu > \sim E/3$ (Longair, 1994). The radio emission from H II regions is produced by this process.

### 1.3.2 Synchrotron Emission

A charged particle in a magnetic field circles the magnetic field lines due to the Lorentz force. At low energies this produces cyclotron radiation, at a single frequency – the gyrofrequency of the electron. However, a relativistic electron produces a continuum of synchrotron radiation.

The power emitted in synchrotron radiation by a single electron is

$$P = -\left(\frac{dE}{dt}\right) = \frac{4}{3}\sigma_T c \beta^2 U_B \gamma^2 \tag{1.4}$$

where $U_B$ is the energy density of the magnetic field $B^2/8\pi$, and we have averaged over the magnetic field orientation. Unlike Bremssrahlung, the relativistic electron population responsible for synchrotron emission has a negligible cross-section for atomic transition, excluding this population as a source of line emission. Synchrotron emission occurs in

astrophysics settings at all scales, from the radiation belts of Jupiter to jets in active galactic nuclei (AGN).

Synchrotron emission arises in SNe and SNRs due to the interaction of the expanding shock with the circumstellar material (CSM) and later, the interstellar medium (ISM) (Weiler et al., 2002). As the supernova expands, the shock runs into the dense CSM, compressing the magnetic field in the process. The free electron in this region are accelerated to relativistic speeds and interact with the magnetic field, losing energy in the form of radiation. In the case of Type Ib/Ic supernovae, whose progenitors have higher mass-loss rates, this interaction can go on for more than 1000 yr (Chevalier, 2006)

### 1.3.3 Inverse-Compton Emission

Compton Scattering takes place when a high energy photon impacts a charged particle, normally transferring momentum to the particle. (At low energies this is Thompson scattering.) Inverse-Compton scattering is a term used in astrophysics to describe a less common situation where a particle transfers momentum to the photon. The inverse-Compton effect can be described by a coordinate transformation of the Compton effect – in fact, in the rest frame of the particle, it *is* the Compton effect. If the energy of the incoming photon is low in the electron rest frame ($E_\gamma << m_e c^2$), the Thompson cross-section, $\sigma_T$, can be used. If the energy is high then the full quantum-mechanical Klein-Nishina formula must be used, which has the effect of reducing the cross-section.

The power radiated by a singel electron through inverse-Compton is

$$P_{IC} = \frac{2}{3}\sigma_T \gamma^2 \beta^2 U_{photon} \tag{1.5}$$

where $\beta$ is $v/c$, $\gamma$ is the Lorentz factor of the relativistic electron

$$\gamma = \left(1 - \frac{v^2}{c^2}\right)^{-1/2},$$

and $U_{photon}$ is the energy density of the photon field.

The energy of the outgoing photon is boosted by $\gamma^2$. This can be explained by boosting the incident photon into the electron rest frame, and boosting the scattered photon back into the lab frame, picking up one factor of $\gamma$ each time.

$$(h\nu)_{out} \sim \gamma^2 (h\nu)_{in} \tag{1.6}$$

where $h$is Planck's constant. There is a maximum energy that a photon may gain from a collision (a head-on collision)

$$(h\nu)_{max} = 4\gamma^2 (h\nu)_{in} \tag{1.7}$$

(Longair, 1994).

This type of emission produces X-rays in a variety of astrophysical phenomena. These include pulsar wind nebulae, and AGNs.

## 1.4 The Sample

### 1.4.1 M83

M83 (NGC 5236) is a nearby SABc galaxy that is nearly face-on ($i = 24°$, Talbot et al., 1979). It is relatively nearby with distance estimates ranging from 3.75 Mpc (de Vaucouleurs, 1979a) to 8.9 Mpc (Sandage & Tammann, 1987). We have opted to use the Cepheid-established distance of 4.5 Mpc (Thim et al., 2003). The proximity of M83 has

made it an ideal candidate for observations at all wavelengths. The presence of large quantities of gas and dust imply observable levels of enhanced star formation. Previous studies have also noted vigorous star formation in the nuclear region of the galaxy (e.g., Elmegreen et al., 1998). Similar star formation activity is evidenced by the discovery of six supernovae in modern times: SN 1923A, SN 1945B, SN 1950B, SN 1957D, SN 1968L, and SN 1983N. The results of monitoring of these historical supernovae in the radio have been presented in Cowan & Branch (1982, 1985); Cowan et al. (1994); Eck et al. (1998, 2002) and Stockdale et al. (2006). A DSS optical image of M83 is shown in Figure 1.2.

In addition to the radio surveys, several X-ray studies have been performed on M83. Kilgard et al. (2002) and Kilgard et al. (2005) included it in a larger survey of nearby galaxies. Soria & Wu (2002, 2003) also presented detailed analyses of *Chandra* observations of this galaxy. Optical surveys have also provided evidence of high star formation in the form of HII regions (Rumstay & Kaufman, 1983) and supernova remnants (SNRs; Blair & Long, 2004).

Comparisons of compact sources at multiple wavelengths provide critical information about late stages of stellar evolution, emission mechanisms, the transition of supernovae to supernova remnants, etc. In this paper we report on the results of analysis of fifteen years of radio observations of M83, including new, never before published data from 1990 and 1998. We will begin by describing the observations dating back to 1981, before the Very Large Array[2] was completed. A brief description of the analysis techniques will then be presented in Section 3. In the sections that follow, results will be presented for specific

[2]The Very Large Array of the National Radio Astronomy Observatory is a facility of the National Science Foundation operated in cooperative agreement by Associated Universities, Inc.

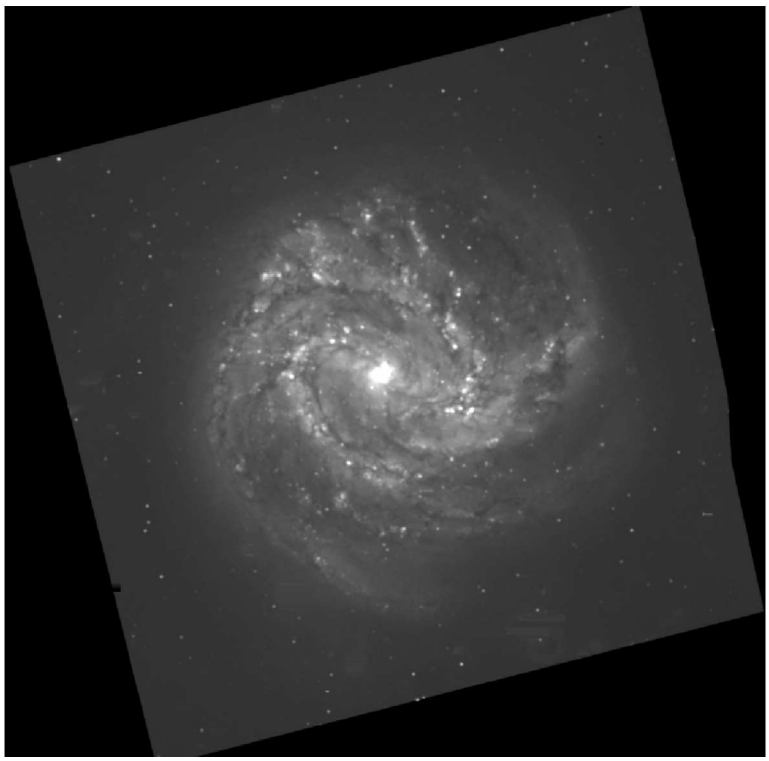


Figure 1.2 DSS image of M83.

sources. The first discussion will be a brief report on the observed historical supernovae. For the remaining unidentified sources, comparisons with optical and X-ray studies will be presented to identify SNRs, HII regions and X-ray binaries (XRBs). Finally, a discussion of the complex nuclear emission will be presented.

### 1.4.2 M51

M51 (NGC 5194/5) is a nearby, grand-design spiral galaxy with an early-type companion forming an interacting pair. It is nearly face-on ($i \sim 20^{\circ}$), which makes it an ideal candidate for population and morphology studies at all wavelengths. Figure 1.3 shows a DSS optical image of the galaxy.

The few distance determinations for M51 range from 6.0 Mpc (Baron et al., 1996) to 9.6 Mpc (Sandage & Tammann, 1974). We have opted to use the distance of 8.4 Mpc as derived by the planetary nebula luminosity function (PLNF) of the galaxy (Feldmeier et al., 1997)

Despite the interaction with M51b, the star-formation rate in the main galaxy is rather modest (Calzetti et al., 2005). The M51a/b interacting system has played host to three supernovae in modern times. M51a was the parent galaxy to SN 1994I (Puckett et al., 1994) and SN 2005cs (Kloehr et al., 2005), the latter of which will not be discussed further in this paper. M51b was host to SN 1945A (Kowal & Sargent, 1971). We will report briefly on the radio emission of SN 1994I, the only supernova that we have detected in our radio observations.

M51 contains a low-luminosity Seyfert 2 nucleus that exhibits evidence of a bipolar outflow (e.g. Ford et al., 1985). The outflow has been studied in several wavebands.

In this paper we present multiwavelength analyses of the numerous compact radio sources in M51 from new, high-resolution observations using the Very Large Array. We present details of the radio observations and analysis. We compare our radio observations with archived optical, infrared (IR) and X-ray data to find counterparts in these complementary bands. Finally, we discuss the radio emission from the Seyfert 2 nucleus.

### 1.4.3 M101 and NGC 3184

M101 is a large, nearly face-on ($i \sim 17°$, Zaritsky et al., 1990), grand-design spiral galaxy. It has been the host to three historical supernovae: SN 1909A, SN 1951H, and SN 1970G. Its proximity and large size has made M101 an ideal candidate for the study of star formation

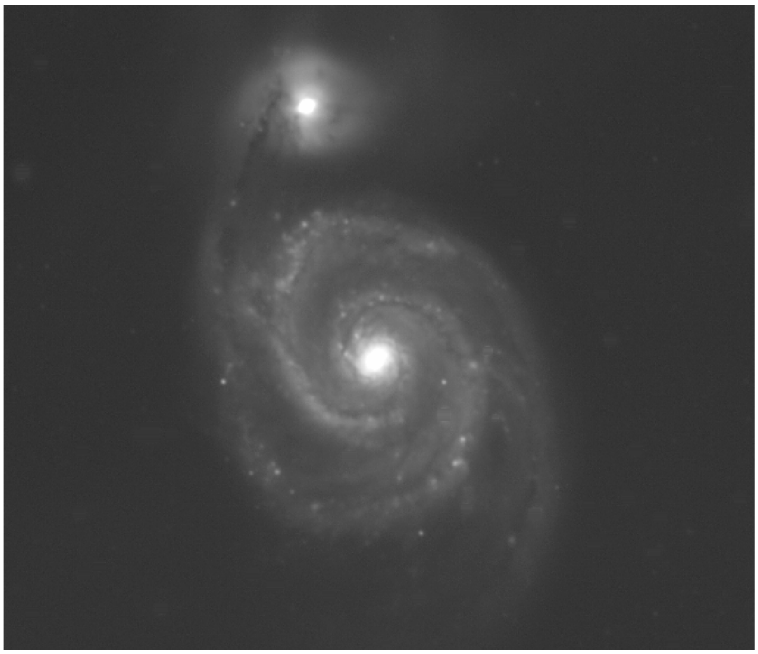


Figure 1.3 DSS image of M51.

and H II regions (e.g., Scowen et al., 1992). Optical images of these galaxies are shown in Figures 1.4 and 1.5.

NGC 3184 is a also a large, nearly face-on spiral. NGC 3184 has a relatively low star formation rate (Kennicutt et al., 2003) based in H$\alpha$ studies. Despite this, NGC 3184 has played host to four historical supernovae: SN 1921B, SN 1921C, SN 1937F, and SN 1999gi.

The published distances to M101 range from 3.3 Mpc(de Vaucouleurs, 1979b) to 7.7 Mpc (Feldmeier et al., 1997). We have chosen to adopt distance of 7.7 Mpc for M101 based on the PLNF, same method used for M51. Distance determinations to NGC 3184 range from 7.2 Mpc (Tully-Fisher, Pierce, 1994) to 13.8 Mpc (group membership; Freedman et al., 2001). We have adopted a distance of 11.1 Mpc, as determined by Leonard et al. (2002) using the expanding photosphere method on SN 1999gi.

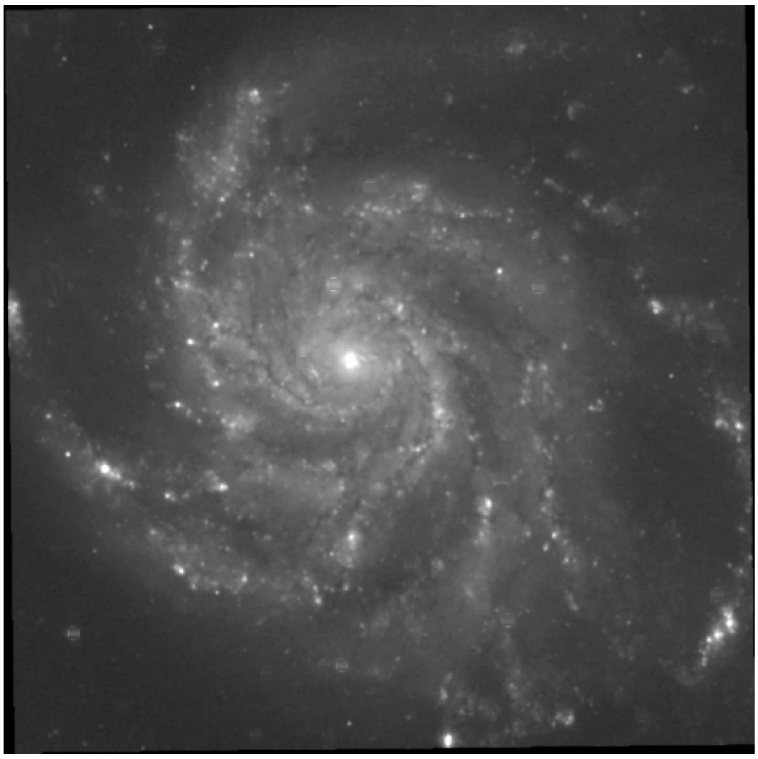


Figure 1.4 DSS image of M101.

Both galaxies have large H I halos (Walter et al., 2005) that extend far beyond our current radio fields.

For this presentation, I will present preliminary results based on radio observations of M101 and NGC 3184. First, the observations and data processing will be described. Second, I will present the resulting source properties and analysis. Finally, I will briefly mention the nature of a few sources. Finally, I will give a mention the work that is still required to finish this project.



Figure 1.5 DSS Image of NGC 3184



Figure 1.6 B-band image of NGC 6300 from the CTIO 1.5m. This image was used for reference in Ryder et al. (1996). The bar and ring structure is evident. Prominent dust lanes can be seen lacing through the ring.

### 1.4.4 NGC 6300

NGC 6300 is one of the nearest (z=0.0037; Mathewson & Ford, 1996) and largest ringed galaxies (Buta, 1987). It is also the least typical. The inner ring structure is composed of tightly wound, dust-riddled spiral arms. No inner ring structure is seen due to the bright Seyfert 2 nucleus which is further confused by the presence of two foreground stars. An optical image of NGC 6300 is shown in Figure 1.6

Study of NGC 6300 began with its discovery by Reynolds (1921). The first photometric work was performed by de Vaucouleurs (1956), and kinematic studies were first done in the late 1970s (Sandage, 1978). Beginning with Buta (1984) more detailed study of the structure and kinematics of the galaxy have been undertaken. Some of the results are described below.

Ryder et al. (1996) performed a study of the distribution of neutral hydrogen (HI) in

NGC 6300 and a more typical ringed galaxy, NGC 1433. NGC 6300 contained a broader HI disk than did NGC 1433. The halo of the galaxy shows a 20° warp and a short tail. While this could be explained by tidal interactions with passing neighbors, no galaxy has been found near enough to have interacted with NGC 6300 in the recent past. Ryder et al. (1996) also note that the outer pseudoring and the nuclear ring predicted in resonance ring theory are not seen in NGC 6300. They postulate that NGC 6300 may be a developing resonance ring galaxy.

More evidence for an evolutionary scenario is the apparent bar-inner ring misalignment. The bar feature of NGC 6300 is misaligned from the major axis of the ring structure by 80° (Buta, 1984). A broader catalog of ringed, barred galaxies show that this feature is very rare (Buta, 1995). In one case Buta et al. (1999) report analysis of a nuclear starburst in the peculiar galaxy ESO $565-11$. In numerical simulations, they determine that the unusual features in that galaxy may evolve over time to be more consistent with other resonance ring galaxies.

Buta (1995) also suggest that the misalignment might be an indication that, at least in these rare cases, the resonances that form the ring were less influenced by the bar. In the aligned cases the ring patterns seem to be driven by the bar potential. While numerical simulations have been performed, there is still little understanding about how this misalignment occurs.

In a study of HII regions of ringed, barred galaxies, Crocker et al. (1996) noted that NGC 6300 has other interesting differences from others in its class. NGC 6300 contains nearly twice the number of star-forming regions as any other galaxy in their sample. Of these almost half (457) had luminosities higher than $L(\mathrm{H}\alpha + [\mathrm{NII}]) \geq 5 \times 10^{37}$ erg s$^{-1}$.

Outside the nucleus, all of the HII regions lie in the ring structure. Such vigorous star formation should lead to an elevated supernova rate in turn producing a wealth of X-ray binaries.

Another interesting feature is that the distribution of HII regions peaks in areas perpendicular to the bar. In more typical ringed galaxies, star forming regions are found clustered near where the bar intersects the ring.

In the following sections, we present the results of a multiwavelength study of two non-nuclear X-ray sources detected in a day long observation by *XMM-Newton*. Using archived observations at radio, infrared and optical wavelengths, we aim to determine the classification of these sources. X-ray spectral analysis of the active nucleus was presented in an earlier paper (Matsumoto et al., 2004). Time series analysis of the nucleus was presented by Awaki et al. (2005).

In section 2 we describe the observations and data reduction. Next we will present the analysis as it stands at the moment. In section 4 we discuss the result of the analysis and give preliminary conclusions as to the nature of the sources.

All X-ray spectral fits include a Galactic neutral hydrogen column density of $9.83 \times 10^{20}$ cm$^{-2}$ (Dickey & Lockman, 1990). Errors quoted are 1-$\sigma$ and upper limits are 5-$\sigma$. Luminosities are determined using the WMAP value of the Hubble constant ($H_0 = 72$ km s$^{-1}$ Mpc$^{-1}$).

# Chapter 2

# A Study of Compact Radio Sources in Nearby Face-on Spiral Galaxies. I. Long Term Evolution of M83

## 2.1 Introduction

M83 (NGC 5236) is a nearby SABc galaxy that is nearly face-on ($i = 24°$, Talbot et al., 1979). It is relatively nearby with distance estimates ranging from 3.75 Mpc (de Vaucouleurs, 1979a) to 8.9 Mpc (Sandage & Tammann, 1987). We have opted to use the Cepheid-established distance of 4.5 Mpc (Thim et al., 2003). The proximity of M83 has made it an ideal candidate for observations at all wavelengths. The presence of large quantities of gas and dust imply observable levels of enhanced star formation. Previous studies have also noted vigorous star formation in the nuclear region of the galaxy (e.g., Elmegreen et al., 1998). Similar star formation activity is evidenced by the discovery of six supernovae in modern times: SN 1923A, SN 1945B, SN 1950B, SN 1957D, SN 1968L, and SN 1983N. The results of monitoring of these historical supernovae in the radio have been presented in Cowan & Branch (1982, 1985); Cowan et al. (1994); Eck et al. (1998, 2002) and Stockdale et al. (2006).

In addition to the radio surveys, several X-ray studies have been performed on M83. Kilgard et al. (2002) and Kilgard et al. (2005) included it in a larger survey of nearby

galaxies. Soria & Wu (2002, 2003) also presented detailed analyses of *Chandra* observations of this galaxy. Optical surveys have also provided evidence of high star formation in the form of HII regions (Rumstay & Kaufman, 1983) and supernova remnants (SNRs Blair & Long, 2004).

Comparisons of compact sources at multiple wavelengths provide critical information about late stages of stellar evolution, emission mechanisms, the transition of supernovae to supernova remnants, etc. In this paper we report on the results of analysis of fifteen years of radio observations of M83, including new, never before published data from 1990 and 1998. We will begin by describing the observations dating back to 1981, before the Very Large Array was completed. A brief description of the analysis techniques will then be presented in Section 3. In the sections that follow, results will be presented for specific sources. The first discussion will be a brief report on the observed historical supernovae. For the remaining unidentified sources, comparisons with optical and X-ray studies will be presented to identify SNRs, HII regions and X-ray binaries (XRBs). Finally, a discussion of the complex nuclear emission will be presented.

## 2.2 Observations and Data Reduction

We have observed M83 with the VLA several times between 1981 and 1998. Table 2.1 summarizes each of the observations. Reports of the 1981, 1983 and 1990 observations have been presented by Cowan & Branch (1982, 1985) and Cowan et al. (1994). The new 1998 observations will be presented here. For this paper, some of the older data have been reprocessed and reimaged in order to to allow consistent analyses and comparisons over

many years.

The first 20cm observation was performed on 10 April 1981 using 22 antennas while the array was being moved from A to B configuration. More 20cm observations were done on 15 and 17 December 1983 in the BnA hybrid configuration. A 6cm observation was taken on 14 March 1984 in the hybrid CnB configuration. These observations were reported in Cowan & Branch (1982, 1985) M83 was observed again at 6cm on 14 October 1990 (CnB), and at 20cm on 30 June 1990 (BnA). These were reported in Cowan et al. (1994). Finally, we observed M83 in 1998 at 20cm (June 13 and 15, BnA) and 6cm (October 31 and November 1, CnB). Cowan et al. (1994) reported results of a 1992 20 cm observation taken in B configuration. The original 1990 observation was believed to be corrupted at the time due to the dramatic fading of SN 1957D. In reprocessing the this observation, we have determined it to be good, and since the array was in the preferred configuration, we have opted to present the observation here for the first time.

All of the data were processed using the Astronomical Image Processing System (AIPS) provided by NRAO. Flux calibration was performed using 3C286 as the primary source calibrator. To correct for atmospheric phase variations, a secondary calibrator, B1354-132 was used for the 1983 and 1984 observations, and J1316-336 was used for the 1990 and 1998 data sets. Due to changes in the AIPS system, we were unable to reproduce adequate maps for the earliest observations. We have opted to use the original maps presented in Cowan & Branch (1985). The remaining data were then imaged using the AIPS task IMAGR using a Briggs robustness parameter of 0. This value has the advantage of minimizing noise while allowing for excellent point source detection in resultant images. During the imaging process, we also employed self-calibration loops using the task CALIB to improve the noise

levels on the maps. The data sets were deconvolved using Gaussian restoring beams, the sizes of which are indicated in Table 2.1. The deconvolved beams were determined using the values for the "dirty" beam, calculated from the Fourier transform of the $u$-$v$ plane coverage. After imaging, the task PBCOR was run on each map to correct for the shape of the primary beam.

## 2.3 Data Analysis

An initial source list was obtained using the AIPS task SAD, which searches for points in a radio image that are higher than a specified level. A gaussian fit is the applied to each detected area of emission, and fits that fail are rejected by the algorithm. Many extended and slightly extended sources were listed as multiple sources. The list was compressed to account for this. Nuclear emission was removed from the source list. Finally, a visual inspection of the maps was performed in order to find sources that were rejected by the detection algorithm. The final list of sources along with peak flux densities at all epochs is presented in Table 2.2. Table 2.3 lists the spectral indices ($S \propto \nu^{+\alpha}$) of each source.

The sources were then fit using the AIPS task IMFIT. The input model was a two-dimensional Gaussian with a linear sloping background as was implemented in Cowan et al. (1994). Fluxes for the sources are listed in Table 2.2. Where no value exists, we assume a 3-$\sigma$ upper limit of 0.59 mJy beam$^{-1}$ (1983 20cm), 0.14 mJy beam$^{-1}$ (1984 6cm), 0.22 mJy beam$^{-1}$ (1990 20cm), 0.11 mJy beam$^{-1}$ (1990 6cm), 0.24 mJy beam$^{-1}$ (1998 20cm), and 0.21 mJy beam$^{-1}$ (1998 6cm). The 20cm map shown in Figure 2.1 shows the positions of the sources in the final list. The 6cm contour map in Figure 2.2 indicates the positions of some of the sources discussed in Cowan et al. (1994) and Eck et al. (1998).

Many of the fluxes of the sources listed in Cowan et al. (1994) differ from fluxes listed in Table 2.2. The reprocessing and reimaging of the older data resulted in maps with different deconvolution sizes than those in the older maps. This produced different flux measurements than maps using the older imaging algorithms. The advantage in reprocessing lies in the fact that all of the older data have been treated in the same manner as the new data.

## 2.4 Discussion

### 2.4.1 Radio Point Sources

#### Historical Supernovae

We detected emission from four of the six historical supernovae (SNe) in M83 (SNe 1923A, 1950B, 1957D and 1983N). Source designations for each of the SNe are provided in Table 2.2. A more detailed discussion of the nature of the historical SNe is presented in Stockdale et al. (2006).

SN 1983N is detected only in the $1983 - 1984$ observations (Cowan & Branch, 1985; Cowan et al., 1994), indicating that it faded very quickly after maximum light. This is consistent with the identification of SN 1983N as a Type Ib supernova (Weiler et al., 1986; Boffi et al., 1999).

Eck et al. (1998) reported the discovery of SN 1923A in the radio. The 1990 observations showed a very faint radio point source, and the reprocessing of the $1983 - 1984$ data did hint at the presence of a source at the position of the supernova, though the flux level is too low to call it a detection. In the 1998 data, we again see a faint source that is coincident with the supernova. In the 1990 maps, the emission appears to be non-thermal in nature.

Rumstay & Kaufman (1983) report the presence of an optical HII region at the position of source 59, coincident with the reported position of SN 1923A. Boffi et al. (1999) could find no optical emission consistent with a supernova expansion shock in the area around SN 1923A. It is possible that we are detecting emission from both objects, though the radio emission is near the limits of detection for the observations.

Cowan et al. (1994) and Stockdale et al. (2006) noted a continuing decline in the radio emission from SN 1957D. However there has been unusual optical activity at the position of the explosion. Long et al. (1989) reported the detection of an optical remnant of SN1957D. The remnant then faded below detectable limits within a few years (Long et al., 1992), suggesting a possible drop in the circumstellar density through which the explosion shock is propagating. Our radio observations also indicate the rapid decline of SN 1957D (see Figure 2.3), and the spectrum seems to be flattening. This could indicate that the supernova is approaching the level of the HII region in the area. The supernova has not faded below this level, but the flattening of the spectrum could mean a greater contribution from the thermal emission of the gas.

As reported in Stockdale et al. (2006), the radio spectrum of SN 1950B seems to have flattened and the flux has remained relatively constant across the 1990 to 1998 epochs. This would imply that the supernova has faded below the level of the local HII regions. SN 1950B occurred in a complex region of emission. Figure 2.4 shows the region and how the emission has changed over the course of the observations.

**Supernova Remnants**

After studying the historical supernovae, we turned our attention to searching for radio counterparts to the numerous optical SNRs reported by Blair & Long (2004). In our search we identified four sources coincident with optical SNRs. Three of these radio sources had corresponding X-ray sources as reported in Soria & Wu (2002, 2003). The SNR counterparts are listed in Table 2.4 and the positions are indicated in Figure 2.1. With the exception of source 39, all sources exhibit continuum spectral indices consistent with those due to synchrotron emission models for radio-emitting SNRs (Berezhko & Völk, 2004).

Source 19 is located on the edge of the southern spiral arm of M83. It has exhibited inverted spectra throughout the observations, with some flattening in 1998. The source faded at 6 cm from 1983 to 1990, and it has remained constant in flux between 1990 and 1998. It could be again that we are seeing larger contributions from thermal emission in this region. The large uncertainties in the spectral index measurements stem from the faintness of the source. Soria & Wu (2003) note the detection of a faint X-ray source coincident with source 19. Two X-ray colors are obtained: a hard color (HC), defined as $(H-M)/(H+M)$ and a soft color (SC), defined as $(M-S)/(M+S)$; where S, M and H are counts in the soft (0.3-1.0 keV), medium (1.0-2.0 keV) and hard (2.0-8.0 keV) bands, respectively. Our resulting colors ($HC = -0.19 \pm 0.45,\ SC = -0.68 \pm 0.17$) are consistent with SNR emission using the classification scheme in Prestwich et al. (2003). Our radio measurements appear to confirm the identification of this source as an SNR.

Source 22 has shown a consistent non-thermal spectrum throughout all observational epochs. It lies in the same region of the galaxy as source 19. This is a crowded region of emission along the southern spiral arm, making isolated measurements difficult. Source 22

has steepened due to the greater fading in the 6cm maps. The source has shown fairly steady emission in the 20cm band. Like source 19 there is a coincident X-ray source. Both source 19 and 22 also exhibit high H$\alpha$ luminosities (Blair & Long, 2004). This is consistent with there being a denser interstellar medium in the region of the sources. The lower resolution 20 cm map presented in Cowan et al. (1994) indicates a high HI density in the area of sources 19 and 22. The X-ray colors for source 22 are not typical for an SNR ($HC = 0.15 \pm 0.22$, $SC = -0.51 \pm 0.14$), though they might indicate the presence of XRB or an X-ray pulsar.

Source 35 has exhibited fairly steady fluxes through all epochs that we are considering. We have determined spectral indices for this source that are consistently non-thermal in nature. Our *Chandra* observations (Kilgard et al., 2005) show that this source has a very soft spectrum ($HC = -0.82 \pm 0.22$, $SC = -0.53 \pm 0.11$), indicative of SNR emission.

Source 39 differs from the other sources discussed here in that it has exhibited consistently thermal spectral indices over the time of observation. We note that the flux density of the source has remained fairly steady with some slight fading in the 6cm band. This is more consistent with the behavior of an HII region than a SNR. There is also a lack of X-ray emission from this source. Blair & Long (2004) identified the optical source as an SNR candidate based on enhanced [SII]:H$\alpha$ ratio. Further spectroscopic confirmation was not possible due to the relatively low luminosity of the region.

### H II Regions

It should come as no surprise that the largest number of radio sources in M83 should be associated with HII regions. M83 is known for exhibiting vigorous star-formation activity as indicated by the large number of observed SNe and SNRs. By far the largest number

of optical counterparts to our radio sources do consist of HII regions. Nearly half of the reported radio sources have coincident optical sources identified with HII emission (Rumstay & Kaufman, 1983). The radio/HII counterparts are listed in Table 2.5. It should be noted that the earlier observations represent some of the first detections of extragalactic HII in the radio at the resolution and flux level that were detected in M83. This is due in part to the depth of each observation. The deep observations also contribute to the ability to see the spiral arm structure of the galaxy as seen in Figures 2.1 and 2.2. It is in the spiral arms where HII regions would be more abundant.

It is clear from Table 2.5, that we are preferentially identifying large optical H II regions. Rumstay & Kaufman (1983) establish a threshold excitation parameter $U \geq 300$pc cm$^{-2}$ to classify a region as large. Only 11% of the Rumstay & Kaufman (1983) sources are classified as large by this criterion, while 12 of 21 radio-detected H II regions fall in this category. If the cut-off was relaxed to 250 pc cm$^{-2}$, 19% of the Rumstay & Kaufman (1983) sources would be included, while 16 of our 21 radio detected H II regions now fall in this regime. We have restricted our comparisons to optical studies with comparable resolutions to our radio observations.

Most of the radio/optical counterpart sources show consistently stable flux densities and flat spectra indicative of thermal emission processes. This type of behavior is what would be expected from the hot gas that composes an HII region. There are notable exceptions. Source 27, although coincident with an optical HII region, is a radio lobe to a background FR II radio galaxy (Maddox et al., 2003; Soria & Wu, 2003).

The spectrum of source 4 has steepened with time. It has shown a consistent increase in 20cm emission, while steadily fading at 6cm. In addition to the associated HII region, there

exists an X-ray counterpart (Colbert et al., 2004). A discussion of the X-ray properties of source 4 are given in the next section.

Sources 53 and 55 are very faint sources. This leads to large uncertainties in the spectral index measurements for each of the sources. As noted earlier, source 53 is coincident with the reported optical position of SN 1923A (Eck et al., 1998). The measured flux of this source is dependent on the noise level at that position on the map. Similarly, the faint source 55 is greatly dependent on the rms map level at the position. While the emission is likely to be thermal emission from H II, we are unable to confidently identify source 55.

### X-ray Counterparts

A comparison of our radio source list with the X-ray lists of Soria & Wu (2003) and Kilgard et al. (2005) yield 10 X-ray counterparts. These sources, along with the *Chandra* source designation, are listed in Table 2.6. Sources 19, 22 and 35 were discussed previously.

In order to constrain the nature of the X-ray/radio sources, we examine the X-ray colors using the values published in Kilgard et al. (2005). The X-ray color-color plot is presented in Figure 2.5. As can be seen, a clear dichotomy exists between X-ray binary candidates and SNR candidates: sources 3, 4, 7, 19, 22 and 35 are SNR candidates; sources 24, 32 and 36 are XRB candidates; and source 28 is a highly absorbed background source. Individual sources are discussed below. This same dichotomy between SNRs and XRBs was seen by Kilgard et al. (2006, in preparation) in M51 X-ray sources that are coincident with compact H$\alpha$ sources. In M51, many of the SNR-candidates are also coincident with compact radio sources. Thus, these observations help place constraints on X-ray source classification based upon X-ray colors.

Sources 3 and 4 show consistently non-thermal radio emission over the three epochs, although for source 3 we cannot calculate a spectral index due to lack of detections for at least one band in each epoch. In the radio, source 3 has shown a rise in 20cm flux density from 1983 to 1990. That emission dropped to below detectability in 1998. At the same time the source brightened to a detectable level in 1998 after no detections in the two previous epochs. We do note that there are optical HII regions (Rumstay & Kaufman, 1983) coincident with both radio sources. Source 3 has HC= $-0.44 \pm 0.31$ and SC = $-0.50 \pm 0.15$, placing it in the range of thermal SNRs; source 4 falls on the cusp between SNRs and soft X-ray binaries (likely LMXBs), with HC= $-0.57 \pm 0.25$ and SC= $-0.22 \pm 0.18$. Both sources exhibit no variability between the two *Chandra* observations.

Similarly, source 7 has X-ray colors of HC= $-0.17 \pm 0.27$ and SC = $-0.47 \pm 0.15$, placing it also on the cusp of LMXBs and SNRs. Consistent non-thermal radio emission over this time strengthens the determination of this source as an SNR. There was an increase in 20cm emission, while at 6cm the flux remained flat. There is no identified optical counterpart to this source so we cannot place other constraints on the source type.

Source 24 has X-ray colors indicative of an X-ray binary, with HC = $-0.20 \pm 0.26$ and SC= $0.11 \pm 0.25$. However, the location of the source within a dust lane could lead to absorption of the soft X-rays. As such, we cannot rule out an identification of an SNR based upon the X-ray data.

Source 28 has been of particular interest since it was associated with sources 27 and 29 (Cowan et al., 1994). It was postulated that the sources could be part of a jet from the nucleus of M83. High resolution *Chandra* observations show an X-ray source at the position of source 28. X-ray spectral analysis indicate that it is likely a background galaxy (Stockdale

et al., 2001a; Soria & Wu, 2003). Radio observations show a source that varies slightly at 20cm while fading rapidly at 6cm. Sources 27 and 29 show consistent non-thermal emission. At 20cm source 27 has brightened slightly, while source 29 has remained steady or slightly faded (there is a large overlap in the uncertainty). Both sources faded between 1990 and 1998 at 6cm. The association of sources 27 and 29 indicate that they are the radio lobes of a FR II radio galaxy that lies along the line of sight (Stockdale et al., 2001a; Maddox et al., 2003; Soria & Wu, 2002, 2003).

Source 32 has the faintest X-ray detected counterpart to a radio source in M83 ($L_X < 10^{37} erg\ s^{-1}$). The X-ray colors indicate that the source is a soft X-ray binary (HC= $-0.73 \pm 0.32$, SC = $0.00 \pm 0.26$). The soft X-ray color may be artificially "softened" due to excess soft, diffuse X-ray emission near the source. There is also the suggestion of X-ray variability, with the source not detected at all in the second *Chandra* observation. However, given the short observation time (20% that of the longer observation), the source would be at or slightly below the detection limit. This source lies near the confused nuclear region of the galaxy. This leads to a large X-ray background in that area. The measured spectral index for source 32 is quite steep ($-1.7$), but this could be attributed to the uncertainty in the background level. The source could also be exhibiting radio variability similar to the suggested X-ray variability.

Source 36 has been a mystery in previous studies. It has no optical counterpart. It is not located in the high surface brightness area of a spiral arm. The presence of the X-ray counterpart was noted first by Stockdale et al. (2001a), and Maddox et al. (2003) suggested that it was another background galaxy. Radio measurements show a slight rise in 20cm emission from the earliest epoch. Over the same span of time the 6cm has dramatically

dropped. Further analysis of the X-ray indicated that the source is consistent with an X-ray binary (HC= $-0.13 \pm 0.16$, SC= $0.15 \pm 0.16$), with evidence for X-ray spectral evolution between the two observations without a change in flux.

As illustrated in Figure 2.1 and listed in Tables 2.2, 2.4, 2.5, and 2.6, we detect radio emission from 55 point source sources overlapping with 6 X-ray only sources, 20 optical only sources, and 4 X-ray/optical sources. 54% of the sources in our radio sample have counterparts in the optical and X-ray, which can be compared to the SNR populations measured by Pannuti et al. (2002) for M33, NGC 300, and NGC 7793. For M33, they report radio emission from 53 SNRs with 37 optical and 11 optical/X-ray co-detections; for NGC 300, they report radio emission from 17 SNRs with one optical, one X-ray, and two optical/X-ray co-detections; and for NGC 7793, they report seven radio SNRs with one each optical, X-ray, and optical/X-ray co-detection. It should be noted that the resolution for the observations was $6\overset{s}{.}$, that the statistical errors of the SNR spectral index measurements were so large that the spectral indices for most identified radio sources are not clearly identified as SNRs by their own identification ($\alpha < -0.2$), and that a large fraction of their detections would not be classified as detections in this catalog as their flux measurements do not exceed $4\sigma$. Given these limitations, the fact that we have an approximate 50% overlap at the other bands is in relative agreement with the range of co-detections of Pannuti et al. (2002).

### 2.4.2 Nuclear Emission

The nucleus of M83 is very complex. The bright emission prevents the resolution of individual sources using the VLA configurations for the observation bands here. Cowan et al. (1994) noted that the optical/IR nucleus was not coincident with the radio nucleus. We

are able to confirm this with the new analysis of the data. The peak of the radio nuclear emission is located at a distance of $\sim 10''$ from the optical center. Contour plots of all maps are shown in Figure 2.6.

There does exist evidence for multiple emission sources within the nuclear complex. From the 1983−1984 observations to those in 1992, there was an overall increase in the nuclear emission. Figure 2.7 shows a series of three-dimensional emission profiles of the nuclear region. The plots for the 20cm band indicate the presence of at least four possible sources. The position of the third brightest "peak" is consistent with the optical center. Soria & Wu (2002) report the presence of a hard X-ray source at this position. X-ray spectral analysis (Soria & Wu, 2002) indicate that the source is consistent with a low accretion-rate black hole with mass $\sim 10^7 M_\odot$. This compares favorably with the mass estimates of Thatte et al. (2000) ($1.6 \times 10^7 M_\odot$) and Mast et al. (2005) ($1.2 \times 10^7 M_\odot$). Although we cannot get accurate measurements of the nuclear peak flux levels in the radio maps, qualitative inspection indicates that the emission is non-thermal in nature which would be consistent with the X-ray results.

The second highest "peak" seems to be consistent with the obscured "dark" nucleus reported by Thatte et al. (2000) and subsequently studied in Sakamoto et al. (2004). In a later study, however, Mast et al. (2005) reported a different position for this "dark" nucleus. Figure 2.8 shows positions of the optical nucleus and the "dark" nucleus on the 1983 20cm contours. As illustrated in Figure 2.8 nucleus appears closer to the peak of the radio emission of the galaxy. The studies of this mass concentration indicate that it is more massive (e.g., Mast et al., 2005) than the the optical nucleus. Thatte et al. (2000) also note that the "dark" nucleus is located near the dynamical center of the galaxy. The positions

of the nuclear mass concentrations are given in Table 2.7. The positions for the "dark" nucleus are offset in Declination by $\sim 3.6''$, which corresponds to the deconvolution size for our observations. We would need the higher resolution of VLBI observations in order to isolate the radio emission sources.

A VLBI observation using the Long Baseline Array of the Australia Telescope has been performed on the nuclear region of M83. The aim of these observations is to resolve the individual sources in this region to get a better idea of the distribution and to find multiple counterparts to the nuclear X-ray sources reported in Soria & Wu (2003). The results of this study will be presented in a future paper (Maddox et al, in preparation).

## 2.5 Conclusions

We have studied the long term radio emission from compact sources in the galaxy M83. The observations included previously unpublished data from 1990 and 1998. We have presented the data over the fifteen years in a consistent manner. Our observations have resulted in the detection of a number of objects in M83:

• It was shown that SN 1957D has continued fading, consistent with an expanding shock through a circumstellar material that is decreasing in density. SN 1950B has apparently faded to the level of thermal HII regions that are near the position of the explosion. SN 1923A has faded to near the limits of detection of these observations. We continue to show no detection of SN 1983N after its initial radio detection, consistent with it having been a Type Ib supernova.

• About half of the radio sources are thermal HII regions. A result that is not surprising due to the high star formation activity of M83. The HII regions tend to be very large,

exhibiting high excitation parameters. The largest regions are not detected due to the high resolution of our observations.

• It was found that ten sources were coincident with X-ray sources. The continuum spectral indices of these sources indicated that most were X-ray supernova remnants. We confirm that one of the coincident sources (source 28) is the nucleus of a background radio galaxy with two radio lobes (sources 27 and 29). Three of the X-ray sources are coincident with known optical supernova remnants.

• We note that the nuclear region of M83 has shown a slight increase in 20 cm emission in the radio peak. It is possible that there is an increase in accretion onto a supermassive black hole, which would be consistent with X-ray results. The 6 cm emission does not show this increase in flux. We confirmed that the reported optical/IR nuclear peak is not consistent with the radio nucleus, though there is evidence for a radio emission region at the position of the optical nucleus. It was seen that the nuclear radio peak was near the position of a second "dark" nuclear mass concentration that corresponds to the dynamical nucleus of the galaxy.

Our multiwavelength analyses have provided new information about the nature of the many detected compact sources and the nucleus in the starburst galaxy M83. Studies of the compact sources are providing new information about late-term stellar evolution (*e.g.*, mass-loss rates), emission mechanisms, the transition of SNe into SNRs, and the nature of XRBs. The combination of radio, X-ray and optical observations provide an excellent diagnostic for the classification of compact sources in this and other nearby galaxies. This galaxy also appears to have a complicated nuclear structure, including possibly multiple supermassive black holes, and may have minor variability. In the future we will continue

Table 2.1. VLA Radio Observations of M83

| | 1983 – 1984 Observations | | 1990 Observations | | 1998 Observations | |
|---|---|---|---|---|---|---|
| Parameter | 20cm | 6cm | 20cm | 6cm | 20cm | 6cm |
| Frequency (GHz)..... | 1.446 | 4.873 | 1.452 | 4.873 | 1.465 | 4.885 |
| Observing dates..... | 1983 Dec 15,17 | 1984 Mar 15 | 1990 Jun 30 | 1990 Oct 14 | 1998 Jun 13 | 1998 Oct 31 |
| Observing time (hr)..... | 3 | 6.5 | 7.5 | 6 | 11.3 | 11.6 |
| Configuration..... | BnA | CnB | BnA | CnB | BnA | CnB |
| Primary beam HPBW... | $30'$ | $8'$ | $30'$ | $8'$ | $30'$ | $8'$ |
| Clean Beam..... | $3\farcs50 \times 3\farcs50$ | $3\farcs93 \times 2\farcs80$ | $3\farcs65 \times 3\farcs65$ | $3\farcs65 \times 3\farcs65$ | $3\farcs65 \times 3\farcs65$ | $3\farcs65 \times 3\farcs65$ |
| rms noise (mJy beam$^{-1}$) | 0.197 | 0.045 | 0.074 | 0.037 | 0.079 | 0.070 |

to follow the long-term evolution of these sources in this galaxy, as well as to compare the results here with those in other nearby face-on spiral galaxies.

Table 2.2. Radio Positions and Peak Flux Densities of Sources in M83

| | Position[a] | | 1983-1984[b] | | 1990 | | 1998 | |
|---|---|---|---|---|---|---|---|---|
| Source | R.A.(2000) | Decl.(2000) | 20 cm (mJy) | 6 cm (mJy) | 20 cm (mJy) | 6 cm (mJy) | 20 cm (mJy) | 6 cm (mJy) |
| 1 | $13^h36^m50^s.00$ | $-29°52'43''.36$ | ··· | $0.41 \pm 0.08$ | $0.37 \pm 0.08$ | $0.35 \pm 0.04$ | $0.52 \pm 0.07$ | $0.34 \pm 0.06$ |
| 2 | 13 36 50.83 | −29 51 59.56 | ··· | ··· | $0.38 \pm 0.08$ | ··· | ··· | ··· |
| 3 | 13 36 50.86 | −29 52 38.54 | $0.76 \pm 0.20$ | $0.39 \pm 0.08$ | $0.38 \pm 0.08$ | $0.25 \pm 0.03$ | $0.40 \pm 0.09$ | $0.20 \pm 0.06$ |
| 4 | 13 36 51.11 | −29 50 41.98 | $0.96 \pm 0.19$ | ··· | $0.55 \pm 0.08$ | $0.23 \pm 0.04$ | $0.58 \pm 0.07$ | $0.34 \pm 0.04$ |
| 5[c] | 13 36 51.24 | −29 54 02.01 | $4.58 \pm 0.20$ | $1.30 \pm 0.12$ | ··· | ··· | ··· | ··· |
| 6 | 13 36 51.55 | −29 53 00.61 | ··· | ··· | $0.43 \pm 0.08$ | $0.41 \pm 0.05$ | $0.54 \pm 0.10$ | $0.36 \pm 0.06$ |
| 7 | 13 36 52.78 | −29 52 31.58 | ··· | ··· | $0.52 \pm 0.08$ | $0.25 \pm 0.04$ | $0.47 \pm 0.10$ | $0.29 \pm 0.05$ |
| 8 | 13 36 52.77 | −29 51 10.39 | ··· | $0.45 \pm 0.07$ | $0.38 \pm 0.08$ | $0.49 \pm 0.04$ | $0.42 \pm 0.09$ | $0.30 \pm 0.05$ |
| 9 | 13 36 52.83 | −29 51 37.96 | ··· | ··· | $0.62 \pm 0.08$ | ··· | $0.90 \pm 0.08$ | ··· |
| 10 | 13 36 52.91 | −29 52 49.07 | $0.73 \pm 0.19$ | $0.39 \pm 0.08$ | $0.60 \pm 0.08$ | $0.28 \pm 0.05$ | $0.45 \pm 0.09$ | $0.28 \pm 0.05$ |
| 11[c] | 13 36 52.92 | −29 51 56.50 | $0.70 \pm 0.17$ | $0.43 \pm 0.06$ | $0.54 \pm 0.08$ | $0.54 \pm 0.05$ | $0.53 \pm 0.07$ | $0.50 \pm 0.04$ |
| 12 | 13 36 53.14 | −29 51 33.12 | $0.98 \pm 0.19$ | $1.03 \pm 0.06$ | $0.95 \pm 0.08$ | $1.16 \pm 0.05$ | $0.89 \pm 0.13$ | $1.17 \pm 0.05$ |
| 13 | 13 36 53.27 | −29 52 57.44 | $0.47 \pm 0.19$ | $0.53 \pm 0.08$ | $0.45 \pm 0.08$ | $0.40 \pm 0.06$ | $0.60 \pm 0.08$ | $0.47 \pm 0.05$ |
| 14 | 13 36 53.25 | −29 50 58.62 | ··· | $0.31 \pm 0.06$ | $0.42 \pm 0.08$ | $0.41 \pm 0.04$ | $0.20 \pm 0.08$ | $0.35 \pm 0.04$ |
| 15 | 13 36 53.39 | −29 51 11.17 | ··· | ··· | ··· | $0.18 \pm 0.04$ | ··· | $0.19 \pm 0.05$ |
| 16 | 13 36 54.20 | −29 50 42.22 | ··· | $0.45 \pm 0.06$ | $0.37 \pm 0.08$ | $0.30 \pm 0.05$ | $0.41 \pm 0.07$ | $0.33 \pm 0.04$ |
| 17 | 13 36 54.40 | −29 53 05.17 | $0.43 \pm 0.21$ | $0.37 \pm 0.08$ | $0.36 \pm 0.08$ | $0.49 \pm 0.05$ | $0.52 \pm 0.11$ | $0.58 \pm 0.06$ |
| 18 | 13 36 54.74 | −29 52 56.77 | $0.59 \pm 0.19$ | $0.47 \pm 0.08$ | $0.60 \pm 0.08$ | $0.33 \pm 0.05$ | $0.44 \pm 0.10$ | $0.29 \pm 0.06$ |
| 19 | 13 36 54.90 | −29 53 10.29 | ··· | $0.58 \pm 0.08$ | ··· | $0.40 \pm 0.04$ | $0.36 \pm 0.10$ | $0.43 \pm 0.05$ |
| 20 | 13 36 54.95 | −29 52 40.21 | ··· | ··· | ··· | $0.19 \pm 0.05$ | $0.28 \pm 0.09$ | ··· |
| 21 | 13 36 55.41 | −29 52 56.08 | ··· | ··· | $0.26 \pm 0.08$ | ··· | $0.26 \pm 0.09$ | $0.21 \pm 0.03$ |
| 22 | 13 36 55.54 | −29 53 03.26 | ··· | ··· | $0.22 \pm 0.08$ | $0.26 \pm 0.04$ | $0.33 \pm 0.09$ | $0.32 \pm 0.05$ |
| 23 | 13 36 55.72 | −29 49 52.14 | $0.88 \pm 0.18$ | $0.51 \pm 0.06$ | $0.70 \pm 0.08$ | $0.43 \pm 0.04$ | $0.46 \pm 0.06$ | $0.53 \pm 0.05$ |
| 24 | 13 36 56.13 | −29 52 54.99 | ··· | ··· | $0.45 \pm 0.08$ | $0.31 \pm 0.04$ | $0.42 \pm 0.07$ | ··· |
| 25 | 13 36 56.32 | −29 49 34.10 | ··· | ··· | ··· | $0.13 \pm 0.03$ | $0.30 \pm 0.05$ | ··· |
| 26 | 13 36 56.84 | −29 52 48.36 | ··· | ··· | ··· | $0.27 \pm 0.04$ | $0.35 \pm 0.08$ | $0.25 \pm 0.04$ |
| 27 | 13 36 56.91 | −29 50 43.28 | $3.39 \pm 0.18$ | $0.86 \pm 0.05$ | $3.23 \pm 0.08$ | $1.09 \pm 0.03$ | $3.38 \pm 0.07$ | $1.02 \pm 0.04$ |
| 28 | 13 36 58.34 | −29 51 04.58 | $0.74 \pm 0.18$ | $1.31 \pm 0.06$ | $1.06 \pm 0.08$ | $1.55 \pm 0.04$ | $0.82 \pm 0.07$ | $0.87 \pm 0.05$ |
| 29 | 13 36 59.00 | −29 51 16.04 | $1.39 \pm 0.21$ | $0.37 \pm 0.05$ | $1.45 \pm 0.07$ | $0.60 \pm 0.04$ | $1.38 \pm 0.07$ | $0.49 \pm 0.04$ |
| 30 | 13 36 59.54 | −29 51 26.32 | ··· | ··· | $0.73 \pm 0.07$ | ··· | $1.26 \pm 0.09$ | ··· |
| 31 | 13 36 59.98 | −29 52 16.65 | $2.29 \pm 0.19$ | $1.35 \pm 0.06$ | $2.19 \pm 0.08$ | $1.45 \pm 0.05$ | $2.11 \pm 0.09$ | $1.56 \pm 0.05$ |
| 32 | 13 37 00.17 | −29 51 40.02 | $1.75 \pm 0.21$ | $0.42 \pm 0.06$ | $2.16 \pm 0.08$ | $0.57 \pm 0.03$ | $2.85 \pm 0.12$ | $0.38 \pm 0.08$ |
| 33 | 13 37 00.54 | −29 54 18.50 | ··· | ··· | $0.20 \pm 0.08$ | $0.27 \pm 0.05$ | ··· | ··· |

Table 2.2 (cont'd)

| | Position[a] | | 1983-1984[b] | | 1990 | | 1998 | |
|---|---|---|---|---|---|---|---|---|
| | | | 20 cm | 6 cm | 20 cm | 6 cm | 20 cm | 6 cm |
| Source | R.A.(2000) | Decl.(2000) | (mJy) | (mJy) | (mJy) | (mJy) | (mJy) | (mJy) |
| 34 | 13 37 01.34 | −29 51 26.51 | 1.34 ± 0.22 | 0.95 ± 0.05 | 0.92 ± 0.08 | 0.87 ± 0.04 | 1.14 ± 0.09 | 0.85 ± 0.04 |
| 35 | 13 37 02.36 | −29 51 25.85 | 0.94 ± 0.21 | ··· | 0.77 ± 0.08 | 0.48 ± 0.04 | 0.66 ± 0.08 | 0.37 ± 0.05 |
| 36 | 13 37 03.24 | −29 52 26.56 | ··· | 1.13 ± 0.06 | 0.50 ± 0.08 | 0.63 ± 0.04 | 0.68 ± 0.07 | 0.32 ± 0.04 |
| 37 | 13 37 03.28 | −29 51 13.7 | ··· | ··· | 0.24 ± 0.08 | ··· | ··· | 0.22 ± 0.05 |
| 38 | 13 37 03.39 | −29 54 02.04 | 1.01 ± 0.23 | 1.07 ± 0.07 | 0.66 ± 0.08 | 1.04 ± 0.05 | 0.80 ± 0.06 | 1.00 ± 0.05 |
| 39[c] | 13 37 03.53 | −29 49 40.56 | 2.72 ± 0.21 | 2.18 ± 0.06 | 1.88 ± 0.08 | 1.57 ± 0.04 | 0.82 ± 0.09 | 0.60 ± 0.05 |
| 40 | 13 37 04.73 | −29 50 57.59 | ··· | 0.32 ± 0.06 | 0.27 ± 0.08 | 0.36 ± 0.04 | 0.67 ± 0.08 | 0.41 ± 0.05 |
| 41 | 13 37 06.61 | −29 53 32.32 | ··· | 0.75 ± 0.09 | 0.59 ± 0.08 | 0.42 ± 0.05 | 0.56 ± 0.08 | 0.31 ± 0.05 |
| 42 | 13 37 06.91 | −29 49 36.03 | 1.30 ± 0.23 | 1.42 ± 0.05 | 1.51 ± 0.08 | 1.53 ± 0.04 | 1.54 ± 0.07 | 1.50 ± 0.05 |
| 43 | 13 37 07.37 | −29 51 06.38 | ··· | 0.32 ± 0.06 | 0.27 ± 0.08 | 0.43 ± 0.04 | 0.38 ± 0.06 | 0.34 ± 0.05 |
| 44 | 13 37 07.40 | −29 52 06.91 | ··· | ··· | 0.23 ± 0.08 | 0.20 ± 0.04 | ··· | ··· |
| 45 | 13 37 07.66 | −29 51 13.28 | 0.60 ± 0.21 | 0.31 ± 0.06 | 0.55 ± 0.07 | 0.47 ± 0.04 | 0.49 ± 0.07 | 0.40 ± 0.06 |
| 46 | 13 37 07.74 | −29 53 13.99 | ··· | ··· | 0.26 ± 0.08 | 0.22 ± 0.04 | ··· | 0.23 ± 0.04 |
| 47 | 13 37 07.82 | −29 52 41.69 | ··· | ··· | 0.28 ± 0.08 | 0.26 ± 0.05 | 0.23 ± 0.06 | ··· |
| 48 | 13 37 07.89 | −29 51 17.78 | 0.66 ± 0.22 | 0.65 ± 0.07 | 0.98 ± 0.07 | 0.53 ± 0.04 | 0.65 ± 0.07 | 0.62 ± 0.05 |
| 49 | 13 37 08.09 | −29 52 55.78 | ··· | ··· | 0.34 ± 0.09 | 0.23 ± 0.05 | 0.34 ± 0.07 | 0.29 ± 0.05 |
| 50 | 13 37 08.31 | −29 52 11.54 | 0.68 ± 0.22 | 0.35 ± 0.08 | 0.46 ± 0.09 | 0.41 ± 0.04 | 0.40 ± 0.08 | 0.38 ± 0.05 |
| 51 | 13 37 08.69 | −29 51 31.04 | ··· | 0.39 ± 0.06 | 0.26 ± 0.08 | 0.31 ± 0.04 | 0.48 ± 0.08 | 0.23 ± 0.05 |
| 52 | 13 37 09.19 | −29 51 33.31 | 0.86 ± 0.22 | 0.38 ± 0.07 | 0.48 ± 0.07 | 0.33 ± 0.04 | 0.70 ± 0.07 | 0.35 ± 0.04 |
| 53[c] | 13 37 09.22 | −29 51 00.51 | ··· | ··· | ··· | 0.28 ± 0.04 | 0.22 ± 0.06 | 0.19 ± 0.05 |
| 54 | 13 37 10.01 | −29 51 28.24 | ··· | 0.45 ± 0.06 | ··· | 0.20 ± 0.04 | 0.29 ± 0.09 | 0.25 ± 0.06 |
| 55 | 13 37 11.44 | −29 49 52.31 | ··· | ··· | ··· | 0.23 ± 0.05 | 0.21 ± 0.06 | 0.18 ± 0.06 |

[a]From 1998 6 cm observations.

[b]Flux measurements using original maps discussed in Cowan & Branch (1985). Included here for completeness.

[c]In order of appearance: SN 1983N, SN 1950B, SN 1957D, and SN 1923A.

Table 2.3. Spectral Indices of Sources in M83

| | Spectral Index | |
|---|---|---|
| Source | 1990 | 1998 |
| 1 | –0.05±0.24 | –0.36±0.22 |
| 2 | $< -1.01$ | ··· |
| 3 | –0.35±0.24 | –0.58±0.38 |
| 4 | –0.73±0.23 | –0.45±0.17 |
| 5 | ··· | ··· |
| 6 | –0.04±0.22 | –0.34±0.25 |
| 7 | –0.61±0.22 | –0.41±0.27 |
| 8 | 0.21±0.23 | –0.28±0.27 |
| 9 | $< -1.42$ | $< -1.20$ |
| 10 | –0.64±0.22 | –0.40±0.27 |
| 11 | 0.00±0.17 | –0.05±0.15 |
| 12 | 0.17±0.09 | 0.23±0.15 |
| 13 | –0.10±0.23 | –0.21±0.17 |
| 14 | –0.02±0.21 | 0.47±0.42 |
| 15 | $> -0.17$ | $> -0.18$ |
| 16 | –0.18±0.27 | –0.18±0.21 |

Table 2.3 (cont'd)

| | Spectral Index | |
|---|---|---|
| Source | 1990 | 1998 |
| 17 | 0.26±0.24 | 0.09±0.24 |
| 18 | –0.50±0.20 | –0.35±0.31 |
| 19 | $> 0.49$ | 0.15±0.30 |
| 20 | $> -0.13$ | $< -0.23$ |
| 21 | $< -0.70$ | -0.18±0.37 |
| 22 | 0.14±0.39 | –0.03±0.31 |
| 23 | –0.41±0.15 | 0.12±0.16 |
| 24 | –0.31±0.22 | $< -0.57$ |
| 25 | $> -0.44$ | $< -0.29$ |
| 26 | $> 0.16$ | -0.28±0.28 |
| 27 | –0.91±0.04 | –1.01±0.04 |
| 28 | 0.32±0.08 | 0.05±0.10 |
| 29 | –0.74±0.08 | –0.87±0.10 |
| 30 | $< -1.55$ | $< -1.48$ |
| 31 | –0.35±0.05 | –0.25±0.05 |
| 32 | –1.12±0.06 | –1.70±0.21 |

Table 2.3 (cont'd)

| | Spectral Index | |
|---|---|---|
| Source | 1990 | 1998 |
| 33 | 0.25±0.44 | ··· |
| 34 | –0.05±0.10 | –0.25±0.09 |
| 35 | –0.40±0.13 | –0.49±0.18 |
| 36 | 0.19±0.17 | –0.63±0.16 |
| 37 | $< -0.64$ | $> -0.06$ |
| 38 | 0.38±0.13 | 0.19±0.09 |
| 39 | –0.15±0.05 | –0.26±0.14 |
| 40 | 0.24±0.32 | –0.41±0.17 |
| 41 | –0.28±0.18 | –0.50±0.22 |
| 42 | 0.01±0.06 | –0.02±0.06 |
| 43 | 0.39±0.31 | –0.09±0.22 |
| 44 | –0.12±0.40 | ··· |
| 45 | –0.13±0.15 | –0.17±0.21 |
| 46 | –0.14±0.36 | $> -0.02$ |
| 47 | –0.06±0.34 | $< -0.08$ |
| 48 | –0.52±0.10 | –0.04±0.13 |

Table 2.3 (cont'd)

| | Spectral Index | |
|---|---|---|
| Source | 1990 | 1998 |
| 49 | –0.33±0.34 | –0.13±0.27 |
| 50 | –0.10±0.22 | –0.04±0.24 |
| 51 | 0.15±0.33 | –0.62±0.27 |
| 52 | –0.31±0.19 | –0.58±0.15 |
| 53 | $> 0.19$ | -0.12±0.38 |
| 54 | $> -0.09$ | -0.12±0.39 |
| 55 | $> 0.03$ | -0.13±0.44 |

Table 2.4 Optical Supernova Remnants with Radio Counterparts

| Source | Radio Spectral Index | SNR |
|---|---|---|
| 19.... | $+0.15 \pm 0.30$ | BL18 |
| 22.... | $-0.18 \pm 0.37$ | BL24 |
| 35.... | $-0.49 \pm 0.18$ | BL41 |
| 39.... | $-0.26 \pm 0.14$ | BL50 |

Table 2.5. Radio Sources with Associated HII Regions

| Source | Radio Spectral Index | H II Region | Excitation Parameter[a] |
|---|---|---|---|
| 2 | $< -1.02$ | RK230 | 241 |
| 3 | $-0.58 \pm 0.38$ | RK233 | 355 |
| 4 | $-0.45 \pm 0.17$ | RK223 | 444 |
| 6 | $+0.34 \pm 0.25$ | RK292/295 | 228/287 |
| 8 | $-0.28 \pm 0.27$ | RK211 | 393 |
| 12 | $+0.23 \pm 0.15$ | RK209 | 321 |
| 18[b] | $-0.35 \pm 0.31$ | ... | ... |
| 22 | $-0.03 \pm 0.31$ | RK185 | 369 |
| 26 | $-0.28 \pm 0.28$ | RK181 | 201 |
| 33 | $+0.25 \pm 0.44$ | RK144 | 300 |
| 34 | $-0.25 \pm 0.09$ | RK137 | 473 |
| 37 | $> -0.06$ | RK119 | 97 |
| 40 | $-0.41 \pm 0.17$ | RK110 | 470 |
| 42 | $-0.02 \pm 0.06$ | RK86 | 316 |
| 43 | $-0.09 \pm 0.22$ | RK79 | 288 |
| 45/48 | $-0.04 \pm 0.13$ | RK75 | 395 |
| 46 | $-0.14 \pm 0.36$ | RK78 | 228 |

Table 2.5 (cont'd)

| Source | Radio Spectral Index | H II Region | Excitation Parameter[a] |
|---|---|---|---|
| 49 | $-0.13 \pm 0.27$ | RK73 | 301 |
| 50 | $-0.04 \pm 0.24$ | RK70 | 353 |
| 53 | $-0.12 \pm 0.38$ | RK59 | 323 |
| 55 | $-0.13 \pm 0.44$ | RK37 | 294 |

[a]The excitation parameter $U$ is a measure of the total Lyman continuum flux and is a useful index of the distribution of O stars. The values are in units of pc cm$^{-2}$, as presented in Rumstay & Kaufman (1983).

[b]This source was detected as an HII in a survey by de Vaucouleurs et al. (1983), listed as source 23.

Table 2.6 X-Ray Counterparts to Radio Sources in M83

| Source | Radio Spectral Index | CXOU | Source Type | Reference |
|---|---|---|---|---|
| 3..... | $-0.58 \pm 0.38$ | J133650.8-295240 | HII Region/SNR | 1 |
| 4..... | $-0.45 \pm 0.17$ | J133651.1-295043 | HII Region/LMXB | 1 |
| 7..... | $-0.41 \pm 0.27$ | J133652.8-295231 | SNR | 1 |
| 19.... | $+0.15 \pm 0.30$ | J133655.0-295239 | SNR | 2 |
| 22.... | $-0.02 \pm 0.31$ | J133655.6-295303 | SNR | 2 |
| 24.... | $-0.31 \pm 0.22$ | J133656.2-295255 | ... | |
| 28.... | $+0.05 \pm 0.10$ | J133658.3-295105 | Background Galaxy | 3 |
| 32.... | $-1.70 \pm 0.21$ | J133700.0-295138 | ... | |
| 35.... | $-0.49 \pm 0.18$ | J133702.4-295126 | SNR | 2 |
| 36.... | $-0.63 \pm 0.16$ | J133703.3-295226 | XRB | |

(1) Colbert et al. (2004)

(2) Blair & Long (2004)

(3) Stockdale et al. (2001a)

Table 2.7 Reported Positions of Nuclear Mass Concentrations

| | RA (J2000) | Dec (J2000) | Reference |
|---|---|---|---|
| Optical Nucleus | 13 37 00.79 | −29 51 58.60 | Cowan et al. (1994) |
| Hidden Nucleus | 13 37 00.54 | −29 51 53.62 | Mast et al. (2005) |
| | 14 37 00.72 | −29 51 57.20 | Thatte et al. (2000) |

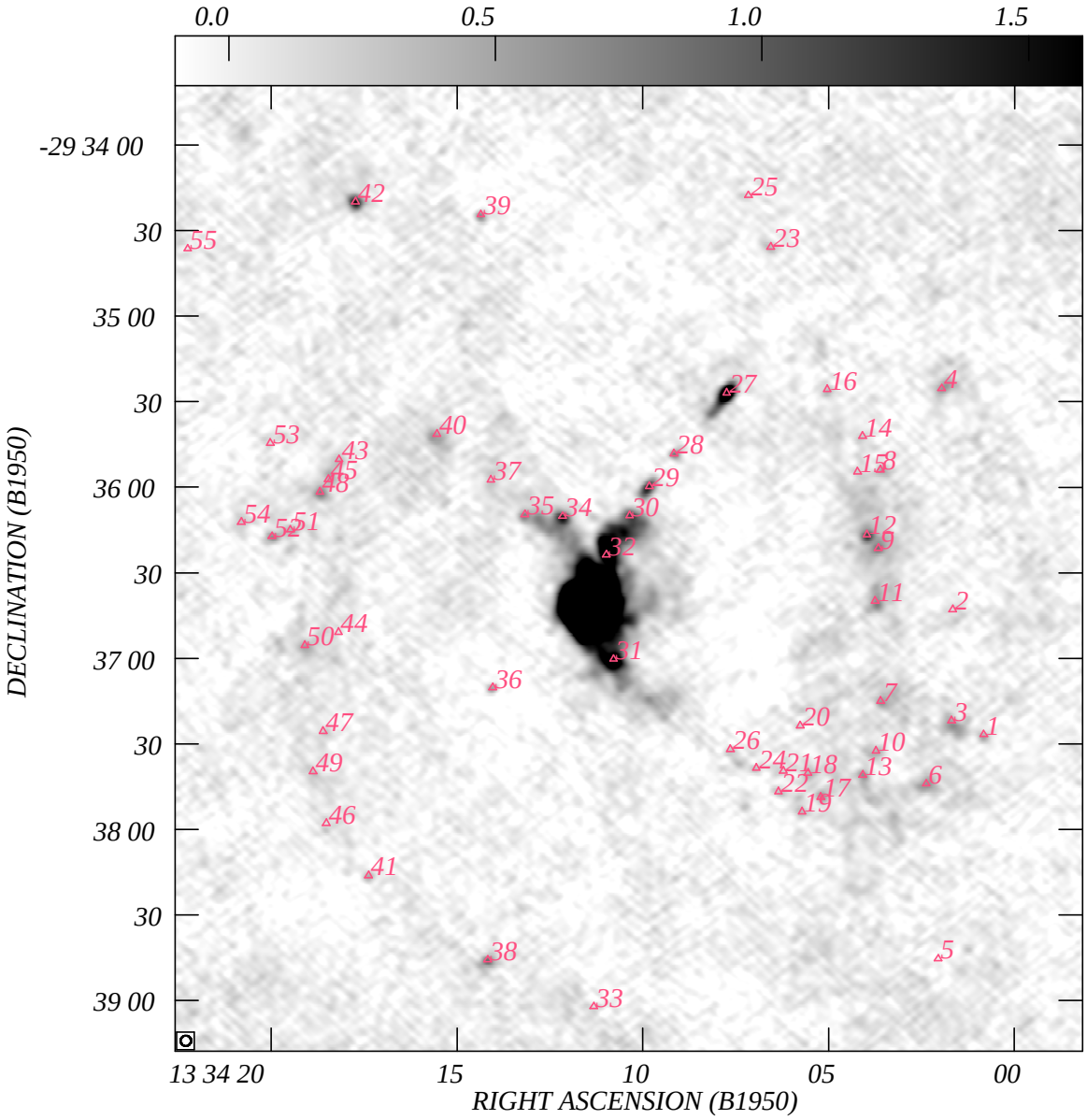



Figure 2.1 A 20cm map of M83 from the 1998 observation. Sources indicated correspond to those in Table 2.2. Greyscale spans from −0.1 mJy to 1.6 mJy.

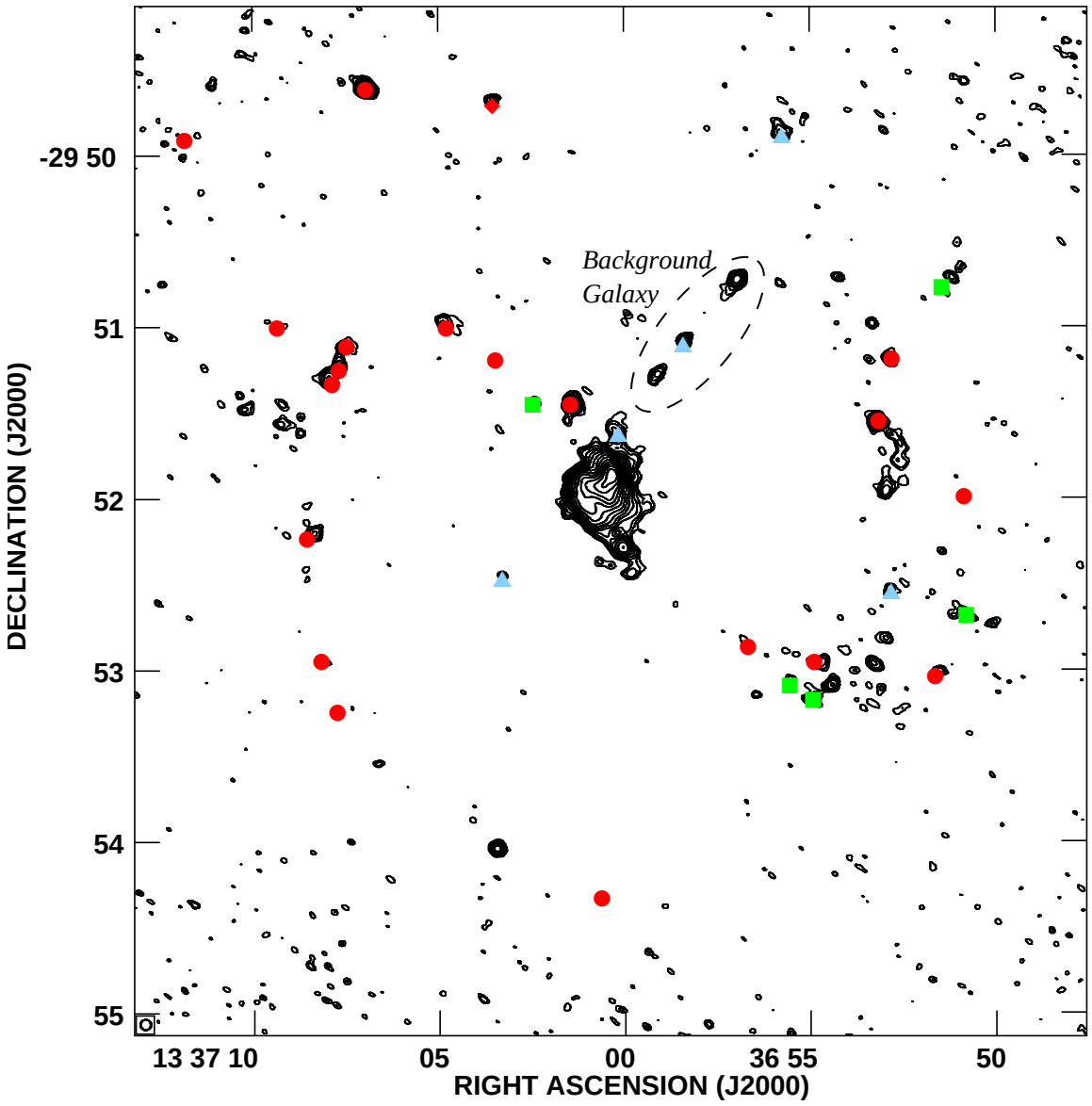



Figure 2.2 6cm contours of M83. Red symbols indicate radio sources with optical counterparts. Red circles are HII regions, while the red diamond indicates an optical SNR. Blue triangles indicate the presence of X-ray counterparts. Green squares denote sources that have emission in radio, optical and X-ray. Contour levels are 0.14, 0.20, 0.28, 0.40, 0.57, 0.80, 1.13, 1.60, 2.26, 3.20, 4.53, 6.40, 9.05 and 12.80 mJy/beam.

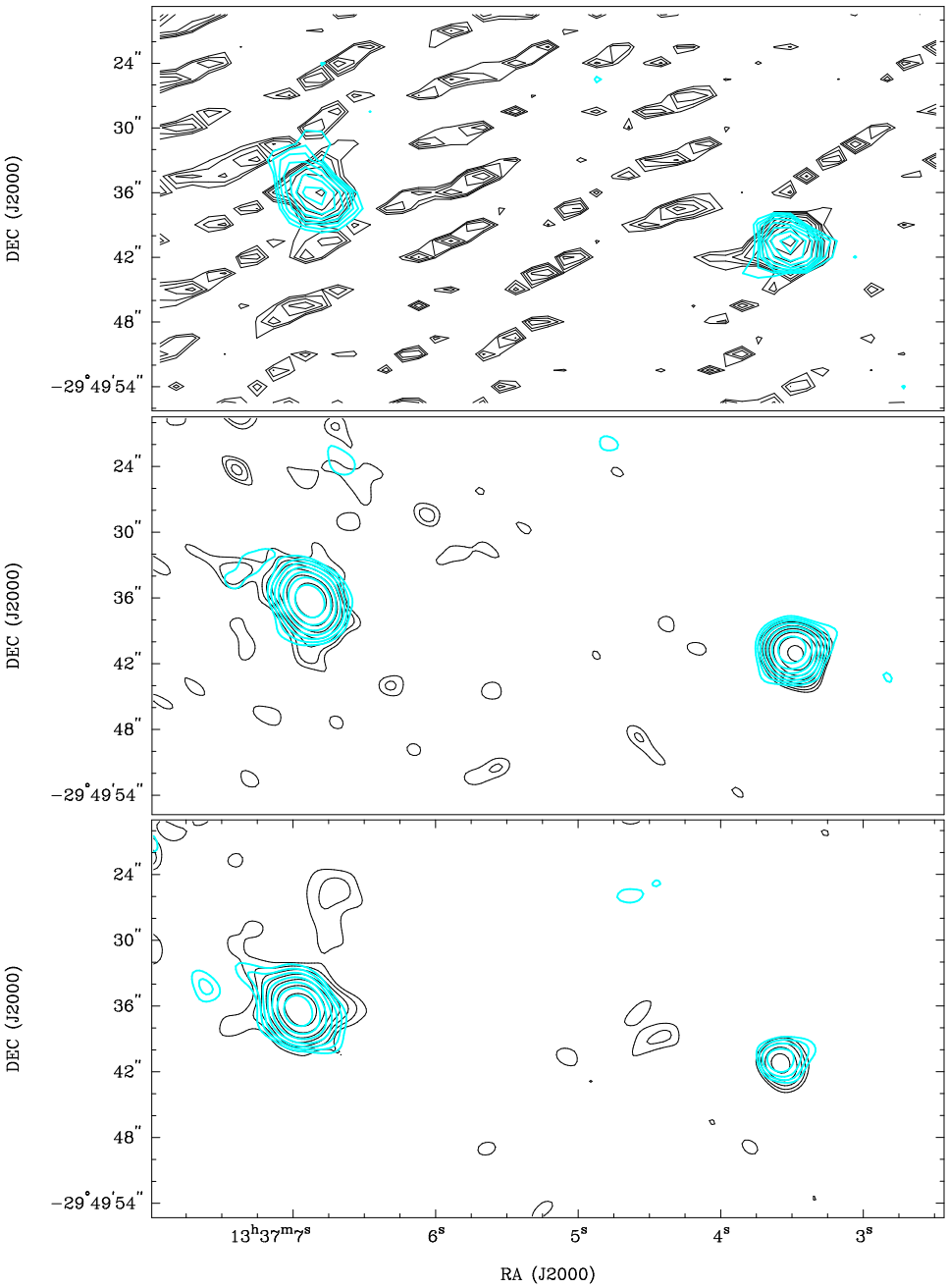



Figure 2.3 A series of contour plots showing the time evolution of SN 1957D. Black contours are 20cm emission and thick blue green contours are 6cm emission. Contour levels for both plots are 0.20, 0.28, 0.40, 0.57, 0.8, 1.13, 1.60 and 2.26 mJy/beam. SN 1957D is the right hand source. The left hand source is an HII region. Time runs from top to bottom.

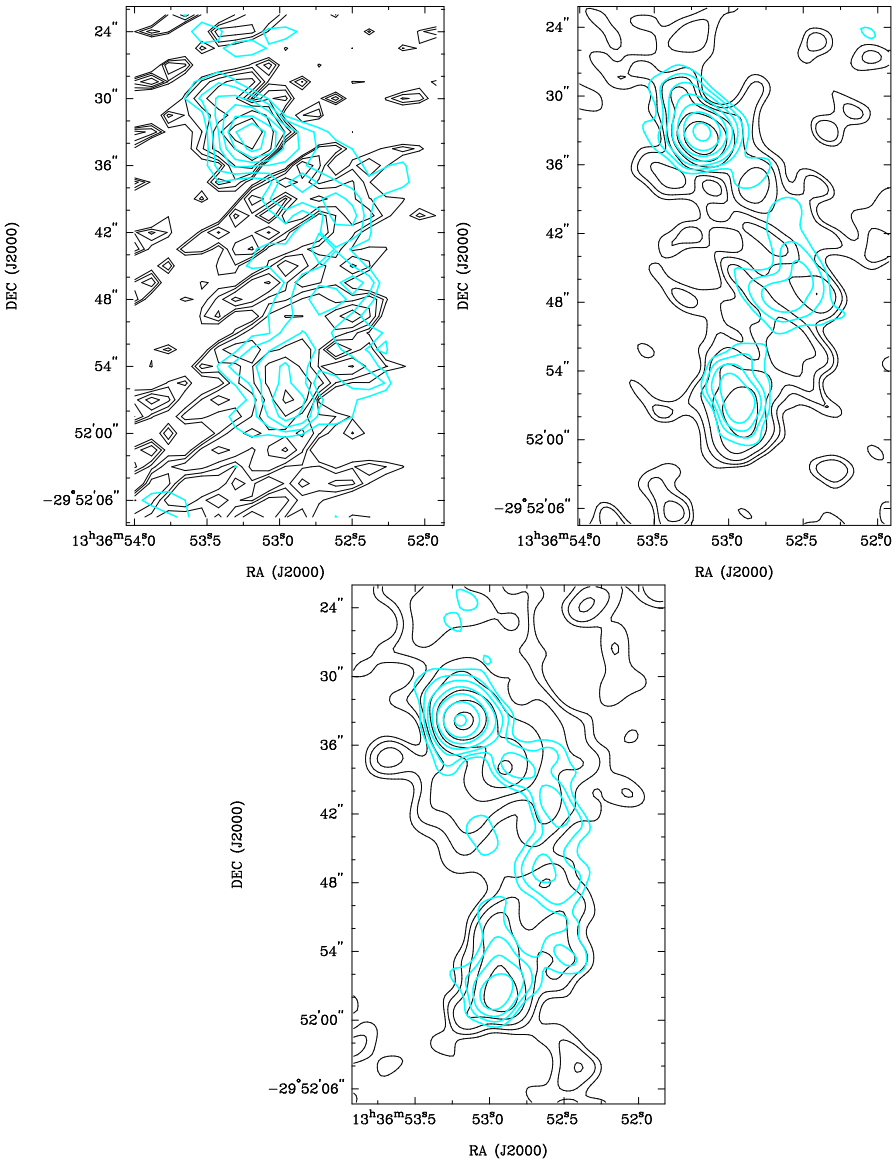



Figure 2.4 Same as Figure 2.3, but near the region of SN 1950B. Contour levels are the same. SN 1950B is the lower of the two major sources. Time progress clockwise form the upper left.

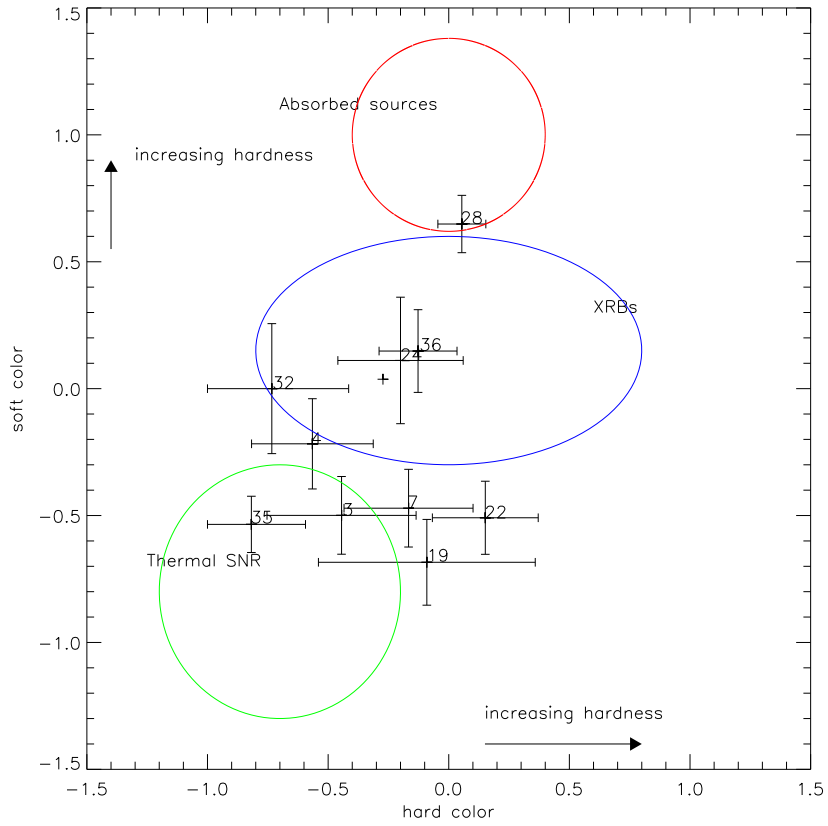



Figure 2.5 X-ray color-color diagram for the X-ray/Radio counterpart sources in M83.

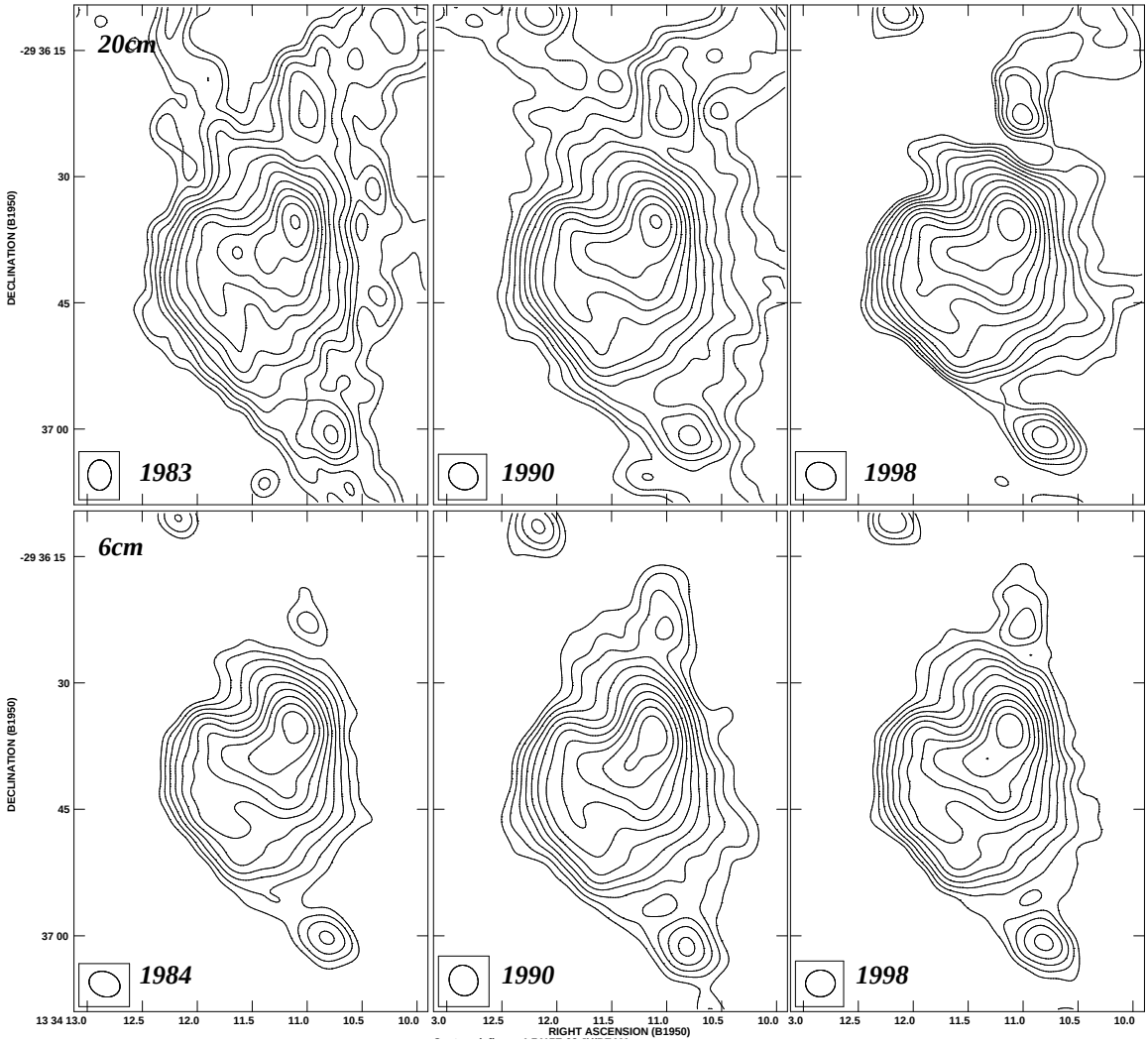



Figure 2.6 Same as Figure 2.3, but for the nuclear region. Contour levels are 0.40, 0.57, 0.8, 1.13, 1.60, 2.26, 3.20, 4.53, 6.40, 9.05, 12.80, 18.10 and 25.59 mJy/beam.

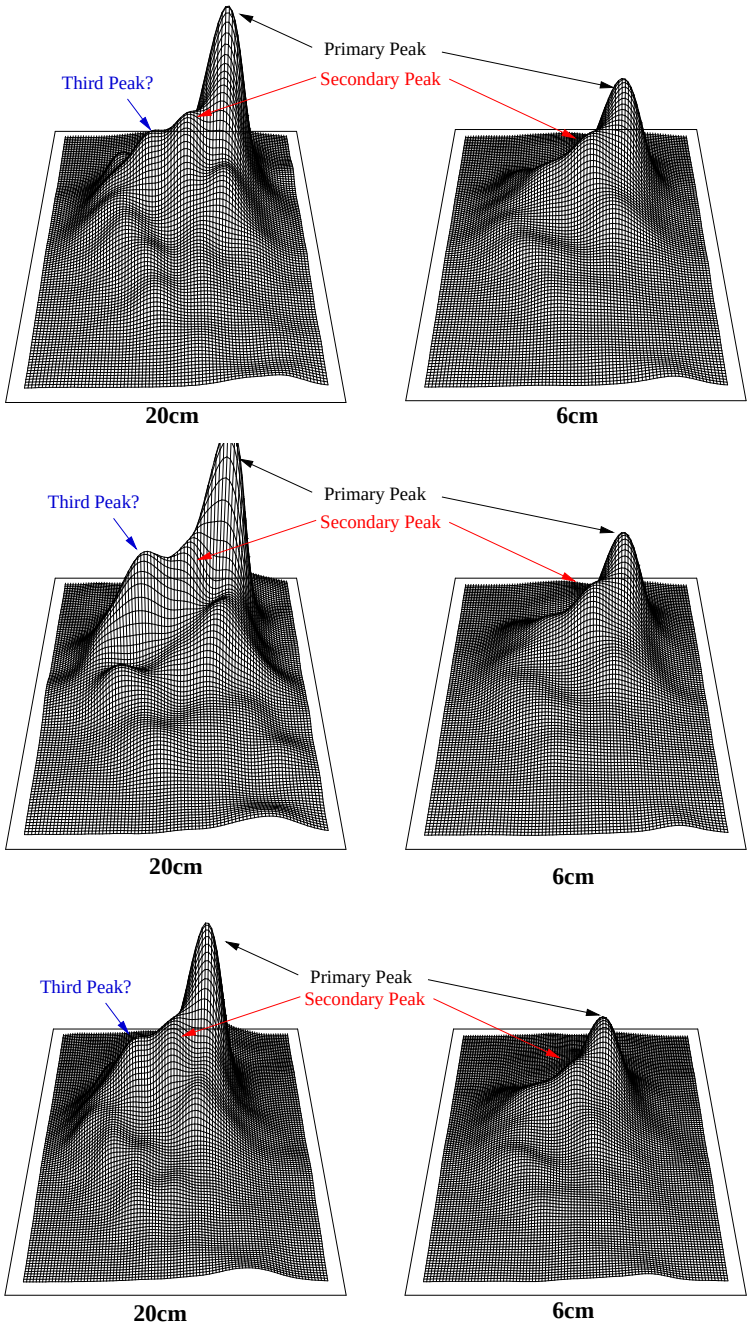



Figure 2.7 A series of profile plots of the nuclear region. Flux peaks are scaled to the 1990 20cm observation to show the differences between 20cm (left) and 6cm (right). Time progresses from top to bottom. One notable feature of these plots is the evidence for several lesser "peaks" of emission in the 20cm images.

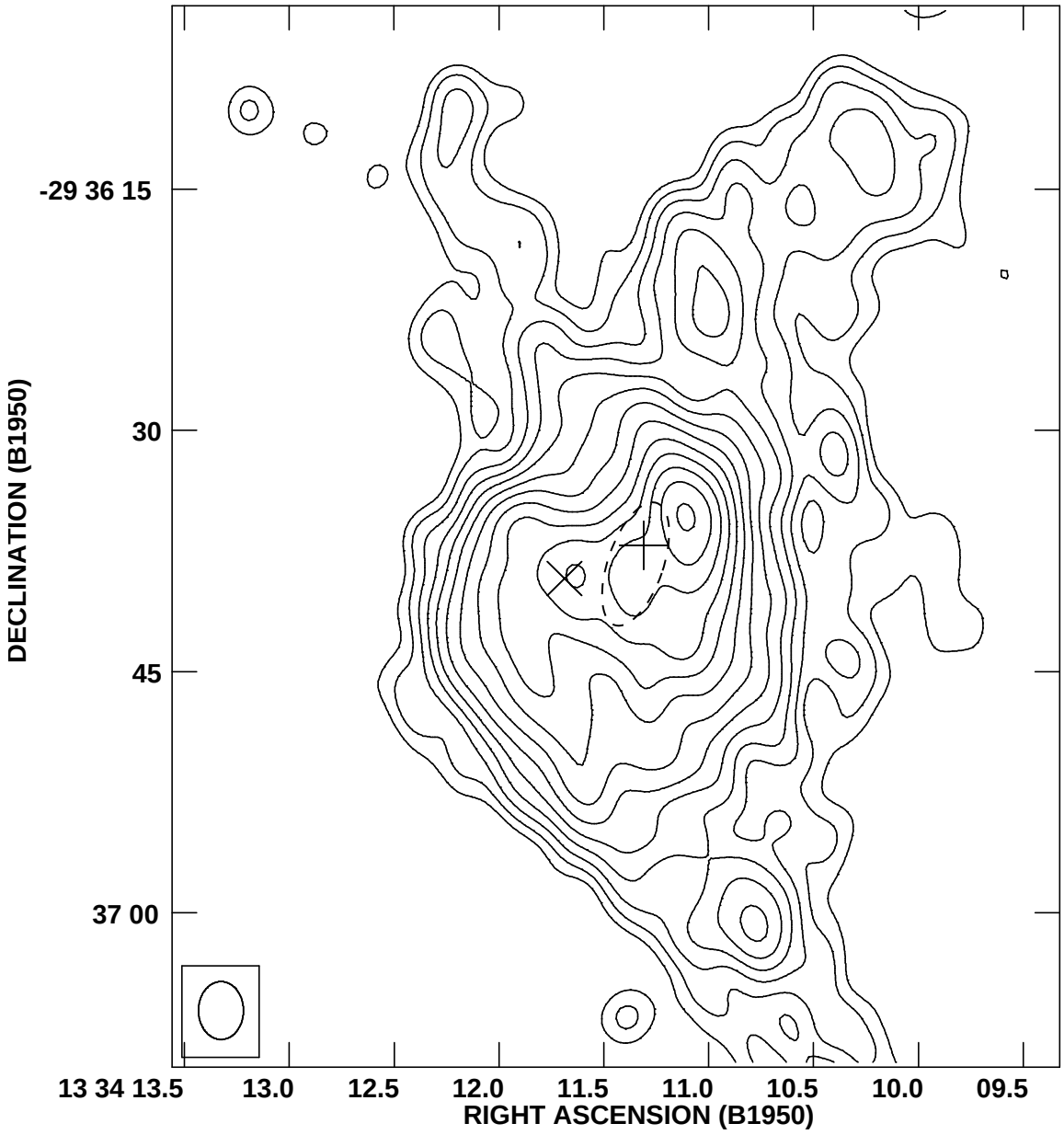



Figure 2.8 Contours of 20cm emission from the 1983 observation. Contour levels are same as Figure 2.6. The cross indicates the position of the optical nucleus. The plus sign indicates the reported position of the hidden nuclear mass as determined by Mast et al. (2005). The ellipse surrounding the plus indicates a probable region in which the hidden mass lies due to another estimate by Thatte et al. (2000).

# Chapter 3

# A Study of Compact Radio Sources in Nearby Face-on Spiral Galaxies. II. Multiwavelength Analyses of Sources in M51

## 3.1 Introduction

M51 (NGC 5194/5) is a nearby, grand-design spiral galaxy with an early-type companion forming an interacting pair. It is nearly face-on ($i \sim 20°$), which makes it an ideal candidate for population and morphology studies at all wavelengths. This is the second galaxy in our study of nearby spiral galaxies. Results of a long-term study of M83 were presented in Maddox et al. (2006).

The few distance determinations for M51 range from 6.0 Mpc (Baron et al., 1996) to 9.6 Mpc (Sandage & Tammann, 1974). We have opted to use the distance of 8.4 Mpc as derived by the planetary nebula luminosity function (PLNF) of the galaxy (Feldmeier et al., 1997)

Despite the interaction with M51b, the star-formation rate in the main galaxy is rather modest (Calzetti et al., 2005). The M51a/b interacting system has played host to three supernovae in modern times. M51a was the parent galaxy to SN 1994I (Puckett et al., 1994) and SN 2005cs (Kloehr et al., 2005), the latter of which will not be discussed further in this paper. M51b was host to SN 1945A (Kowal & Sargent, 1971). We will report briefly

on the radio emission of SN 1994I, the only supernova that we have detected in this galaxy with our radio observations.

An H I study of M51 by Rots et al. (1990) noted that the neutral gas emission follows the spiral arms closely. The large quantities of gas indicate that compact radio emission should also be concentrated along the arms.

M51 contains a low-luminosity Seyfert 2 nucleus that exhibits evidence of a bipolar outflow (e.g., Ford et al., 1985). The outflow has been studied in several wavebands.

In this paper we present multiwavelength analyses of the numerous compact radio sources in M51 from new, high-resolution observations using the Very Large Array. We present details of the radio observations and analysis. We compare our radio observations with archived optical, infrared (IR) and X-ray data to find counterparts in these complementary bands. Finally, we discuss the radio emission from the Seyfert 2 nucleus.

## 3.2 Observations and Data Reduction

Some of the observational parameters for this data are presented in Table 3.1. The 20 cm observation was performed on 2002 April 5 for a total of 6 hours while the array was in A configuration. The 6 cm observations were performed at B configuration over several days in December 2003 and January 2004. The total on-source integration time for the 6 cm observations was 22.5 hours.

All of the data were processed using the Astronomical Image Processing System (AIPS) provided by NRAO. Flux calibration was performed using 3C 286 as the primary source calibrator. To correct for atmospheric phase variations, a secondary calibrator, J1327+434 was used in all observations. The data were then imaged using the AIPS task IMAGR

using a Briggs robustness parameter of 0. This value has the advantage of minimizing noise while allowing for excellent point-source detection in resultant images. Due to the low flux in the radio sources and the depth of the observations, self-calibration was not required. The data sets were deconvolved using Gaussian restoring beams, the dimensions of which are indicated in Table 3.1. The deconvolved beams were determined using the values for the "dirty" beam, calculated from the Fourier transform of the $u$-$v$ plane coverage. After imaging, the task PBCOR was run on each map to correct for the shape of the primary beam.

## 3.3 Data Analysis

An initial source list was obtained using the AIPS task SAD, which searches for points in a radio map that are higher than a specified level. A Gaussian fit was applied to each detected emission source, and fits that fail are rejected by the algorithm. Some extended and slightly extended sources were listed as multiple points. Similarly, SAD listed point-like emission in the extended nuclear "bubble" to the north of the nucleus. Our source list was compressed to account for this and the "bubble" sources were removed from the list. Finally a visual inspection of the maps was performed in order to find real emission that was rejected by the detection algorithm. The final list of sources, including peak flux densities and spectral indices ($S \propto \nu^{+\alpha}$) are listed in Table 3.2. The final 20 cm radio map is shown in Figure 3.1. The spiral arms are evident in the radio maps, as is the position of M51b, the interaction companion galaxy. As a comparison, Figure 3.2 shows a three-color Hubble Space Telescope (HST) image of M51.

The peak flux density values were determined using the AIPS task IMFIT. The input

model was a simple two-dimensional Gaussian. Peak flux densities are listed in Table 3.2. Where the fit failed, we assume a 3 $\sigma$ upper limit of 65 $\mu$Jy at 20 cm and 36 $\mu$Jy at 6 cm.

## 3.4 Discussion

### 3.4.1 Radio Point Sources

In Table 3.2, we present the results of our radio survey of the M51 system listing the positions, radio flux densities at 20 cm and 6 cm (when detected at the appropriate band), and the spectral index ($\alpha$, $S_\nu \propto \nu^{+\alpha}$) derived from these measurements for the 107 radio point sources we have detected. We have determined that 33 of these sources have steep indices ($\alpha < -0.3$), 45 sources have flat indices ($-0.3 < \alpha < 0.3$), 3 sources have inverted spectral indices ($0.3 < \alpha$), and 26 sources cannot be distinguished as having either a flat or steep spectral index due to the experimental uncertainties. Figure 3.3 shows the sources overlayed on an HST/ACS I Band image of M51.

Sources 15, 20, 35, 40, and 78 have very steep spectral indices ($\alpha < -1$), with sources 40 and 78 having only been detected in the 20 cm observations. These sources may be background sources (e.g., unresolved radio galaxies), optically obscured SNRs, or highly variable, unresolved radio sources in M51, as the 20 cm and 6 cm data were obtained 21 months apart. Source 20 is associated with an optical H II region, so it is likely this source is an optically obscured SNR.

All of the detected radio sources lie along the spiral arms of the galaxy. The three inverted sources, denoted as blue circles in Figure 3.3 lie in dust lanes in the inner region of the galaxy. They could be embedded H II regions experiencing free-free absorption due

to a high column density of gas. In order to test for free-free absorption in these compact sources, we would require high resolution radio observations at lower and higher frequencies to look for a spectral turnover at low frequency. A similar study was performed by Tingay (2004) for NGC 253, who found significant evidence for free-free absorption of the compact radio emission regions.

The flat sources in Figure 3.3, indicated in yellow, tend to populate the outer spiral arms, away from dust-rich areas. The steep sources are seen mostly along the inner arms. If these sources are radio SNRs, the position along the inner region is not unusual, as star formation in this region would be higher. The indeterminant sources also lie mostly in the inner region. Some of these sources might be absorbed SNRs, as they are positioned along the dust lanes. High resolution, narrow-band optical observations (e.g., [O III] and [S II]) would be needed to further classify these objects.

We have identified 44 radio sources coincident with previously detected optical H II regions. Of these, 27 sources have flat spectral indices, 8 have steep spectral indices and 8 have indices which cannot be classified as either due to experimental uncertainty. One of the 45 sources, source 13, has an inverted spectral index >1.0. This source is likely embedded in the disk and the 20 cm flux is being absorbed by intervening gas (e.g., Tingay, 2004). Sources 17 and 34 with spectral indices $\sim 0.5$ are also likely embedded H II regions.

**Supernovae**

At the time of our observations, M51 had been the host to two historical supernovae: the Type I SN 1945A (Kowal & Sargent, 1971), and the Type Ic SN1994I (Puckett et al., 1994). We were unable to detect emission from the reported position of SN 1945A, which exploded

in M51b and would be near the edge of our field of view. Figure 3.4 shows the position of the supernovae on an optical DSS image of M51.

We have detected non-thermal radio emission from the reported optical position of SN 1994I (Source 58, Puckett et al., 1994), nearly a decade after its initial discovery (see Figure 3.5). The flux level at this time (160 $\mu$Jy at 20 cm) is consistent with a Type Ic supernova, based on the model of Weiler et al. (2002). If we assume a uniform, progenitor wind velocity of 10 km s$^{-1}$, we determine a progenitor mass-loss rate of $\dot{M} = 2.75 \times 10^{-6}\ M_{\odot}\ yr^{-1}$ (Stockdale et al., 2005b). An estimate of the progenitor mass-loss based on the X-ray emission (using the same wind velocity) yields a rate of $\dot{M} \sim 10^{-5}\ M_{\odot}\ yr^{-1}$ (Immler et al., 2002).

While our observations pre-date the explosion of the type II SN 2005cs, subsequent radio observations of this SN did not detect emission from this source at 1.3, 2.0, 3.5, and 6.2 cm (Stockdale et al., 2005a). We detect no identifiable radio emission from the immediate nearby region, which would indicate the presence of radio SNRs or HII regions.

**Optical Counterparts**

We overlayed our radio positions on an optical HST/ACS image available through the Hubble Heritage project (Figure 3.3). Of our 116 compact radio sources, 42 are coincident with large H II regions. An additional 24 have more compact H$\alpha$ counterparts. Six sources (5, 47, 68, 74, 76, and 84) are coincident with resolved H$\alpha$ shells (Figure 3.6). Other broad optical bands show only emission from stars. Two of the sources, 47 and 84, have associated X-ray emission, and will be discussed in Section 3.4.1. The remaining sources, with the exception of Source 5 exhibit non-thermal radio emission consistent with that of

SNRs. The angular diameter of most remnants are $\sim 0.3 - 0.5''$. If we assume a Cas A like expansion velocity of 6000 km s$^{-1}$, this would give an age of $\sim 2000 - 3300$ yr for the largest shell source.

The remaining H II counterparts lie in large clouds of ionized gas. In other optical filters, these clouds contain a large star cluster (Figure 3.7). Most of these radio sources have flat spectral emission, but a few exhibit non-thermal spectra consistent with the emission from the shell sources. Four of the sources in this category have X-ray counterparts, and will be discussed in Section 3.4.1.

To get an idea of the strength of the H II regions in M51, we have computed excitation parameters based on the 6 cm radio properties that we have determined from our observations. Using the formulae from Schraml & Mezger (1969) and Mezger & Henderson (1967):

$$U = 4.5526 \left[ a(\nu, T)^{-1} \nu^{0.1} T^{0.35} S_\nu D^2 \right]^{1/3}, \tag{3.1}$$

where

$$a(\nu, T) = 0.366 \left( \frac{\nu}{\mathrm{GHz}} \right)^{0.1} \left( \frac{T_e}{\mathrm{K}} \right)^{-0.15} \left\{ \ln \left[ 4.995 \times 10^{-2} \left( \frac{\nu}{\mathrm{GHz}} \right)^{-1} \right] + 1.5 \ln \left( \frac{T_e}{\mathrm{K}} \right) \right\} \tag{3.2}$$

We assume and average H II temperature of $T_e = 10^4$ K. The results of these calculations are listed in Table 3.3.

Just as we found in M83 (Maddox et al., 2006), we are selectively detecting the brightest H II regions in our observations. Eleven of the sources exhibit steep spectral indices ($\alpha < -0.3$), indicating a non-thermal emission mechanism. Five of the source are confirmed SNRs (see Section 3.4.1), and the remaining are possible SNR candidates. High resolution [O III] and [S II] observations are needed to possibly confirm the classification of these sources as

SNRs.

### IR/UV Emission

Calzetti et al. (2005) presented a study of the star formation activity in M51 using data from *GALEX* and *Spitzer*. We compared our radio results with those presented in that study. The aperture photometry in the IR/UV study was performed using 13" apertures, so in many cases there are several radio sources contained in one aperture, particularly in the innermost region of M51a. A more detailed study of individual IR sources from a *Spitzer* observation will be presented in a future paper (Maddox et al, in preparation). The apertures which contain radio sources are listed in Table 3.4. The aperture designations are taken from Table 1 of Calzetti et al. (2005), as are the luminosity values. The star formation study assumed a distance of 8.3 Mpc. The difference in luminosity values for that distance versus the 8.4 Mpc used here is 0.02 dex.

Most of the UV emission in the inner region of the galaxy, where we have the greatest concentration of radio sources, are due to dust-containing stellar clusters. All of the apertures contain some IR emission, but they are concentrated most in the inner spiral arms, where it is expected that star formation would be higher and therefore more heating of the dust.

### X-ray Counterparts

Many radio sources are also coincident with bright X-ray sources in external galaxies. Though most of the luminous X-ray sources detected in galaxies are X-ray binaries, few are detectable in the radio, assuming isotropic emission. It may, however, be possible to de-

tect beamed emission, e.g., from a microquasar. The presence of such an X-ray counterpart can aid in the classification of these sources.

Of the 107 radio sources detected in M51, 13 have X-ray counterparts from Chandra observations (Kilgard et al., 2005). The Chandra observations reach a uniform limiting luminosity of less than $5 \times 10^{36} erg\ s^{-1}$. Basic properties of these 13 sources are listed in Table 3.5. As described in Prestwich et al. (2003) and Kilgard et al. (2005), it is possible to assign a rough source classification to an X-ray source based upon its X-ray luminosity, variability, and placement on an X-ray color-color diagram. Figure 3.8 shows a model X-ray color-color diagram. SNRs, which typically have thermal X-ray spectra with temperatures of a few hundred eV, are located in the lower-left portion of the color-color diagram. As the spectrum becomes more absorbed, it moves up the diagram. The right half of the diagram is occupied by sources with power-law or multi-component spectra. Thus, all SNRs should be found on the left side of the diagram, regardless of the absorbing column.

Figure 3.9 shows the X-ray color-color diagram for the radio sources with X-ray counterparts. As can clearly be seen, most of the sources are indicative of thermal spectra with increasing absorption. Indeed, 8 of the 13 sources are near textbook examples of SNR-like X-ray spectra. These sources are numbers 47, 49, 53, 58, 68, 73, 79, and 84.

Of the 8 sources with SNR-like X-ray colors, 6 are coincident with H$\alpha$ shells or discrete H$\alpha$ point sources in observations with the Advanced Camera for Surveys (ACS) on HST (optical/X-ray coincidences are discussed in Kilgard et al. (2006)). The remaining 2, sources 73 and 79, are associated with massive star clusters with embedded H$\alpha$ emission, thus determining the position of any individual SNRs in the H$\alpha$ is not feasible. These sources are located along the spiral arms of the galaxy.

Notes on individual sources:

Source 4 lies outside the main disc of the galaxy. Its X-ray colors are consistent with an XRB-like spectrum, though a soft AGN spectrum cannot be ruled out. The source is coincident with a blue point source in the optical ACS images.

Source 12 has a highly absorbed X-ray spectrum, with no photons detected below 2 keV in any of the Chandra observations. (It is located at the far right of the color-color diagram). It also exhibits variability on the timescale of months to years between Chandra observations. The source is coincident with a very faint red point source in the optical images from ACS. The steep radio spectrum points to a highly non-thermal emission mechanism. All these things combined lead to the conclusion that the source is likely a background AGN whose soft X-ray emission is absorbed by M51.

Source 58, along the inner spiral arm, is in a confused H$\alpha$ emission region, though we have already determined it to be emission from SN 1994I.

Source 65 is coincident with a compact H$\alpha$ source, but exhibits XRB-like X-ray colors.

Source 95 is highly absorbed in the X-rays. (It is located in the "Absorbed sources" ellipse of the color-color diagram). It is thus impossible to select between possible soft X-ray spectra. However, the position towards the left on the color-color diagram means that we can rule out hard X-ray spectra. The source is thus consistent with either a SNR-like or soft XRB-like spectrum. There is no counterpart detected in B, V, I or H$\alpha$.

Source 107 is the brightest of the X-ray/radio overlaps. It exhibits a flat radio spectrum between 20cm and 6cm. This would normally indicate a thermal process that would also produce H$\alpha$ emission; however, no H$\alpha$ emission is detected in the ACS images. The radio observations were separated by $\sim$ 20 months. It is possible that we are observing a

microquasar in a radio-loud state (Nipoti et al., 2005).

### 3.4.2 Nuclear Emission

The X-ray and radio morphologies of the nuclear region are strikingly similar. They consist of an area of ring-like emission to the north, postulated to be a bubble blown out due to an outflow (Ford et al., 1985), and a dense area of emission to the south of the nucleus. Following the studies by Terashima & Wilson (2001) (and references therein), we refer to the southern source as the extranuclear cloud (XNC). The nucleus itself is unresolved. Figure 3.10 shows radio contours overlayed onto a three color X-ray image of this nuclear region.

X-ray spectral modeling of the nucleus determined that the emission consisted of two major components. The hard component arises from reflection of the radiation from a compact nuclear source with a power law spectrum by cold matter in the vicinity. The soft component is similar to the XNC, being well modeled by a thermal plasma that is shock-heated by mass outflow (Terashima & Wilson, 2001). In the radio, shock heating due to an observed radio jet (Crane & van der Hulst, 1992) would produce non-thermal continuum emission. For the nucleus (Source 52), we measure a steep spectral index ($-0.82 \pm 0.27$) which strengthens the evidence for shock-heating in the nucleus.

We measure a similar steep spectrum for the XNC ($\alpha = -0.81 \pm 0.02$). In high resolution 6 cm observations of the nucleus, Crane & van der Hulst (1992) described a radio jet emanating from the nucleus and terminating in the XNC. This jet, hypothesized in earlier studies (e.g., Ford et al., 1985), seems to drive the heating of the cloud. It is the site of the hardest X-ray emission in the XNC (Terashima & Wilson, 2001) and the broadest optical line emission (Cecil, 1988).

Comparison of the bubble in the two radio bands yield a non-thermal spectral index measurement ($\alpha = -0.58$), which is consistent with a synchrotron emission mechanism. This matches the X-ray analysis of the bubble in Terashima & Wilson (2001). The knots of X-ray emission (not seen in the our radio observations due to resolution limits) may be SNRs. These sources are not heavily absorbed, so they could be clumps of hot gas on the edge of the bubble. They could also be soft X-ray binaries that are not embedded in the diffuse emitting gas.

In a high resolution observation of the nuclear region of M51 at 6 cm, Crane & van der Hulst (1992) detected evidence for a radio jet emanating from the nucleus and fueling the expansion of the XNC. Gopal-Krishna & Irwin (2000) presented a model where shells in spiral galaxies, like those seen in our data, may be produced through shock heating due to a radio jet. The interaction of the jet with the material within the disk would lead to a bow shock, which is seen in the XNC by Crane & van der Hulst (1992). If the bubble were driven by a continuous jet, like the XNC, we would expect that there would be jet emission visible in our observations, or in higher resolution observations. Crane & van der Hulst (1992) saw no evidence for jet emission in their 6 cm observations, nor do we see evidence. The ring-like structure of the bubble indicates cooler gas within. Rudnick (1982) suggested a one-sided ejection mechanism to explain the asymmetrical nature of some double lobed radio sources. If this is the case, the bubble could be a relic of a previous one-sided ejection cycle.

## 3.5 Conclusions

We have presented a multiwavelength study of the compact radio sources in M51. Primarily using radio, optical and X-ray observations, we have classified most of the detected radio sources. Our primary findings are:

• We detected emission from the Type Ic SN 1994I nearly a decade after explosion. We found the emission at this epoch to be consistent with light curve models for Type Ib/Ic supernovae. The SN was also detected in X-ray, though no optical counterpart was seen.

• Six of the radio sources associated with H$\alpha$ sources are young SNRs with resolved shells. Most exhibit steep continuum radio spectra consistent with synchrotron emission. Based on a Cas A expansion velocity, we estimate the age of the SNRs to be $\sim 2000 - 3300$ yr.

• Thirteen radio sources have X-ray counterparts. Eight of the 13 sources have SNR-like X-ray spectra. Two of these X-ray/radio sources are coincident with resolved H$\alpha$ shells. Two of the remaining sources are highly absorbed. Source 12 is likely a background AGN, while Source 95, though there is no optical counterpart, could be a dust-embedded SNR or an XRB.

• The result of our analysis of the nuclear region, including the XNC, bubble and nucleus, are consistent with previous studies that suggest a bipolar radio jet from the low luminosity Seyfert 2 nucleus. The nucleus and XNC have identical continuum spectra, indicative of shock heated gas interacting with the jet.

Table 3.1. M51 Observations

| Observing Band (GHz) | Configuration | Date | Integration Time (min) | Clean Beam (arcsec$^2$) | rms Noise ($\mu$Jy beam$^{-1}$) |
|---|---|---|---|---|---|
| 1.425 | A | 2002 Apr 5 | 359.0 | $1.50 \times 1.21$ | 22.5 |
| | | ..... | | | |
| | | 2003 Dec 11 | 426.5 | | |
| | | 2003 Dec 12 | 212.5 | | |
| | | 2003 Dec 20 | 90.2 | | |
| | | 2003 Dec 28 | 119.0 | | |
| 4.860 | B | 2003 Dec 29 | 91.5 | $1.47 \times 1.13$ | 11.7 |
| | | 2004 Jan 2 | 120.3 | | |
| | | 2004 Jan 5 | 120.3 | | |
| | | 2004 Jan 9 | 170.5 | | |

Table 3.2. Positions, Flux Densities and Spectral Indices of Point Sources in M51

| Source | R.A. (J2000) (h m s) | Dec (J2000) (d m s) | 20cm ($\mu$Jy beam$^{-1}$) | 6cm ($\mu$Jy beam$^{-1}$) | Spectral Index $\alpha$[a] |
|---|---|---|---|---|---|
| 1 | 13 29 30.46 | 47 12 50.61 | 394±21 | 190±18 | −0.59±0.11 |
| 2 | 13 29 36.56 | 47 11 05.51 | 68±21 | 43±13 | −0.37±0.43 |
| 3 | 13 29 38.05 | 47 12 05.84 | 470±22 | 264±14 | −0.47±0.07 |
| 4 | 13 29 38.96 | 47 13 23.60 | 84±22 | 102±18 | +0.15±0.32 |
| 5[b] | 13 29 39.36 | 47 08 40.72 | ··· | 73±17 | > +0.09 |
| 6[b] | 13 29 43.67 | 47 10 00.95 | 56±21 | 32±13 | −0.46±0.55 |
| 7[b] | 13 29 44.05 | 47 10 22.71 | 245±20 | 259±12 | +0.05±0.09 |
| 8 | 13 29 45.10 | 47 13 32.25 | 164±21 | 93±13 | −0.46±0.19 |
| 9[b] | 13 29 45.17 | 47 09 56.93 | 192±21 | 229±12 | +0.14±0.12 |
| 10[b] | 13 29 46.40 | 47 12 33.14 | 55±22 | 75±12 | +0.25±0.43 |
| 11[b] | 13 29 46.74 | 47 09 40.78 | ··· | 61±13 | > −0.06 |
| 12 | 13 29 49.14 | 47 12 57.11 | 123±21 | 43±15 | −0.86±0.27 |
| 13[b] | 13 29 49.43 | 47 12 40.54 | ··· | 217±11 | > +0.98 |
| 14 | 13 29 49.53 | 47 14 00.17 | 234±21 | 221±13 | −0.05±0.11 |
| 15 | 13 29 49.60 | 47 13 27.51 | 326±21 | 74±12 | −1.21±0.17 |
| 16 | 13 29 49.43 | 47 11 23.86 | 123±20 | 49±17 | −0.75±0.38 |

Table 3.2 (cont'd)

| Source | R.A. (J2000) (h m s) | Dec (J2000) (d m s) | 20cm ($\mu$Jy beam$^{-1}$) | 6cm ($\mu$Jy beam$^{-1}$) | Spectral Index $\alpha$[a] |
|---|---|---|---|---|---|
| 17 | 13 29 49.93 | 47 11 20.53 | 121±19 | 232±11 | +0.53±0.16 |
| 18 | 13 29 49.93 | 47 11 31.11 | 464±22 | 235±11 | −0.55±0.07 |
| 19[b] | 13 29 49.95 | 47 11 26.73 | 234±21 | 113±10 | −0.59±0.13 |
| 20[b] | 13 29 50.04 | 47 11 24.89 | 205±21 | 43±17 | −1.20±0.41 |
| 21 | 13 29 50.13 | 47 11 40.32 | 140±20 | 54±10 | −0.78±0.23 |
| 22[b] | 13 29 50.13 | 47 11 36.92 | 107±20 | 59±10 | −0.49±0.25 |
| 23 | 13 29 50.20 | 47 11 51.36 | 146±20 | 103±11 | −0.28±0.17 |
| 24[b] | 13 29 50.24 | 47 11 19.06 | 71±21 | 63±11 | −0.10±0.34 |
| 25 | 13 29 50.26 | 47 11 48.48 | ··· | 54±10 | $> -0.16$ |
| 26 | 13 29 50.30 | 47 11 22.42 | 432±21 | 240±11 | −0.48±0.07 |
| 27 | 13 29 50.32 | 47 13 57.95 | 61±20 | 63±13 | +0.026±0.87 |
| 28 | 13 29 50.32 | 47 11 32.91 | 111±17 | 63±8 | −0.46±0.20 |
| 29 | 13 29 50.43 | 47 11 53.26 | ··· | 70±10 | $> 0.06$ |
| 30 | 13 29 50.45 | 47 11 45.16 | 56±20 | 55±11 | −0.01±0.41 |
| 31 | 13 29 50.45 | 47 11 27.02 | 115±20 | 73±10 | −0.37±0.22 |
| 32 | 13 29 50.46 | 47 11 37.36 | ··· | 59±9 | $> -0.08$ |

Table 3.2 (cont'd)

| Source | R.A. (J2000) (h m s) | Dec (J2000) (d m s) | 20cm ($\mu$Jy beam$^{-1}$) | 6cm ($\mu$Jy beam$^{-1}$) | Spectral Index $\alpha$[a] |
|---|---|---|---|---|---|
| 33[b] | 13 29 50.48 | 47 13 45.22 | 82±21 | 73±12 | −0.09±0.3 |
| 34 | 13 29 50.70 | 47 11 55.86 | ··· | 122±10 | > +0.51 |
| 35 | 13 29 50.95 | 47 13 43.69 | ··· | 84±12 | > +0.20 |
| 36 | 13 29 51.50 | 47 12 00.54 | 213±21 | 165±11 | −0.21±0.12 |
| 37 | 13 29 51.57 | 47 12 08.01 | 2229±21 | 946±11 | −0.70±0.015 |
| 38 | 13 29 51.68 | 47 11 57.89 | 52±20 | 49±10 | −0.05±0.44 |
| 39 | 13 29 51.73 | 47 12 01.87 | 108±21 | 132±11 | +0.16±0.21 |
| 40 | 13 29 51.80 | 47 11 40.43 | 385±20 | ··· | < −1.99 |
| 41 | 13 29 51.86 | 47 11 37.01 | 211±20 | 115±10 | −0.49±0.13 |
| 42[b] | 13 29 51.99 | 47 10 54.02 | 115±20 | 52±11 | −0.65±0.27 |
| 43 | 13 29 52.01 | 47 12 02.21 | ··· | 55±10 | > −0.14 |
| 44[b] | 13 29 52.01 | 47 12 42.95 | 151±21 | 173±11 | +0.11±0.15 |
| 45 | 13 29 52.02 | 47 12 04.42 | ··· | 57±10 | > −0.11 |
| 46[b] | 13 29 52.03 | 47 12 47.20 | 64±20 | 62±11 | −0.03±0.36 |
| 47[b] | 13 29 52.08 | 47 11 26.82 | 84±21 | 40±13 | −0.60±0.41 |
| 48 | 13 29 52.17 | 47 11 36.60 | 94±20 | 73±10 | −0.21±0.25 |

Table 3.2 (cont'd)

| Source | R.A. (J2000) (h m s) | Dec (J2000) (d m s) | 20cm ($\mu$Jy beam$^{-1}$) | 6cm ($\mu$Jy beam$^{-1}$) | Spectral Index $\alpha$[a] |
|---|---|---|---|---|---|
| 49[b] | 13 29 52.22 | 47 11 29.48 | 87±29 | 50±13 | −0.45±0.42 |
| 50 | 13 29 52.35 | 47 11 36.09 | 94±20 | 59±10 | −0.38±0.27 |
| 51[b] | 13 29 52.38 | 47 12 38.51 | ··· | 56±11 | $> -0.13$ |
| 52[b] | 13 29 52.73 | 47 11 21.23 | 162±26 | 59±13 | −0.82±0.27 |
| 53 | 13 29 52.71 | 47 11 42.73 | 2079±21 | 1135±11 | −0.49±0.01 |
| 54 | 13 29 52.79 | 47 11 39.17 | 2047±20 | 761±10 | −0.81±0.02 |
| 55[b] | 13 29 53.22 | 47 12 39.53 | 94±21 | 65±11 | −0.30±0.28 |
| 56 | 13 29 53.86 | 47 09 54.09 | 152±22 | 73±12 | −0.60±0.22 |
| 57[b] | 13 29 53.91 | 47 14 05.44 | ··· | 61±13 | $> -0.06$ |
| 58 | 13 29 54.12 | 47 11 30.33 | 160±22 | 46±11 | −1.02±0.28 |
| 59 | 13 29 54.24 | 47 11 32.40 | 136±22 | 55±11 | −0.74±0.26 |
| 60 | 13 29 54.24 | 47 11 23.23 | 81±21 | 45±11 | −0.48±0.36 |
| 61 | 13 29 54.32 | 47 11 29.86 | 92±21 | 67±11 | −0.26±0.28 |
| 62 | 13 29 54.72 | 47 12 36.60 | 98±22 | 49±11 | −0.56±0.32 |
| 63 | 13 29 54.84 | 47 11 59.23 | 51±19 | 36±10 | −0.28±0.46 |
| 64[b] | 13 29 54.92 | 47 11 33.00 | 133±20 | 72±10 | −0.50±0.20 |

Table 3.2 (cont'd)

| Source | R.A. (J2000) (h m s) | Dec (J2000) (d m s) | 20cm ($\mu$Jy beam$^{-1}$) | 6cm ($\mu$Jy beam$^{-1}$) | Spectral Index $\alpha$[a] |
|---|---|---|---|---|---|
| 65 | 13 29 54.95 | 47 09 22.41 | 406±21 | 280±17 | −0.30±0.08 |
| 66[b] | 13 29 54.98 | 47 10 48.93 | 60±21 | 62±11 | +0.03±0.39 |
| 67[b] | 13 29 55.08 | 47 11 35.01 | 126±20 | 89±10 | −0.28±0.19 |
| 68[b] | 13 29 55.25 | 47 10 46.16 | 158±23 | 61±14 | −0.78±0.27 |
| 69 | 13 29 55.31 | 47 11 38.61 | 133±20 | 54±10 | −0.73±0.24 |
| 70 | 13 29 55.33 | 47 11 36.51 | ··· | 59±10 | $> -0.08$ |
| 71 | 13 29 55.33 | 47 12 02.32 | ··· | 44±10 | $> -0.32$ |
| 72 | 13 29 55.42 | 47 11 40.67 | ··· | 51±10 | $> -0.20$ |
| 73[b] | 13 29 55.42 | 47 14 02.05 | 101±23 | 80±16 | −0.19±0.30 |
| 74 | 13 29 55.52 | 47 12 09.92 | 98±20 | 54±10 | −0.49±0.28 |
| 75 | 13 29 55.57 | 47 13 59.82 | 175±15 | 78±12 | −0.66±0.18 |
| 76 | 13 29 55.60 | 47 12 03.08 | 80±20 | 37±10 | −0.63±0.37 |
| 77 | 13 29 55.64 | 47 11 41.57 | ··· | 53±10 | $> -0.17$ |
| 78 | 13 29 55.69 | 47 11 46.61 | 122±18 | ··· | $< -1.04$ |
| 79[b] | 13 29 55.86 | 47 11 44.48 | 319±25 | 230±13 | −0.26±0.10 |
| 80 | 13 29 55.85 | 47 11 54.58 | 246±22 | 142±11 | −0.45±0.12 |

Table 3.2 (cont'd)

| Source | R.A. (J2000) (h m s) | Dec (J2000) (d m s) | 20cm ($\mu$Jy beam$^{-1}$) | 6cm ($\mu$Jy beam$^{-1}$) | Spectral Index $\alpha$[a] |
|---|---|---|---|---|---|
| 81 | 13 29 55.86 | 47 11 50.61 | 147±21 | 61±11 | −0.72±0.23 |
| 82[b] | 13 29 56.13 | 47 14 08.91 | 77±22 | 78±14 | +0.01±0.34 |
| 83 | 13 29 56.21 | 47 10 47.33 | 109±21 | 73±11 | −0.33±0.24 |
| 84 | 13 29 57.47 | 47 10 37.08 | 128±22 | 59±14 | −0.63±0.29 |
| 85[b] | 13 29 58.94 | 47 14 09.00 | 98±22 | 89±13 | −0.08±0.27 |
| 86 | 13 29 59.49 | 47 11 09.96 | ··· | 68±11 | > +0.03 |
| 87[b] | 13 29 59.53 | 47 15 58.30 | 1494±20 | 1181±21 | −0.19±0.02 |
| 88 | 13 29 59.58 | 47 11 11.32 | 95±20 | 77±11 | −0.17±0.25 |
| 89[b] | 13 29 59.61 | 47 13 59.18 | 88±20 | 84±13 | −0.04±0.27 |
| 90 | 13 29 59.84 | 47 11 12.68 | 238±21 | 307±12 | +0.21±0.10 |
| 91[b] | 13 30 00.11 | 47 13 30.53 | 63±21 | 66±13 | +0.04±0.39 |
| 92[b] | 13 30 00.36 | 47 13 18.87 | 82±21 | 76±13 | −0.06±0.31 |
| 93[b] | 13 30 00.78 | 47 11 37.73 | ··· | 58±11 | > −0.10 |
| 94[b] | 13 30 00.93 | 47 09 28.90 | 61±18 | 73±13 | +0.15±0.34 |
| 95 | 13 30 01.27 | 47 12 43.77 | 131±22 | 62±15 | −0.61±0.29 |
| 96 | 13 30 01.41 | 47 11 57.83 | 78±20 | 50±11 | −0.36±0.34 |

Table 3.2 (cont'd)

| Source | R.A. (J2000) (h m s) | Dec (J2000) (d m s) | 20cm ($\mu$Jy beam$^{-1}$) | 6cm ($\mu$Jy beam$^{-1}$) | Spectral Index $\alpha$[a] |
|---|---|---|---|---|---|
| 97[b] | 13 30 01.50 | 47 12 51.42 | 412±21 | 443±12 | +0.06±0.06 |
| 98[b] | 13 30 01.77 | 47 11 48.81 | 54±22 | 60±12 | +0.09±0.45 |
| 99 | 13 30 02.03 | 47 09 51.35 | 113±21 | 75±13 | −0.33±0.25 |
| 100[b] | 13 30 02.38 | 47 09 49.10 | 170±21 | 194±13 | +0.11±0.14 |
| 101[b] | 13 30 02.75 | 47 09 56.94 | 67±21 | 64±13 | −0.04±0.37 |
| 102[b] | 13 30 03.50 | 47 09 41.00 | ··· | 78±14 | $> +0.14$ |
| 103[b] | 13 30 03.95 | 47 15 33.00 | 119±21 | 144±21 | +0.16±0.23 |
| 104 | 13 30 05.13 | 47 10 35.78 | 9599±22 | 4287±14 | −0.66±0.00 |
| 105[b] | 13 30 07.38 | 47 13 22.30 | 144±21 | 175±15 | +0.16±0.17 |
| 106 | 13 30 10.85 | 47 09 40.26 | 148±21 | 100±17 | −0.32±0.22 |
| 107 | 13 30 11.03 | 47 10 40.75 | 500±22 | 482±20 | −0.03±0.06 |

[a] $S_\nu \propto \nu^{+\alpha}$

[b] Coincident with optical H II region

Table 3.3. Excitation Parameters for H$\alpha$ Sources

| Source | Spectral Index | U (pc cm$^{-2}$) |
|---|---|---|
| 5 | $> +0.09$ | 242.5 |
| 6 | –0.46±0.55 | 184.2 |
| 7 | 0.05±0.09 | 369.9 |
| 9 | 0.14±0.12 | 355.0 |
| 10 | 0.25±0.43 | 244.7 |
| 11 | $> -0.06$ | 228.4 |
| 13 | $> +0.98$ | 348.7 |
| 19 | –0.59±0.13 | 280.5 |
| 22 | –0.49±0.25 | 225.9 |
| 24 | –0.1±0.34 | 230.9 |
| 33 | –0.09±0.3 | 242.5 |
| 42 | –0.65±0.27 | 216.6 |
| 44 | 0.11±0.15 | 323.3 |
| 46 | –0.03±0.36 | 229.7 |
| 47 | –0.6±0.41 | 198.5 |
| 49 | –0.45±0.42 | 213.8 |
| 51 | $> -0.13$ | 222.0 |

Table 3.3 (cont'd)

| Source | Spectral Index | U (pc cm$^{-2}$) |
|---|---|---|
| 52 | –0.82±0.27 | 225.9 |
| 55 | –0.3±0.28 | 233.3 |
| 57 | $> -0.06$ | 228.4 |
| 64 | –0.5±0.2 | 241.4 |
| 66 | 0.03±0.39 | 229.7 |
| 67 | –0.28±0.19 | 259.1 |
| 68 | –0.78±0.27 | 228.4 |
| 73 | –0.19±0.3 | 250.0 |
| 79 | –0.26±0.1 | 355.5 |
| 82 | 0.01±0.34 | 247.9 |
| 85 | –0.08±0.27 | 259.1 |
| 87 | –0.19±0.02 | 613.2 |
| 89 | –0.04±0.27 | 254.1 |
| 91 | 0.04±0.39 | 234.5 |
| 92 | –0.06±0.31 | 245.8 |
| 93 | $> -0.10$ | 224.6 |
| 94 | 0.15±0.34 | 242.5 |

Table 3.3 (cont'd)

| Source | Spectral Index | U (pc cm$^{-2}$) |
|---|---|---|
| 97 | 0.06±0.06 | 442.3 |
| 98 | 0.09±0.45 | 227.2 |
| 100 | 0.11±0.14 | 335.9 |
| 101 | –0.04±0.37 | 232.1 |
| 102 | $> +0.14$ | 247.9 |
| 103 | 0.16±0.23 | 304.1 |
| 105 | 0.16±0.17 | 324.6 |

Table 3.4. Properties of Coincident IR/UV/Radio Emission

| IR Source | Radio Source(s) | $\log L$(FUV) | $\log L$(NUV) | $\log L$(H$\alpha$) | $\log L(8)$ | $\log L(24)$ |
|---|---|---|---|---|---|---|
| IR-03 | 40,41 | 41.07 | 41.22 | 38.86 | 41.36 | 41.17 |
| IR-04 | 47,49,50 | 41.00 | 41.19 | 38.96 | 41.34 | 41.14 |
| IR-05 | 58,59,61 | 40.74 | 41.03 | 38.88 | 41.40 | 41.14 |
| IR-08 | 64,67,69,70, 77,78,80,81 | 41.20 | 41.33 | 39.15 | 41.43 | 41.39 |
| IR-09 | 79 | 40.95 | 41.09 | 38.83 | 41.16 | 40.89 |
| IR-10 | 63 | 40.60 | 40.94 | 39.03 | 41.29 | 41.07 |
| IR-13 | 29,34,36,37, 38,39,43,45 | 40.95 | 41.17 | 39.20 | 41.54 | 41.38 |
| IR-15 | 21,23,25,30 | 40.72 | 40.91 | 38.81 | 41.35 | 41.14 |
| IR-16 | 18,19,22,28, 31,32 | 40.17 | 40.38 | 38.82 | 41.40 | 41.23 |
| IR-17 | 16,17,20,24, 26 | 40.10 | 40.32 | 38.88 | 41.17 | 41.00 |
| IR-30/08-03 | 86,88,90 | 40.75 | 40.76 | 38.87 | 41.17 | 41.02 |
| IR-35 | 62 | 40.25 | 40.40 | 38.76 | 41.08 | 40.80 |
| IR-36 | 55 | 40.26 | 40.41 | 39.01 | 41.08 | 40.95 |
| IR-37 | 44,46,51 | 40.69 | 40.84 | 39.24 | 41.22 | 41.24 |
| IR-39 | 13 | 39.85 | 39.83 | 38.98 | 41.15 | 41.17 |
| IR-54 | 53 | 40.24 | 40.58 | 38.51 | 41.04 | 40.78 |
| 01-04 | 27 | 40.00 | 40.00 | 38.70 | 40.72 | 40.38 |
| 01-05 | 15 | 39.91 | 39.95 | 38.25 | 40.70 | 40.45 |

Table 3.4 (cont'd)

| IR Source | Radio Source(s) | $\log L$(FUV) | $\log L$(NUV) | $\log L$(H$\alpha$) | $\log L(8)$ | $\log L(24)$ |
|---|---|---|---|---|---|---|
| 01-09 | 8 | 40.58 | 40.59 | 38.87 | 40.95 | 40.50 |
| 02-03 | 3 | 39.96 | 39.96 | 37.98 | 40.17 | 39.75 |
| 03-03 | 5 | 40.35 | 40.24 | 39.09 | 41.04 | 40.74 |
| 04-03 | 10 | 41.15 | 41.20 | 38.71 | 40.78 | 40.43 |
| 05-02 | 7 | 41.73 | 41.33 | 39.37 | 41.30 | 41.20 |
| 05-03 | 9 | 40.33 | 40.48 | 38.75 | 40.97 | 40.67 |
| 05-04 | 6 | 41.05 | 41.02 | 38.76 | 40.71 | 40.48 |
| 05-06 | 11 | 40.40 | 40.44 | 38.21 | 40.32 | 40.01 |
| 07-02 | 95,97 | 41.13 | 41.10 | 39.22 | 41.32 | 41.04 |
| 07-04 | 92 | 41.08 | 41.00 | 38.98 | 41.18 | 40.84 |
| 07-05 | 91 | 41.14 | 41.13 | 39.34 | 41.17 | 40.94 |
| 07-06 | 89 | 40.88 | 40.90 | 39.03 | 40.97 | 40.82 |
| 07-07 | 85 | 40.75 | 40.76 | 38.78 | 40.98 | 40.70 |
| 07-13 | 73,75 | 40.29 | 40.30 | 38.70 | 40.93 | 40.61 |
| 08-02 | 83 | 40.74 | 40.78 | 38.88 | 41.19 | 41.03 |
| 08-04 | 93 | 40.60 | 40.66 | 38.60 | 40.95 | 40.64 |
| 08-05 | 98 | 40.61 | 40.60 | 38.67 | 40.92 | 40.59 |
| 08-06 | 96 | 40.54 | 40.51 | 38.85 | 40.90 | 40.57 |
| 09-05 | 94 | 40.88 | 40.83 | 39.29 | 41.09 | 41.04 |
| 09-06 | 99,100 | 40.78 | 40.78 | 38.99 | 40.81 | 40.74 |
| 09-07 | 101 | 40.67 | 40.63 | 38.86 | 40.70 | 40.53 |
| 09-08 | 102 | 40.58 | 40.51 | 38.28 | 40.47 | 39.88 |

Table 3.4 (cont'd)

| IR Source | Radio Source(s) | $\log L$(FUV) | $\log L$(NUV) | $\log L$(H$\alpha$) | $\log L(8)$ | $\log L(24)$ |
|---|---|---|---|---|---|---|
| 09-11 | 104 | 40.68 | 40.63 | 37.86 | 39.95 | 39.47 |
| 11-03 | 103 | 40.40 | 40.32 | 38.66 | 40.34 | 40.30 |

Table 3.5. X-ray Counterparts to Radio Sources

| | Flux Density | | Spectral | | | |
|---|---|---|---|---|---|---|
| Source | 20cm | 6cm | Index | CXOU | $L_x$ | X-ray ID |
| 4 | 84±22 | 102±18 | +0.15 | J132939.0+471324 | 5E37 | XRB/SNR |
| 12 | 123±21 | 43±15 | −0.86 | J132949.1+471257 | 3E37 | ABS |
| 47 | 84±21 | 40±13 | −0.60 | J132952.1+471127 | 6E37 | SNR |
| 49 | 87±29 | 50±13 | −0.45 | J132952.2+471129 | 4E37 | SNR |
| 52 | 162±26 | 59±13 | −0.82 | J132952.7+471121 | 3E37 | SNR |
| 58[a] | 162±26 | 93±14 | −0.45 | J132954.2+471130 | 4E37 | SNR |
| 65 | 406±21 | 280±17 | −0.30 | J132955.0+470922 | 7E37 | XRB/SNR |
| 68 | 158±23 | 61±14 | −0.78 | J132955.2+471046 | 1E37 | SNR |
| 73 | 101±23 | 80±16 | −0.19 | J132955.4+471402 | 2E37 | SNR |
| 79 | 319±25 | 230±13 | −0.26 | J132955.9+471144 | 7E37 | SNR |
| 84 | 128±22 | 59±14 | −0.63 | J132957.5+471037 | 3E37 | SNR |
| 95 | 131±22 | 62±15 | −0.61 | J133001.3+471244 | 2E37 | ABS |
| 107 | 500±22 | 482±20 | −0.03 | J133011.0+471041 | 1E38 | XRB |

[a] Coincident with SN 1994I.

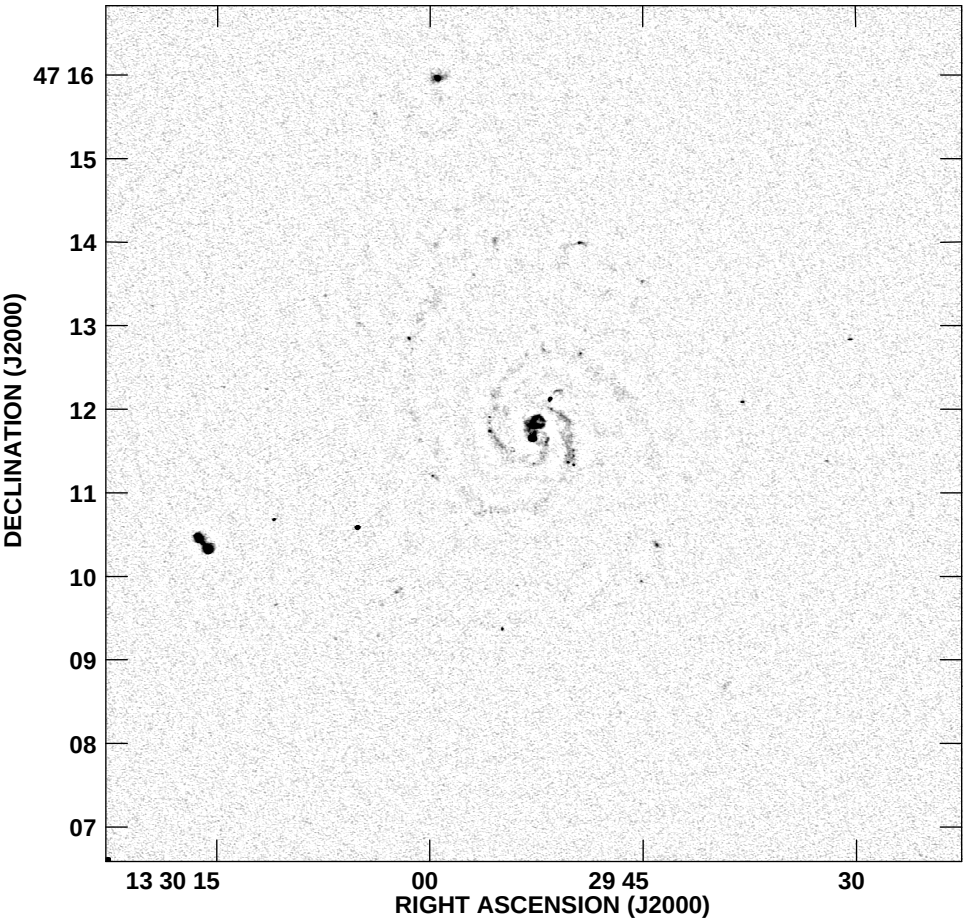



Figure 3.1 20 cm radio map of M51. The greyscale limits are -1 to 500 $\mu$Jy.

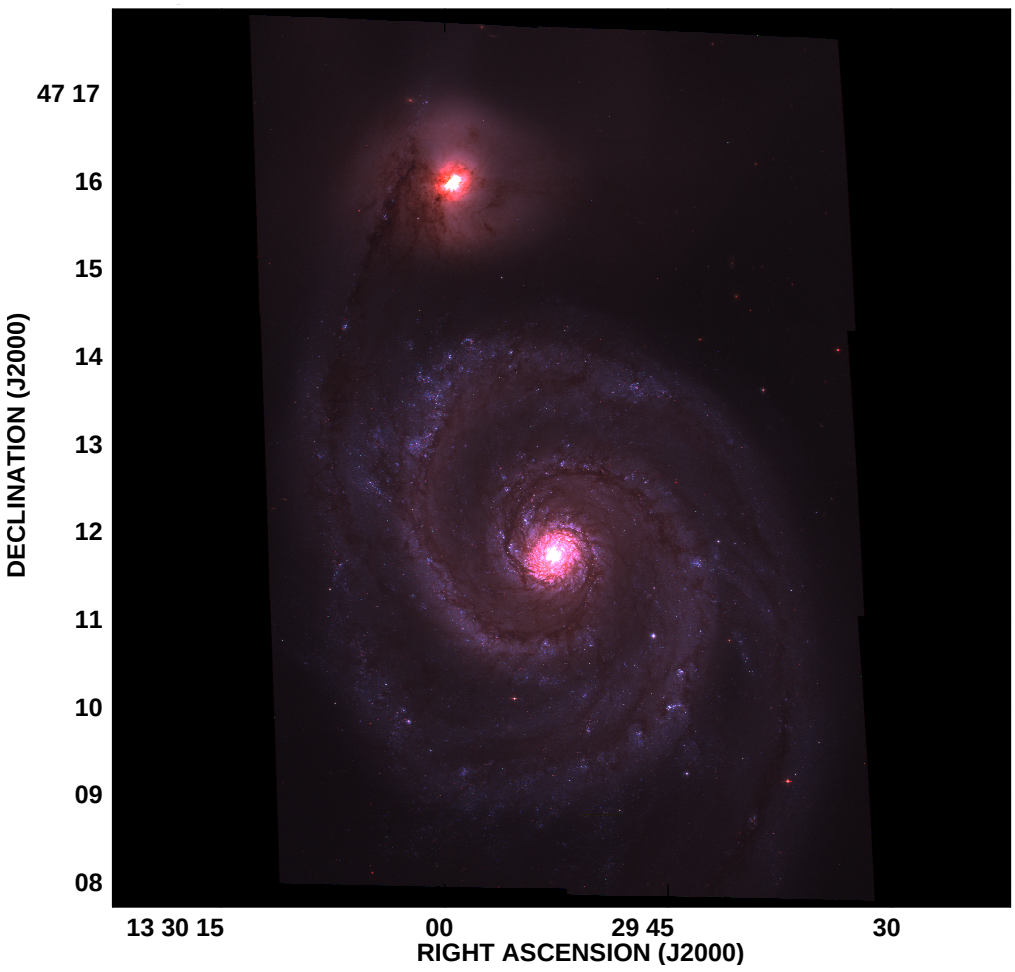



Figure 3.2 Three color optical image of M51 from HST/ACS. *Image Credit:* NASA, ESA, S. Beckwith, and The Hubble Heritage Team (STScI/AURA)

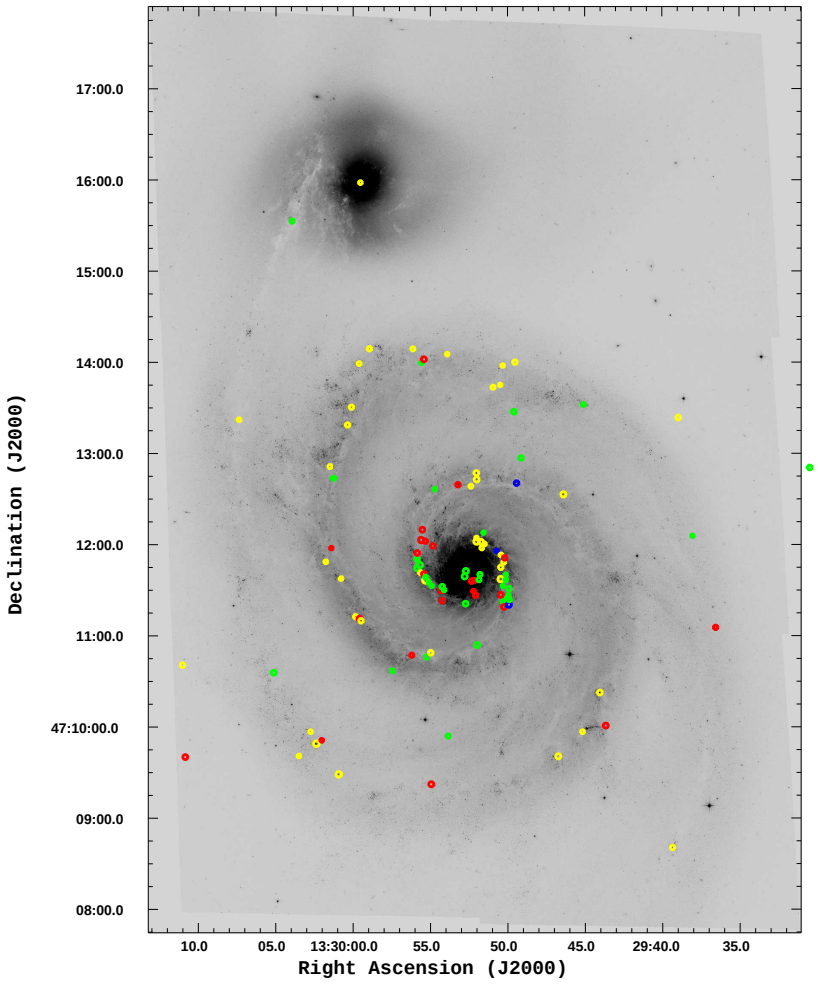



Figure 3.3 I Band image of M51 with radio sources overlayed. The radio sources have been binned according to their spectral index: steep spectrum sources in green, flat spectrum sources in yellow, inverted spectrum sources in blue, and indeterminate flat/steep spectrum sources in red.

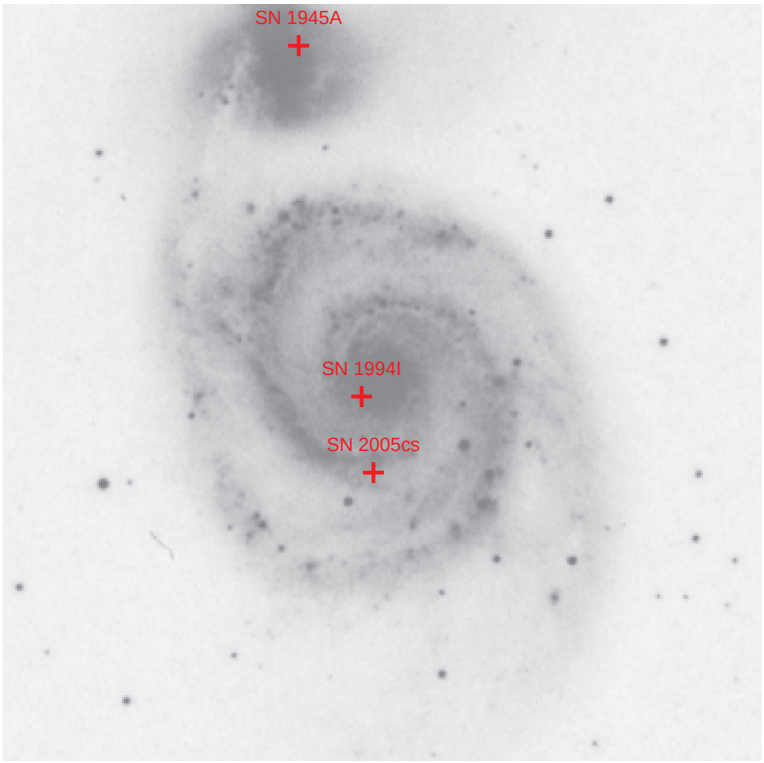



Figure 3.4 A DSS optical image of M51. The crosses indicate the positions of the historical supernovae in the galaxy

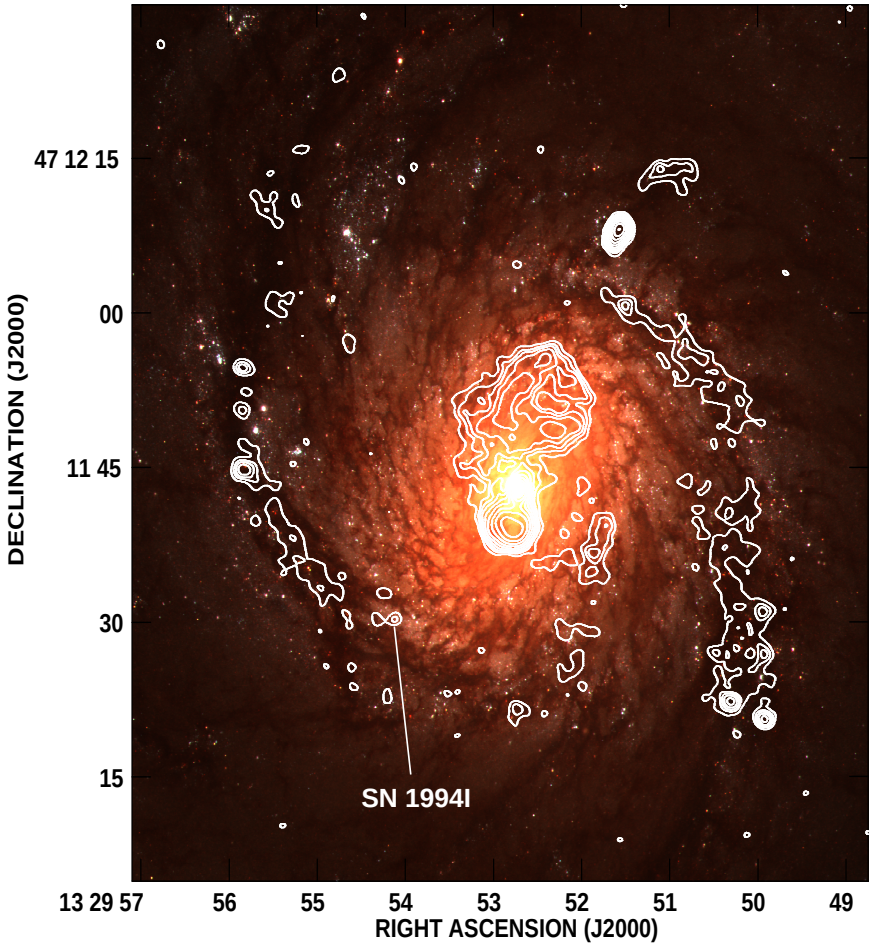



Figure 3.5 Radio contours of 6 cm emission overlayed on an optical HST image of the central 3.7 kpc M51. The position of SN 1994I is marked.

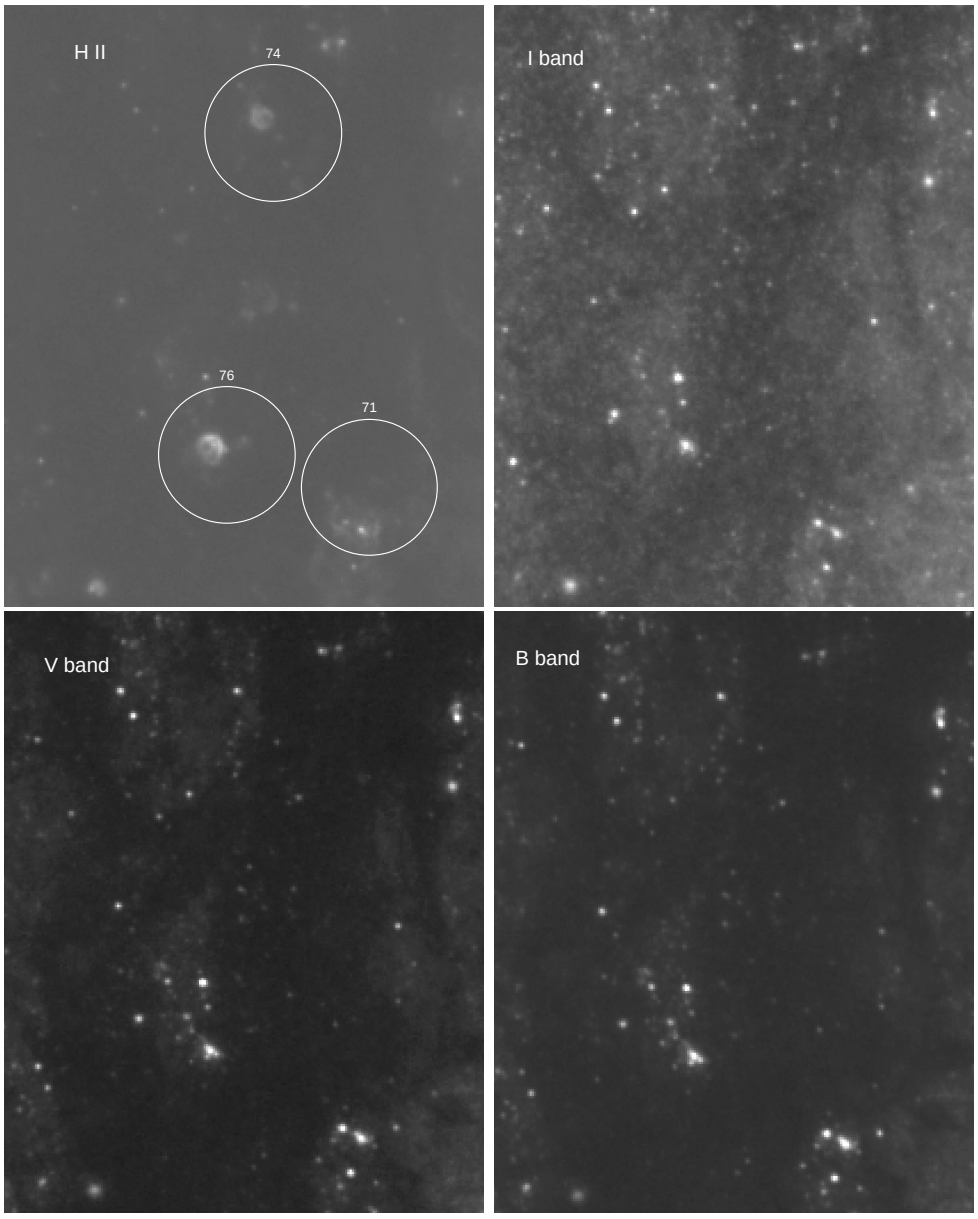



Figure 3.6 Blowup of a small area within M51. The H II image shows the positions of radio sources, indicated by circles, associated with optical emission. Two of the H II sources indicate shell structure indicative of SNRs. The remaining images show no shell emission. The emission in the other optical bands are predominantly due to starlight.

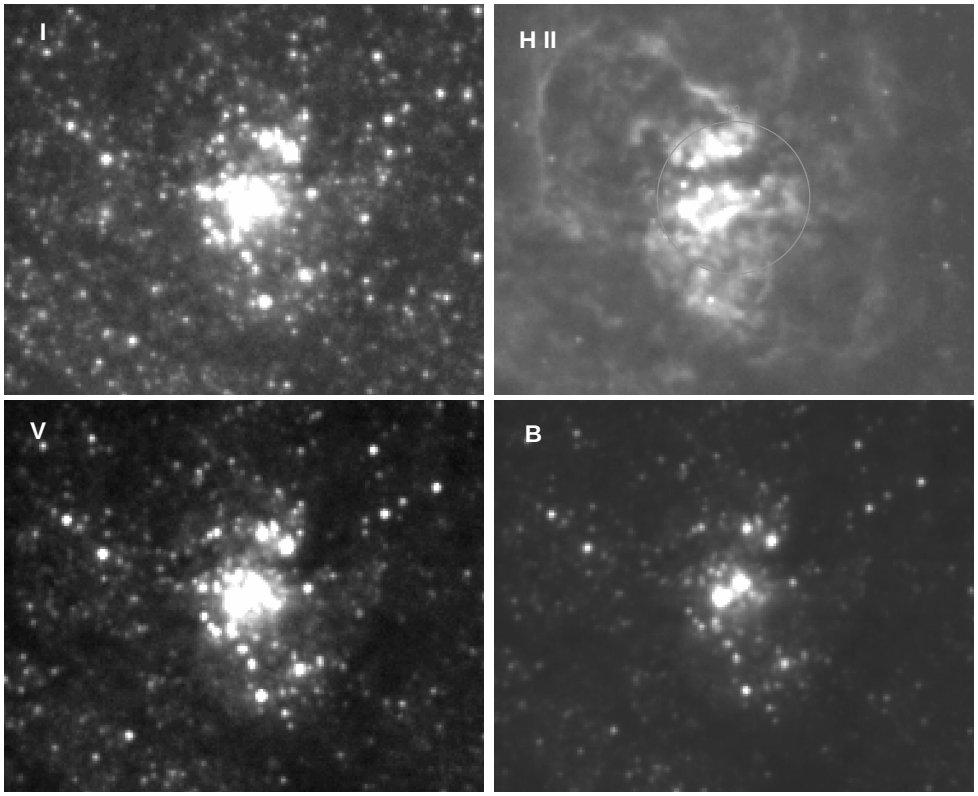



Figure 3.7 Many sources, like source 89 shown above lie in dense stellar clusters. Source 89 (circled in the H II image) is a flat spectrum radio source which is coincident with a large H II region. In I, V, and B bands it is quite evident that the photoionization of the H$\alpha$ cloud is powered by the stars in the cluster.

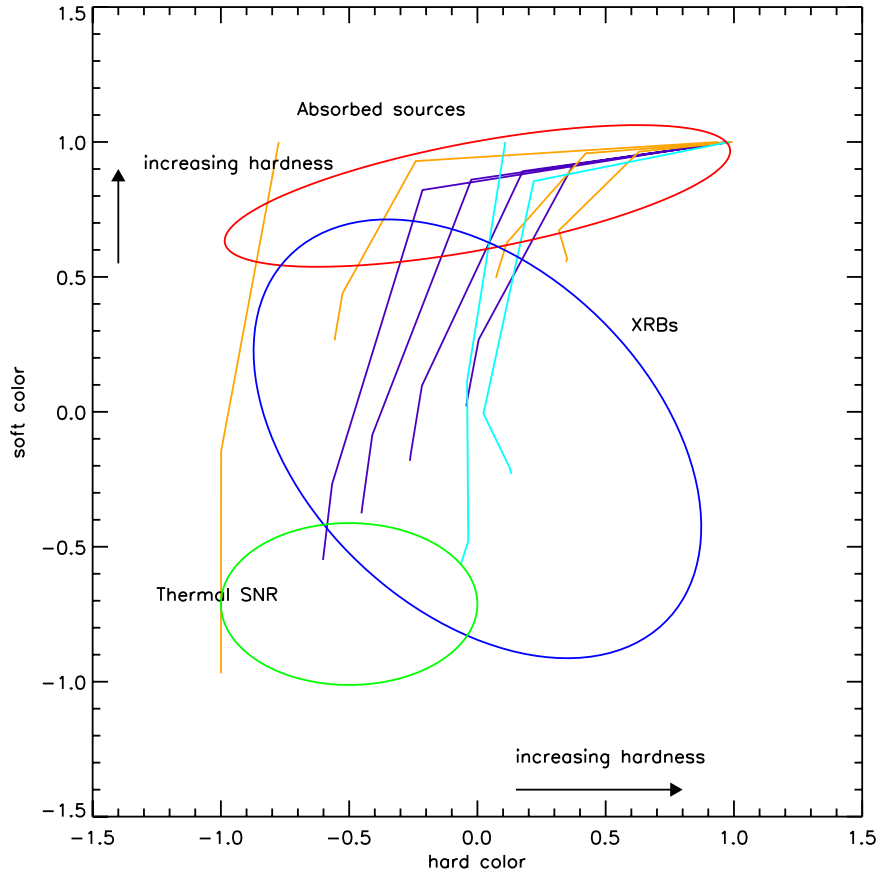



Figure 3.8 Model X-ray color-color diagram. The purple lines are power-law spectra with photon index increasing from left to right ($\Gamma$ = 1, 1.5, 2, and 2.5) and absorption increasing from bottom to top (0 to $10^{24} cm^{-2}$). The orange lines are thermal spectra with temperature increasing from left to right (0.5, 1, 1.5, and 2 keV) and absorption increasing as with the power-law spectra. The light blue lines are power-law plus blackbody spectra. The ellipses mark the likely location of thermal SNRs, X-ray binaries and sources with very heavily absorbed spectra (where color-classification becomes difficult).

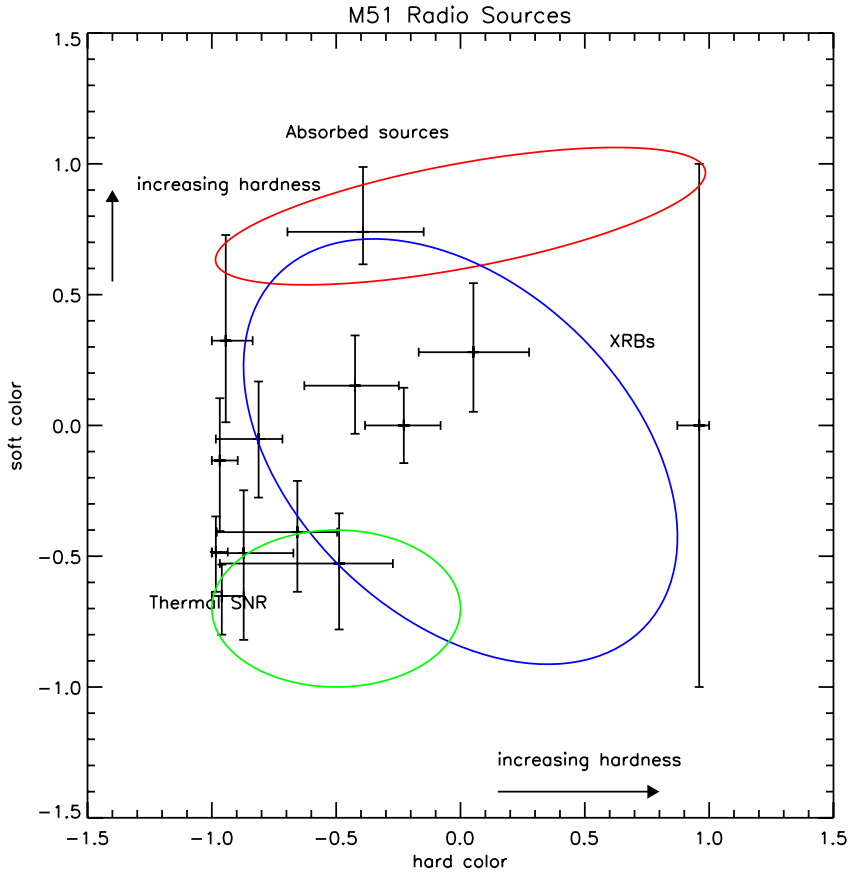



Figure 3.9 X-ray color-color diagram following Kilgard et al. (2005) for radio sources with X-ray counterparts.

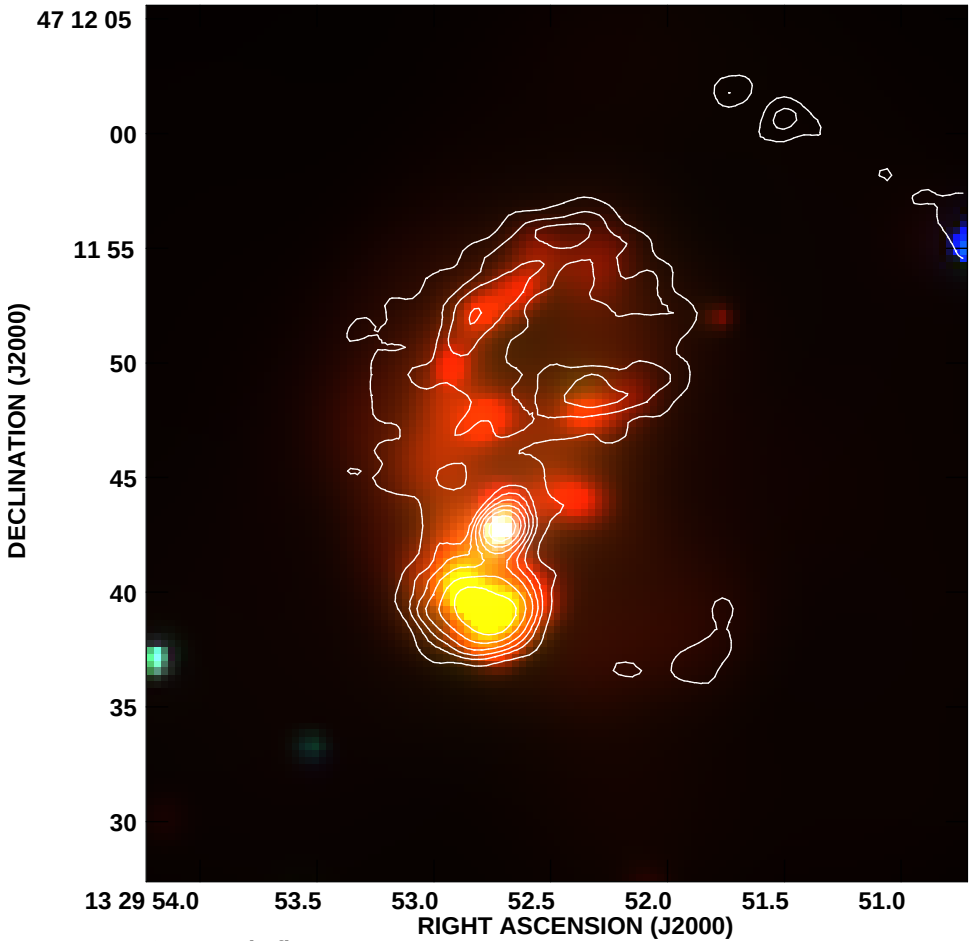



Figure 3.10 An enlargement of the nuclear region of M51. The colors represent X-ray emission, while the contours represent 20 cm radio emission. The smallest point-like feature in each image is $\sim 1.0''$. Overlay of 20 cm contours onto X-ray emission from the nucleus of M51.

# Chapter 4

# A Study of Compact Radio Sources in Nearby Face-on Spiral Galaxies. III. Multiwavelength Analyses of M101 and NGC 3184

## 4.1 Introduction

This chapter contains a preliminary presentation of the work that I have performed on the radio observations of M101 and NGC 3184. It is my intention to complete the analyses and submit the paper for publication as soon as possible after my doctoral work is complete.

M101 is a large, nearly face-on ($i \sim 17$ deg, Zaritsky et al., 1990), grand-design spiral galaxy. It has been the host to three historical supernovae: SN 1909A, SN 1951H, and SN 1970G. Its proximity and large size has made M101 an ideal candidate for the study of star formation and H II regions (e.g., Scowen et al., 1992).

NGC 3184 is a also a large, nearly face-on spiral. NGC 3184 has a relatively low star formation rate (Kennicutt et al., 2003) based in H$\alpha$ studies. Despite this, NGC 3184 has played host to four historical supernovae: SN 1921B, SN 1921C, SN 1937F, and SN 1999gi.

The published distances to M101 range from 3.3 Mpc(de Vaucouleurs, 1979b) to 7.7 Mpc (Feldmeier et al., 1997). We have chosen to adopt distance of 7.7 Mpc for M101 based on the PLNF, same method used for M51. Distance determinations to NGC 3184 range from 7.2 Mpc (Tully-Fisher; Pierce, 1994) to 13.8 Mpc (group membership, Freedman et al., 2001).

We have adopted the distance of Freedman et al. (2001), determined by group association with a galaxy whose distance is Cepheid-established.

Both galaxies have large H I halos (Walter et al., 2005) that extend far beyond our current radio fields.

I will present preliminary results based on radio observations of M101 and NGC 3184. First, the observations and data processing will be described. Second, I will present the resulting source properties and analysis. Finally, I will briefly mention the nature of a few sources. Finally, I will give a mention the work that is still required to finish this project.

## 4.2 Data

Our first observation of M101 was performed with the VLA while in A-configuration at 20cm on 7 March 2002. We performed a 6cm observation in B-configuration on 23 November 2004. Both observations used B1331+305 as the primary calibrator. B1331+305 was calculated to have a flux density of 14.5 Jy, and 14.9 Jy in the respective IFs. A secondary calibrator, B1349+536, was used to correct for atmospheric phase fluctuations and to set the final flux scale. Details of the M101 observations are shown in Table 4.1.

We performed two short observations of NGC 3184. The 20 cm observations were performed on 7 March and 5 April, 2002, for a total of 3.6 hr in A-configuration. We were originally awarded a 6.7 hr 6 cm observation on 28 November, 2003 in B-configuration, but an observer error caused the collection of just the secondary calibrator data. The observation was rescheduled in the same configuration and we obtained 3.6 hr data on 16 January, 2004. Details of the NGC 3184 observations are given in Table 4.2.

Table 4.1 VLA Observations of M101

| Parameter | 20cm | 6cm |
|---|---|---|
| Frequency (GHz) ..... | 1.425 | 4.860 |
| Observing Date ..... | 7 March 2002 | 23 November 2003 |
| Observing Time (hr) ... | 6.5 | 8.7 |
| Configuration ..... | A | B |
| Primary Beam HPBW . | $30'$ | $8'$ |
| Clean Beam ..... | $1\farcs36 \times 1\farcs20$ | $1\farcs22 \times 1\farcs17$ |
| rms noise ($\mu$Jy beam$^{-1}$) | 16.4 | 10.8 |

Table 4.2 VLA Observations of NGC 3184

| Parameter | 20cm | 6cm |
|---|---|---|
| Frequency (GHz) ..... | 1.425 | 4.860 |
| Observing Date ..... | 7 March, 5 April 2002 | 28 November 2003 |
| Observing Time (hr) ... | 3.6 | 6.7 |
| Configuration ..... | A | B |
| Primary Beam HPBW . | $30'$ | $8'$ |
| Clean Beam ..... | $1\farcs96 \times 1\farcs26$ | $1\farcs41 \times 1\farcs13$ |
| rms noise ($\mu$Jy beam$^{-1}$) | 41.9 | 15.4 |

## 4.3 Reduction and Analysis

All data was processed using the Astronomical Image Processing System (AIPS) provided by NRAO. Final maps were calculated using the AIPS task IMAGR with a Brigg's robustness parameter of 0. This value helps to minimize rms noise while allowing for excellent point source detection. The final maps are shown in Figures 4.1 and 4.2

The initial source list of M101 was obtained using the AIPS task SAD. The list was then inspected manually to remove multiple sources attributed to extended emission. There is one background galaxy to the northeast of the nucleus that was detected as multiple sources. The resulting sources were then fit using IMFIT and JMFIT to determine peak flux densities and spectral indices. The source modes used in the fitting tasks was a simple two-dimensional Gaussian. There was no diffuse emission, so there was no need for the addition of a background component in the fit. The results of those fits are presented in Table 4.3.

The observations of NGC 3184 yielded a much smaller set of point sources. For this galaxy, only a manual inspection was used to compile the source list. The sources were fit in an identical manner to those in M101, and the results are listed in Table 4.4.

## 4.4 Discussion

### 4.4.1 M101

Table 4.3 lists the positions and flux densities of all point sources detected in M101. Flux densities are in units of $\mu$Jy beam$^{-1}$. Figure 4.3 shows the positions of the radio sources on a DSS image of the galaxy along with the positions of two the historical SNe.

Like in M51, the sources tend to lie in the spiral arms of the M101.

None of the historical SNe in M101 lie within our field. SN 1970G lies to the north of a large H II region as seen in Figure 4.3 (Stockdale et al., 2001b). Likewise, SN 1951H is located near a large H II complex. SN 1909A exploded far from the center of the galaxy, and lies outside the field of the DSS image.

The sources 1, 2 and 4 take the form of a double lobed background galaxy, like the one seen in M83 (Stockdale et al., 2001a; Maddox et al., 2003). The inverted (source 2) core could be due to variability of the AGN, while 1 and 4 show steep spectra consistent with the lobes of the M83 background (Cowan et al., 1994).

Source 5 and 28 are inverted sources. Both source lie in low brightness regions of the galaxy. Based on that, we have an initial classification of these sources as background.

Figure 4.4 shows the H II region complex NGC 5461, located within one of the spiral arms of M101. The central source (Source 26) is the brightest source in both radio observations. It has 20cm and 6cm peak fluxes of 1.43 mJy and 1.18 mJy, respectively. This gives a spectral index of $\alpha = -0.16 \pm 0.12$. In an analysis of a *XMM-Newton* observation of M101, Jenkins et al. (2004) report a potential X-ray binary and possible intermediate mass black hole candidate.

In an optical study of the nucleus, Moody et al. (1995) saw evidence for a bipolar outflow. A later X-ray study using *Chandra* showed no evidence for outflow (Kuntz et al., 2003). Likewise, our observations are unable to detect any evidence for outflow, due to the resolution. Observations at lower resolution would be require to detect such emission.

Table 4.3. Fluxes and Spectral Indices of Point Sources in M101

| | Position | | Peak Flux | | |
|---|---|---|---|---|---|
| Source | RA | Dec | 20 cm | 6 cm | Spectral Index |
| 1 | 14 02 37.60 | 54 24 56.43 | 317±18 | 113±41 | -0.84±0.37 |
| 2 | 14 02 38.73 | 54 24 53.91 | 105±18 | 186±43 | +0.46±0.29 |
| 3 | 14 02 39.05 | 54 22 28.44 | 168±15 | 213±23 | +0.19±0.14 |
| 4 | 14 02 39.95 | 54 24 47.09 | 371±17 | 203±39 | -0.49±0.20 |
| 5 | 14 02 52.07 | 54 19 47.04 | 162±16 | 265±12 | +0.40±0.11 |
| 6 | 14 02 52.25 | 54 18 51.17 | 200±15 | 76±15 | -0.79±0.21 |
| 7 | 14 02 53.33 | 54 18 56.14 | 187±15 | 68±13 | -0.83±0.21 |
| 8 | 14 02 56.92 | 54 16 19.64 | 1021±15 | 401±23 | -0.76±0.06 |
| 9 | 14 02 56.93 | 54 25 41.59 | 180±16 | 79±24 | -0.68±0.31 |
| 10 | 14 02 59.15 | 54 25 13.23 | 181±14 | 196±19 | +0.06±0.12 |
| 11 | 14 03 03.35 | 54 24 10.33 | 489±17 | 184±13 | -0.79±0.08 |
| 12 | 14 03 04.69 | 54 19 25.59 | 119±15 | 107±9 | -0.09±0.15 |
| 13 | 14 03 05.88 | 54 20 23.03 | 106±14 | 55±9 | -0.53±0.21 |
| 14 | 14 03 12.42 | 54 20 54.93 | 303±16 | 140±7 | -0.63±0.07 |
| 15 | 14 03 14.70 | 54 17 37.86 | 240±16 | 103±14 | -0.69±0.15 |
| 16 | 14 03 18.10 | 54 21 57.69 | 716±14 | 348±8 | -0.59±0.03 |
| 17 | 14 03 23.35 | 54 16 30.48 | 108±15 | 88±19 | -0.17±0.25 |
| 18 | 14 03 23.57 | 54 25 28.76 | 105±15 | 136±18 | +0.21±0.20 |

Table 4.3 (cont'd)

| | Position | | Peak Flux | | |
|---|---|---|---|---|---|
| Source | RA | Dec | 20 cm | 6 cm | Spectral Index |
| 19 | 14 03 27.69 | 54 23 59.89 | 638±16 | 208±14 | -0.92±0.07 |
| 20 | 14 03 29.96 | 54 22 45.62 | 673±15 | 260±12 | -0.77±0.05 |
| 21 | 14 03 31.35 | 54 21 14.44 | 186±14 | 157±12 | -0.14±0.10 |
| 22 | 14 03 34.05 | 54 18 36.97 | 142±16 | 128±14 | -0.08±0.16 |
| 23 | 14 03 35.95 | 54 22 02.35 | 108±15 | 54±14 | -0.56±0.29 |
| 24 | 14 03 38.67 | 54 18 49.38 | 214±16 | 74±16 | -0.86±0.22 |
| 25 | 14 03 39.85 | 54 18 56.81 | 173±14 | 147±18 | -0.13±0.15 |
| 26 | 14 03 41.38 | 54 19 04.39 | 1430±14 | 1181±17 | -0.16±0.02 |
| 27 | 14 03 42.00 | 54 19 24.48 | 155±14 | 142±19 | -0.08±0.16 |
| 28 | 14 03 46.09 | 54 16 16.01 | 279±16 | 833±52 | +0.89±0.08 |

### 4.4.2 NGC 3184

Table 4.4 lists the sources detected in NGC 3184. Most of the sources that were present in both observational bands exhibit non-thermal spectral indices. The sources not detectable in 20 cm have flat or inverted spectral limits. These sources could be emission from H II regions. The non-thermal Source 5 is nucleus of the galaxy. Figure 4.5 shows the radio sources overlayed onto a DSS image of NGC 3184, as well as the positions of the historical SNe.

Most of sources lie outside the brightest portion of the galaxy, within the large H I disk of the galaxy (Walter et al., 2005). Source 1 appears to be coincident with a foreground star.

We detect no emission from any of the historical SNe. Upper limits for the 20 cm flux are rather high (125 $\mu$Jy beam$^{-1}$) due short observations. SN 1999gi occurred near an H II region on an inner spiral arm. The remaining SNe were seen far from the inner part of the galaxy.

Sources 7 and 8 lie near the edge of our field. They are positioned near the reported optical position of SN 1921C (Figure 4.6). The offset from the SN make it unlikely that these sources are associated with the shock from the SN. They are likely a background radio galaxy. No X-ray analysis can be performed on this sources, as it lies off the ACIS chip in the *Chandra* data.

The brightest sources in the field, sources 2 and 10, could also be background sources. We need counterparts in other bands to confirm this.

Source 6 lies in one of the spiral arms near several H II regions. We tentatively classify this source as an SNR.

Our observations of NGC 3184 are not very deep. With deeper observations it is likely that we could detect more sources, though not as many is in M51 (Chapter 3).

## 4.5 Forthcoming Work

There is still much work that must be done. We must analyze the *Chandra* observations to look for counterparts to the radio sources in both galaxies. A search of optical archives will be done to look for optical sources. These optical observations will give us important

Table 4.4. Flux Densities and Spectral Indices of Point Sources in NGC 3184

| | Position | | Peak Flux | | |
|---|---|---|---|---|---|
| Source | RA | Dec | 20 cm | 6 cm | Spectral Index |
| 1 | 10 17 58.02 | 41 27 50.69 | ··· | 270±23 | $> +0.63$ |
| 2 | 10 18 08.24 | 41 30 07.88 | 709±41 | 411±29 | $-0.44\pm0.09$ |
| 3 | 10 18 08.95 | 41 27 52.08 | ··· | 149±16 | $> +0.14$ |
| 4 | 10 18 16.16 | 41 20 35.49 | ··· | 209±29 | $> +0.42$ |
| 5 | 10 18 16.88 | 41 25 27.45 | 252±36 | 150±13 | $-0.42\pm0.17$ |
| 6 | 10 18 23.49 | 41 26 55.98 | 198±35 | 120±14 | $-0.41\pm0.21$ |
| 7 | 10 18 23.63 | 41 21 08.28 | 321±40 | 167±24 | $-0.53\pm0.19$ |
| 8 | 10 18 23.58 | 41 21 01.52 | 176±41 | 72±22 | $-0.73\pm0.38$ |
| 9 | 10 18 36.59 | 41 25 48.76 | ··· | 102±30 | $> -0.17$ |
| 10 | 10 18 42.48 | 41 30 04.60 | 704±41 | 293±63 | $-0.71\pm0.22$ |

allow us to further constrain the properties of these sources and aid in classification. The treatment will be similar to the treatments of M83 and M51. These galaxies, and the ones discussed in the previous chapters, give us an excellent sample for studying the diversity of source populations in spiral galaxies.

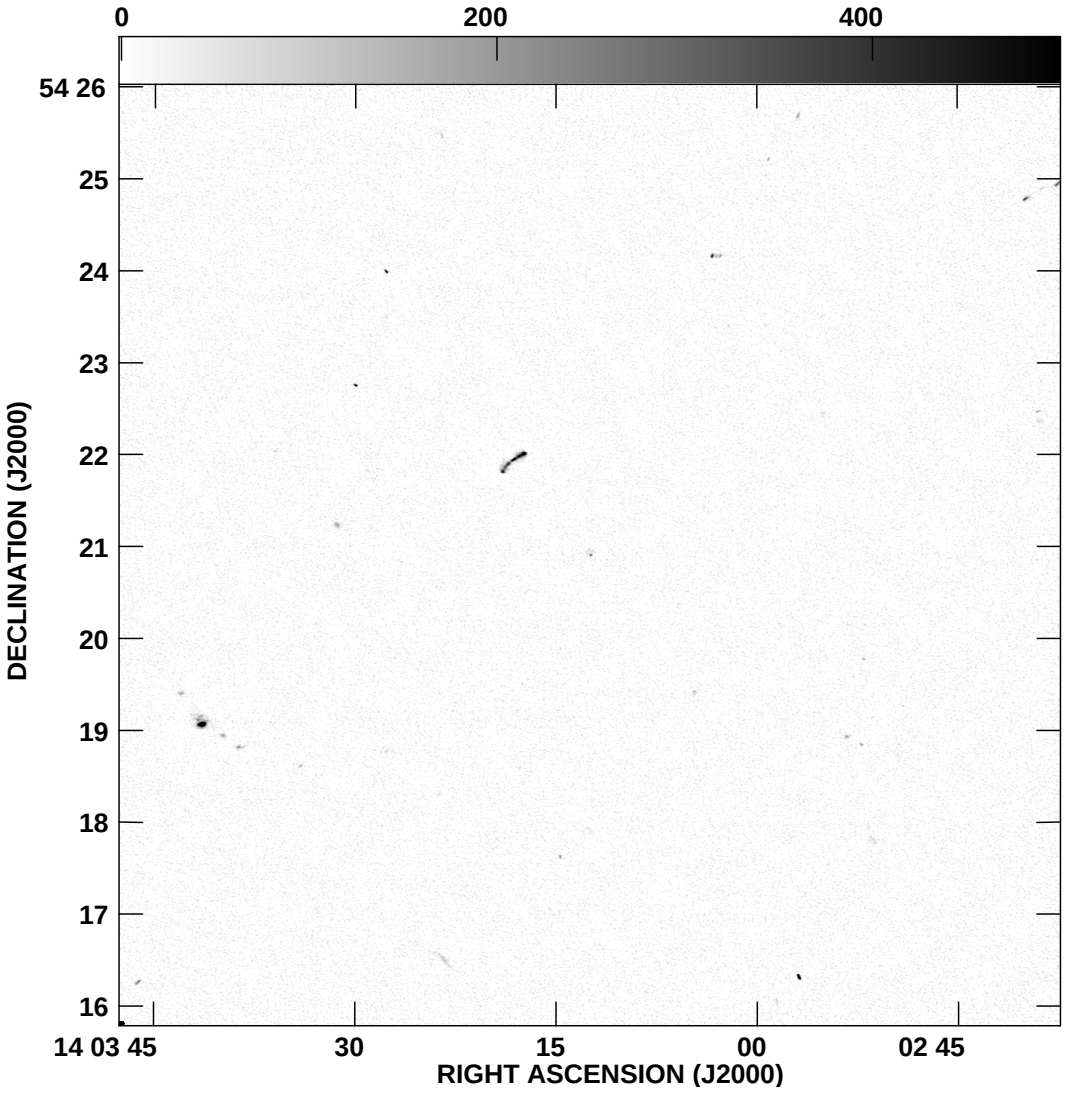



Figure 4.1 20 cm Radio map for M101. Greyscale is linear from -1 to 500 $\mu$Jy.

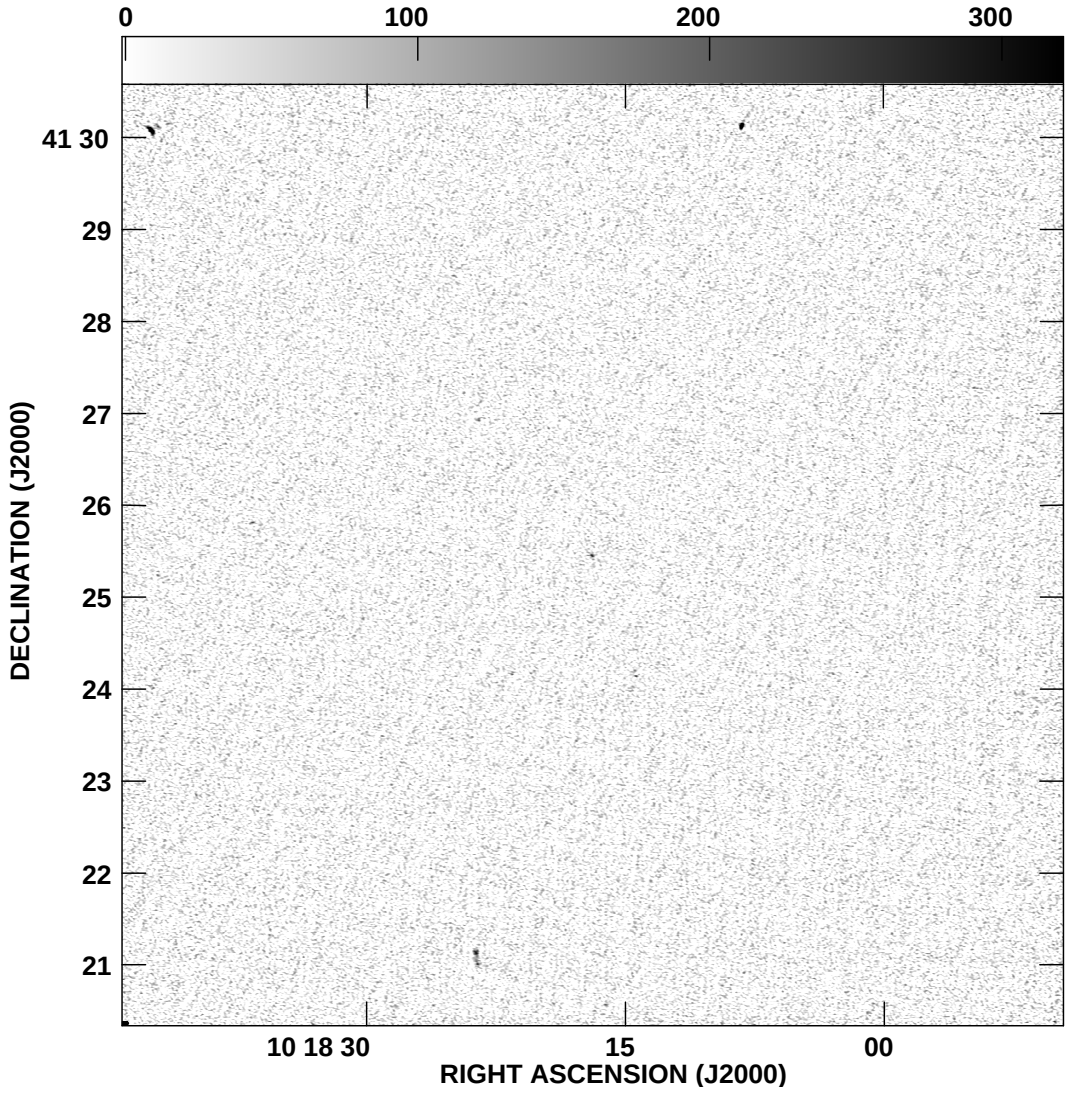



Figure 4.2 Same as Figure 4.1 for NGC 3184. Greyscale is linear from -1 to 321 $\mu$Jy.

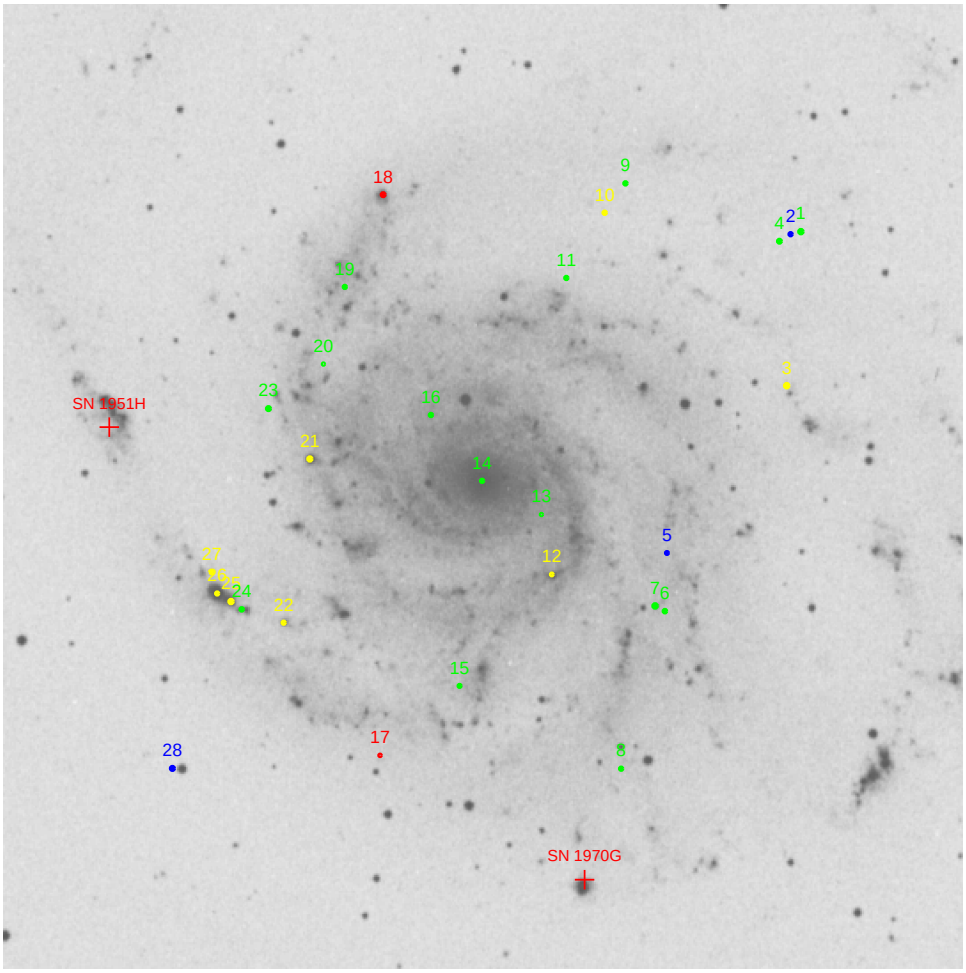



Figure 4.3 Radio sources overlayed on a DSS image M101. Yellow circles are flat spectrum sources. Green are steep spectrum. Blue are inverted spectrum. Red are undetermined due to uncertainty. Red crosses show the positions of historical supernovae SN 1951H and SN 1970G. The SNe lie outside our radio field.

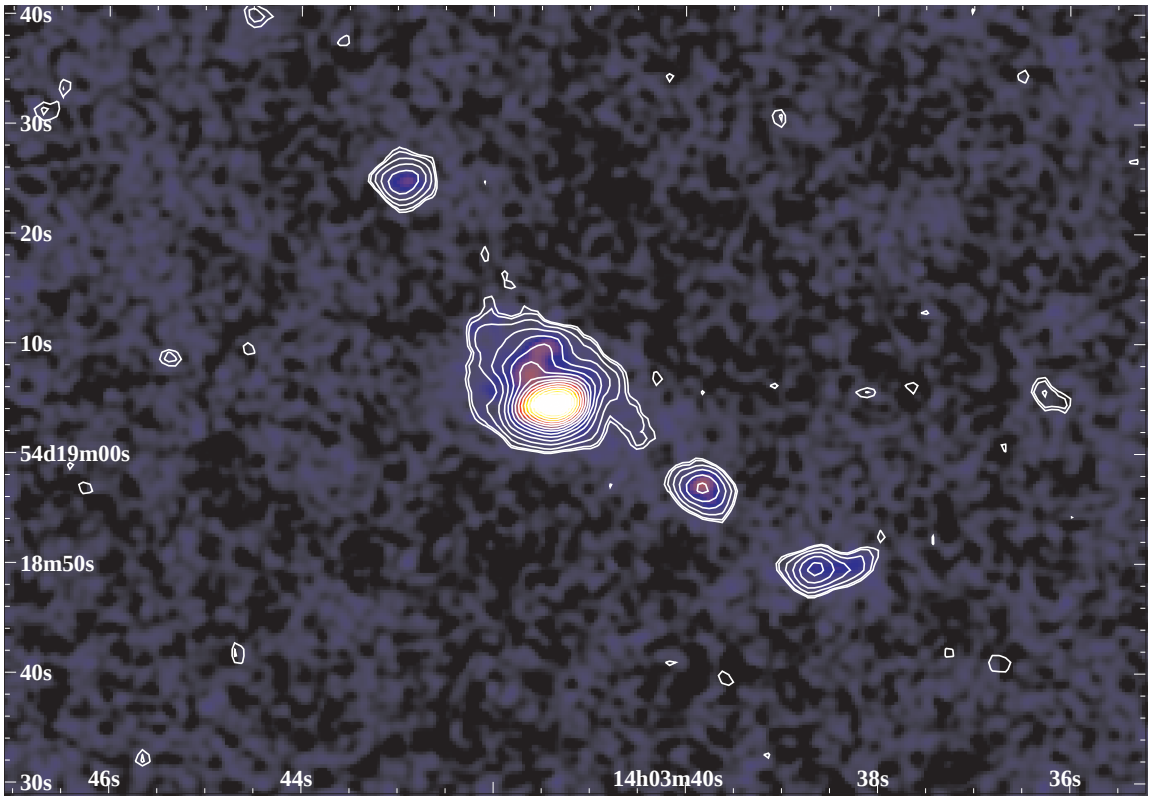



Figure 4.4 A close-up of NGC 5461 at the end of spiral arm in M101. Colors show 6cm emission while the contours are 20cm emission.

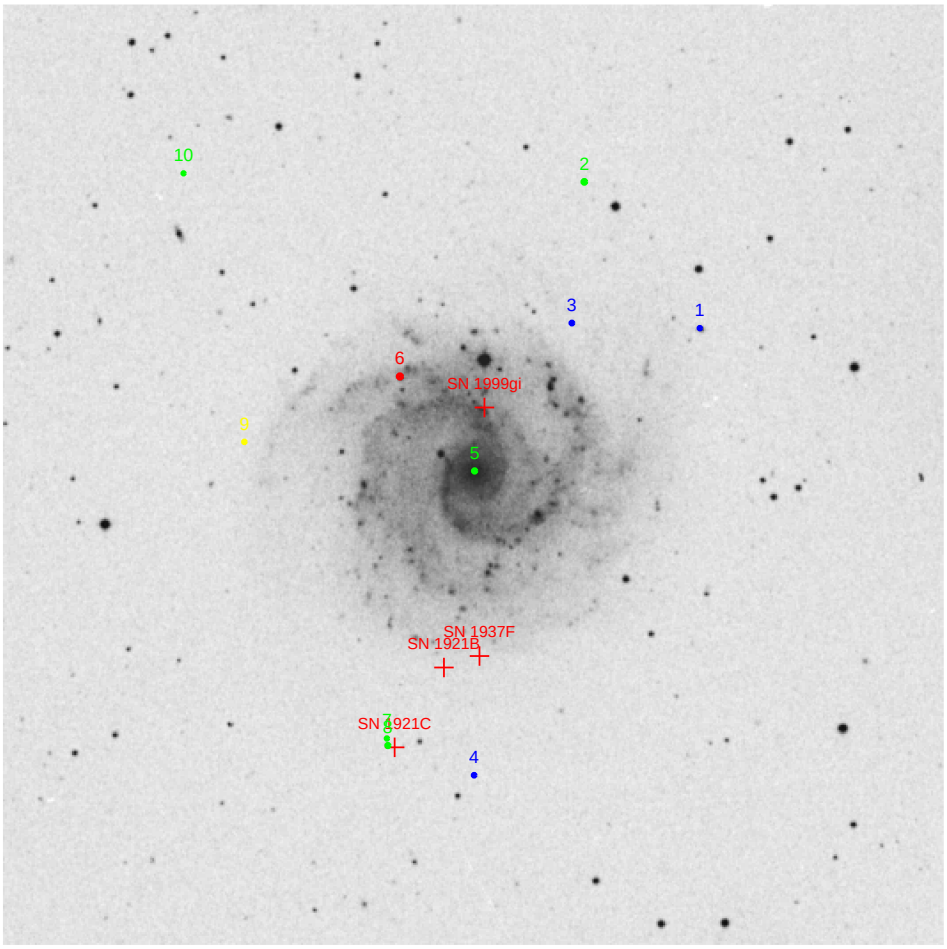



Figure 4.5 Same as Figure 4.3 for NGC 3184. Historical SN 1909A lies outside the DSS field and our radio field.

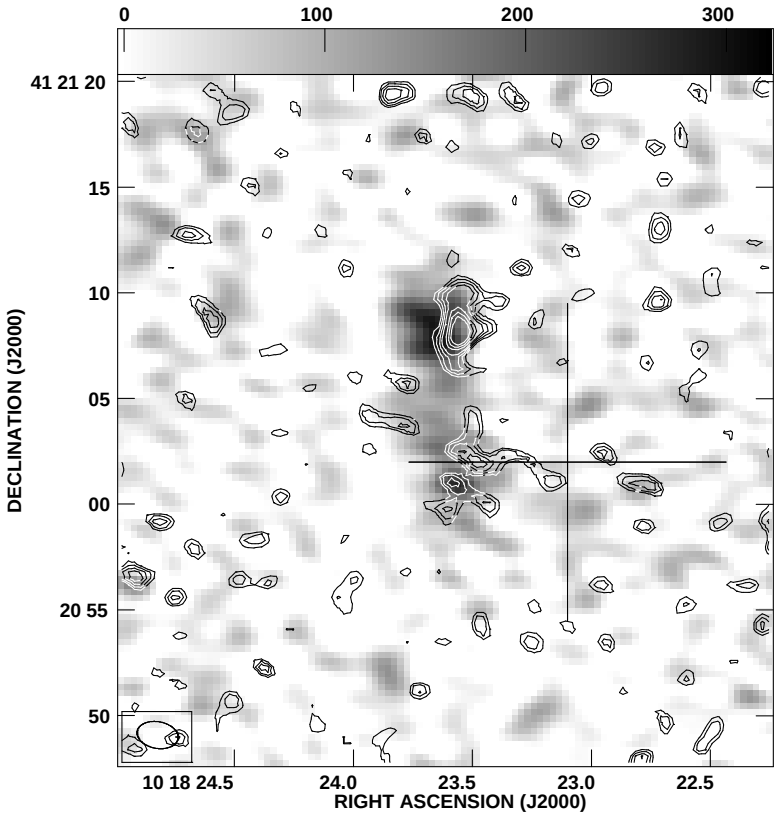



Figure 4.6 Blow-up of small region near NGC 3184. Greyscale indicates the 20cm emission and the contours show 6cm emission. The cross indicates the reported optical position of Type I SN 1921C. The size of the cross reflects a 15" positional uncertainty in the optical position.

# Chapter 5

# An *XMM-Newton* Observation of the Seyfert 2 Galaxy NGC 6300: II. Multiwavelength Analysis of Non-nuclear Sources

## 5.1 Introduction

### 5.1.1 Ringed, Barred Spiral Galaxies

Barred spiral galaxies with resonance rings are common objects in the nearby universe. Nearly half of disk galaxies have some kind of ring structure Buta (1984). The study of these ringed, barred spiral galaxies may yield powerful insight into the understanding of galaxy evolution and morphology. In this introduction we will provide some of the properties of this class of object. Ringed, barred spiral galaxies are often alternately referred to as resonance ring galaxies. Both terms will be used interchangeably throughout this paper. Much of the information in this section may be found in Buta (1999), and references therein.

Rings in galaxies can form in different ways. The most dramatic rings form from the collision of two galaxies. This catastrophic disturbance produces a shock front that causes the compression of interstellar gas within the galaxies. The resulting star formation lights up the ring as the shock propagates out.

Another way to form rings is through a perturbation of the gravitational field within the galaxy. Most disk galaxies are unstable to nonaxisymmetric density wave-type perturbations, like those in bars, ovals, or spiral arms. These perturbations produce resonance regions in the form of rings. Gravitational torques from the perturbation causes gas to collect in these regions. The buildup of gas leads to compression and star formation. These rings are typically called *bar-driven* resonance rings.

Resonance rings may also form through the interaction of two closely passing neighbor galaxies. These rings are called *tidally-driven* resonance rings.

There are three types of rings known to exist in resonance ring galaxies. Nuclear rings are the smallest, usually found well inside the bar at a radius of $\sim$ 700 pc. Inner rings circle the bar ends at a typical radius of 6 kpc. They are also usually elongated along the bar axis. Outer rings are usually diffuse features located at radii twice as large as inner rings. They are typically elongated perpendicular to the bar axis. All of these rings are regions of enhanced star formation activity. In some ringed, barred galaxies, the resonances are the only regions that contain significant star formation.

### 5.1.2 NGC 6300

NGC 6300 is one of the nearest (z=0.0037; Mathewson & Ford, 1996) and largest ringed galaxies (Buta, 1987). It is also the least typical. The inner ring structure is composed of tightly wound, dust-riddled spiral arms. No inner ring structure is seen due to the bright Seyfert 2 nucleus which is further confused by the presence of two foreground stars. An optical image of NGC 6300 is shown in Figure 5.1

Study of NGC 6300 began with its discovery by Reynolds (1921). The first photometric



Figure 5.1 B-band image of NGC 6300 from the CTIO 1.5m. This image was used for reference in Ryder et al. (1996). The bar and ring structure is evident. Prominent dust lanes can be seen lacing through the ring.

work was performed by de Vaucouleurs (1956), and kinematic studies were first done in the late 1970s (Sandage, 1978). Beginning with Buta (1984) more detailed study of the structure and kinematics of the galaxy have been undertaken. Some of the results are described below.

Ryder et al. (1996) performed a study of the distribution of neutral hydrogen (HI) in NGC 6300 and a more typical ringed galaxy, NGC 1433. NGC 6300 contained a broader HI disk than did NGC 1433. The halo of the galaxy shows a 20° warp and a short tail. While this could be explained by tidal interactions with passing neighbors, no galaxy has been found near enough to have interacted with NGC 6300 in the recent past. Ryder et al. (1996) also note that the outer pseudoring and the nuclear ring predicted in resonance ring theory are not seen in NGC 6300. They postulate that NGC 6300 may be a developing resonance ring galaxy.

More evidence for an evolutionary scenario is the apparent bar-inner ring misalignment. The bar feature of NGC 6300 is misaligned from the major axis of the ring structure by 80° (Buta, 1984). A broader catalog of ringed, barred galaxies show that this feature is very rare (Buta, 1995). In one case Buta et al. (1999) report analysis of a nuclear starburst in the peculiar galaxy ESO $565-11$. In numerical simulations, they determine that the unusual features in that galaxy may evolve over time to be more consistent with other resonance ring galaxies.

Buta (1995) also suggest that the misalignment might be an indication that, at least in these rare cases, the resonances that form the ring were less influenced by the bar. In the aligned cases the ring patterns seem to be driven by the bar potential. While numerical simulations have been performed, there is still little understanding about how this misalignment occurs.

In a study of HII regions of ringed, barred galaxies, Crocker et al. (1996) noted that NGC 6300 has other interesting differences from others in its class. NGC 6300 contains nearly twice the number of star forming regions as any other galaxy in their sample. Of these almost half (457) had luminosities higher than $L(\mathrm{H}\alpha + [\mathrm{NII}]) \geq 5 \times 10^{37}$ erg s$^{-1}$. Outside the nucleus, all of the HII regions lie in the ring structure. Such vigorous star formation should lead to an elevated supernova rate in turn producing a wealth of X-ray binaries.

Another interesting feature is that the distribution of HII regions peaks in areas perpendicular to the bar. In more typical ringed galaxies, star forming regions are found clustered near where the bar intersects the ring.

In the following sections, we present the results of a multiwavelength study of two

non-nuclear X-ray sources detected in a day long observation by *XMM-Newton*. Using archived observations at radio, infrared and optical wavelengths, we aim to determine the classification of these sources. X-ray analysis of the active nucleus was presented in an earlier paper (Matsumoto et al., 2004).

In section 2 we describe the observations and data reduction. Next we will present the analysis as it stands at the moment. In section 4 we discuss the result of the analysis and give preliminary conclusions as to the nature of the sources.

All X-ray spectral fits include a Galactic neutral hydrogen column density of $9.83 \times 10^{20}$ cm$^{-2}$ (Dickey & Lockman, 1990). Errors quoted are 1-$\sigma$ and upper limits are 5-$\sigma$. Luminosities are determined using the WMAP value of the Hubble constant ($H_0 = 72$ km s$^{-1}$ Mpc$^{-1}$).

## 5.2 Observations

### 5.2.1 X-ray Observations

NGC 6300 was observed from 2001 March 2 3:35 to 16:36 (UT) with *XMM-Newton*. The EPIC instruments consisting of one PN (Strüder et al., 2001) and two MOS (Turner et al., 2001) CCDs were operated in full-frame imaging mode using the medium filter. The background during the whole observation was low so the observation could be used completely. We did not analyze the Reflection Grating Spectrometer (RGS; den Herder et al., 2001) data because of the low number of photons.

The data could not be reduced in the standard way, because the observation was split into two observation IDs, 0059770101 between 03:35–05:32 and 0059770201 between 05:43–

16:34. The first Observation ID contained the PN and MOS data while the second contained the RGS and Optical Monitor (OM) data. However, while the event files in these observation IDs were complete, the housekeeping data only contained the times given above for the observation IDs. Therefore the housekeeping data had to be merged. We merge the files using the FTOOLS task fmerge as described on the MPE Cookbook page[1]. After this procedure the EPIC event lists were created in the standard way using the SAS version 5.3.0 (Science Analysis Software). We filtered further using HEAsoft[2] version 5.1 and 5.2. We used SAS version 5.3.3 to create the response matrices. Throughout, we used the "flag=0" events with the pattern of 0–4 and 0–12 from the PN and MOS detectors, respectively.

Figure 5.2 shows the resulting image from MOS1&MOS2. Along with the nucleus, there are two other prominent sources. Close inspection of the photon distribution also indicate a few other sources present. Photon counts for Source 1 are low, and other sources contain even fewer, so no analysis was performed on the fainter sources. Higher resolution observations from *Chandra* would be needed to identify the fainter sources in NGC 6300.

### 5.2.2 Optical Imaging Observation

We obtained optical data of NGC 6300 from the public HST archive. Four exposures were taken of the galaxy using the Wide Field Planetary Camera (WFPC2) on 4 July 2001. All exposures were 230 s in duration. Two exposures used the F450W filter and the remaining two used the F814W filter (Proposal 9042, PI Smartt). We also obtained an archived 500 s exposure that used the F606W filter observed on 2 April 1995 (Proposal 5479, PI Malkan).

The data was processed in the Interactive Reduction and Analysis Facility (IRAF) to

[1]http://wave.xray.mpe.mpg.de/xmm/cookbook/EPIC_PN/merge_odf.html

[2]http://heasarc.gsfc.nasa.gov/docs/software/lheasoft/

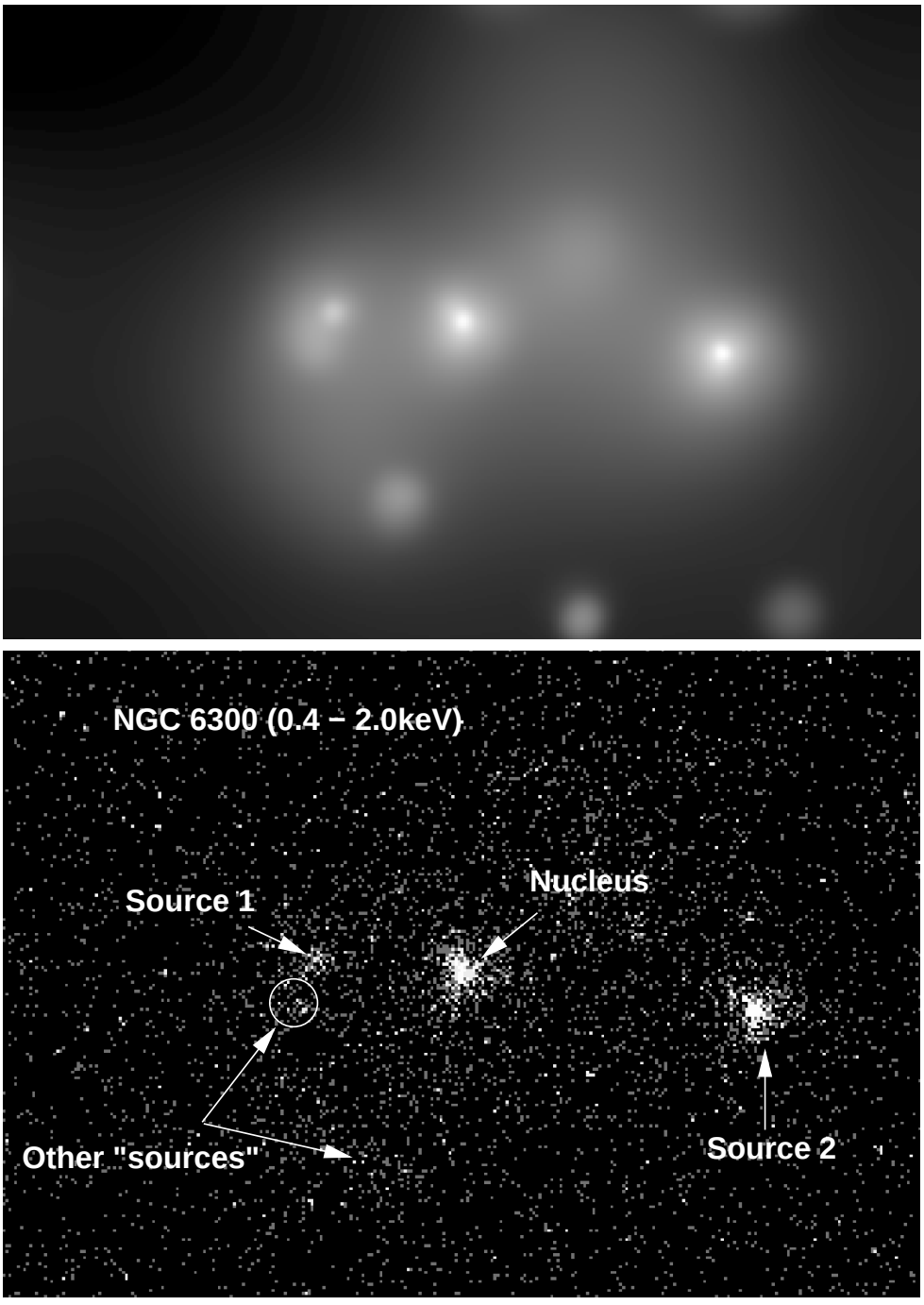



Figure 5.2 (*top*) Adaptively smoothed image ($1-2$ keV) of NGC 6300 showing three primary sources. (*bottom*) Raw image ($0.4-2$ keV) taken from MOS1 & MOS2 CCDs. The nucleus and two serendipitous sources are clearly indicated by arrows. Evidence in the raw photons indicate the presence of other faint sources along the ring structure. The faint sources near Source 1 are likely the origin of a "shelf" of emission seen in adaptively smoothed images of the galaxy.

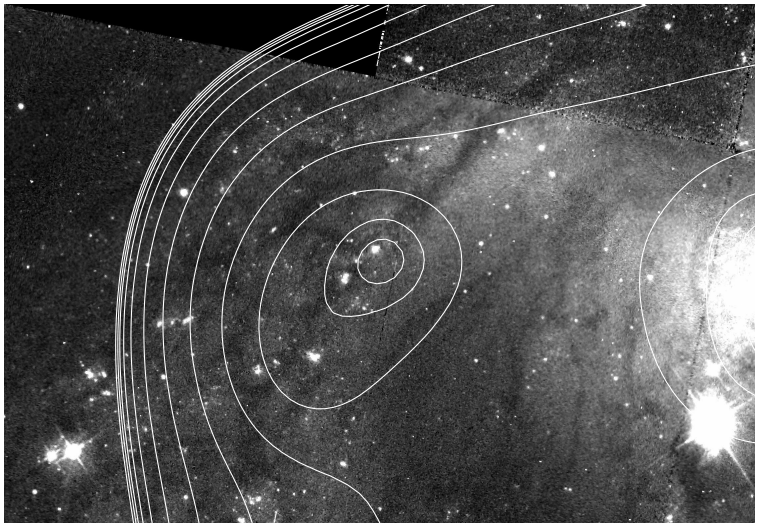


Figure 5.3 Closeup of HST field of NGC 6300. Contours are from a smoothed $1-2$ keV *XMM-Newton* image. Several star clusters are seen along a prominent dust lane.

remove cosmic ray events and to combine all four CCD images in to a mosaic image. Photometry on optical sources was determined using recipe in Gonzaga (2002).

### 5.2.3 Infrared Imaging Observation

Infrared observations were performed on 17 June, 2003 at the Anglo Australian Telescope using the IRIS2[3] detector. Images in the bands J (1.25$\mu$m), H (1.63$\mu$m) and $K_s$ (2.14$\mu$m) were produced. Several integrations were combined totaling $\sim$60s of exposure time in each band.

We performed aperture photometry measurements on several bright sources in the field to obtain instrumental magnitudes. Using the 2MASS Point Source Catalog (Cutri et al., 2003), transformation equations were determined for converting the instrumental magnitudes to the 2MASS standard magnitudes. We used the published fluxes for Vega (Cohen

[3]http://www.aao.gov.au/iris2/iris2.html

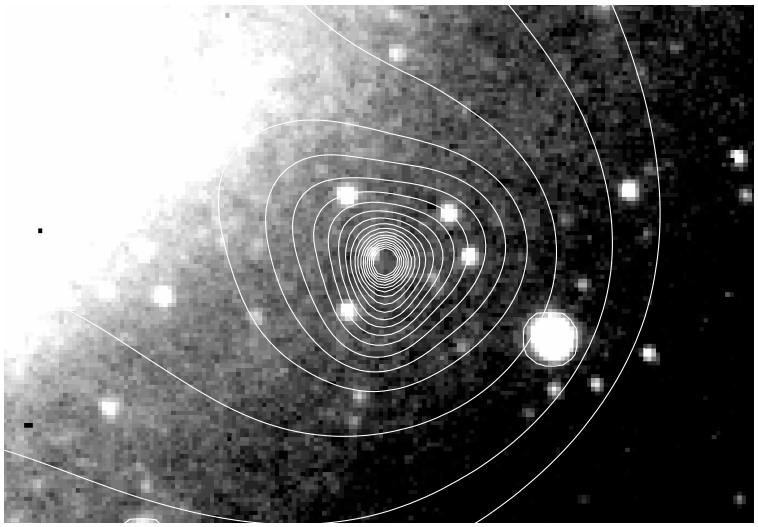


Figure 5.4 Closeup of area near Source 2. The background image is the H-band image from AAT. Contours are from a smoothed $1-2$ keV *XMM-Newton* image. There is a faint IR source just to the northeast of the center of the X-ray contours.

et al., 2003) to obtain energy fluxes.

### 5.2.4 Radio Observations

We obtained archived radio data of NGC 6300 from the ATCA[4]. The observations, described in Mazzolini & Webster (1996), were performed on 14-15 February 1994 in Configuration 6B (maximum baseline of 6km) and on 6 April 1995 in Configuration 6C (same maximum baseline as 6B, but inner telescopes having different positions). In each observation, data was taken simultaneously at 13cm and 20cm using a 33 channel continuum mode. Both observations used 1934-638 as a primary flux calibrator. A secondary calibrator, 1756-663, was observed in the 1994 observation, but was dropped after one scan in the 1995 observation. The good phase stability of 1934-638 during both observations make this of

[4]The Australia Telescope Compact Array is part of the Australia Telescope which is funded by the Commonwealth of Australia for operation as a National Facility managed by CSIRO.

little concern.

Initial processing of the data was done using the Astronomical Image Processing System (AIPS) equipped with a software patch provided by ATNF. Final editing and calibration was then performed using the Multichannel Image Reconstruction Image Analysis and Display (MIRIAD) software of ATNF. After calibration observations from different dates were combined to obtain a total of 24 hours of exposure time. This improved *uv* coverage and sensitivity. Imaging was performed in AIPS using the task MX. Of the original 33 channels, 14 channels from the central 75% of the bandwidth were used for calibration and imaging. We then produced a single channel continuum map for each central frequency using a multi-frequency synthesis algorithm.

Images were created using natural and uniform weighting. All results quoted are for uniform weighted maps unless otherwise noted. There is diffuse galaxy emission seen the the naturally weighted 20cm map due to the larger deconvolved beam. The emission is mostly 21cm neutral hydrogen as described in Ryder et al. (1996).

At 20cm a restoring beam of $7\farcs04 \times 6\farcs01$ with P.A. $-37.45°$ was used on the naturally weighted map. The noise level reached was 0.41 mJy[5]. This noise level is lower than that in Mazzolini & Webster (1996) due larger total exposure time. The uniformly weighted map used a restoring beam of twice the the area, leading to higher galaxy flux from HI emission.

At 13cm a restoring beam of $4\farcs15 \times 3\farcs55$ with P.A. $-34.08°$ was used. The noise level reached was 0.96 mJy.

[5] 1 Jansky = $10^{-21}$erg s$^{-1}$ cm$^{-2}$ Hz$^{-1}$

## 5.3 Multiwavelength Analysis

### 5.3.1 X-ray Spectral Analysis

#### Source 1

We began analysis of the non-nuclear emission with the source to the east of the nucleus. An unsmoothed image of the region indicate that there are at least two point sources that contribute to the X-rays in the $0.4 - 2$ keV energy range. In a smoothed image, this is manifested as a diffuse "shelf" of emission extending to the south of the peak source emission.

We extracted a spectra from a 16 arcsecond region in both the MOS1 and MOS2 CCDs. We the combined the two spectra to increase the total counts. In the end we obtained 306 total counts for source and background. The spectra were then grouped such that each energy bin contained at least 20 counts. We were unable to use the PN data as source 1 lies on a chip gap. If the source were not on the gap, the lower resolution of PN would cause the spectrum to be contaminated by other sources as well as the nucleus. Due to the uncertainty in the background level of the galaxy, we tried to bracket the parameters of the spectrum by extracting background spectra from several regions equidistant from the AGN[6] (Figure 5.5). After trying a few simple models, we obtained the best fits from a multicolor blackbody (*diskbb* in XSPEC) with added Galactic neutral hydrogen absorption. One of the fits is shown in Figure 5.6.

[6]The large point spread function (psf) at high energies mean that some photons from the nucleus will be present even at the position of source 1. Using equidistant backgrounds allows us to handle this extra contamination.

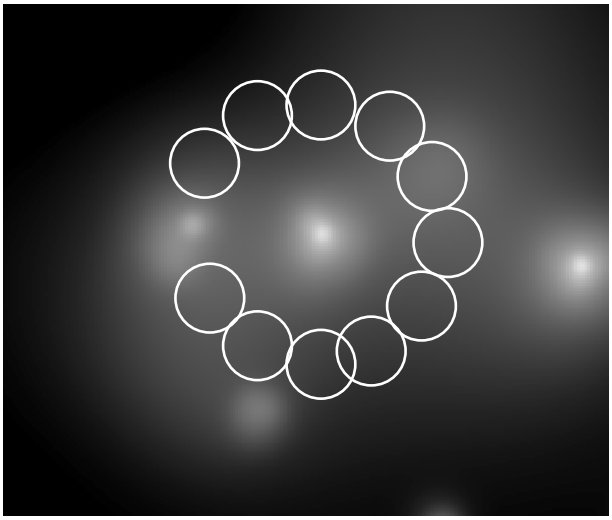


Figure 5.5 Smoothed *XMM-Newton* image of NGC 6300. Circles show the location of the background extraction regions used in the spectral analysis of the eastern point source.

The different backgrounds yielded a range of inner temperatures and luminosities for the accretion disk. The two backgrounds nearest the source yielded the extremes of this range. Using the background region to the south of the source yielded $T_{in} = 0.82^{+0.43}_{-0.25}$ keV, while the region to the north gave $T_{in} = 1.63^{+1.64}_{-0.60}$ keV. While this temperature range is consistent with the lower values for ULXs (Makishima et al., 2000), the luminosities calculated from these results fall short of the $10^{39}$ erg s$^{-1}$ minimum.

**Source 2**

For the source to the west of the nucleus, we extracted spectra from a 16 arcsecond region around the center. spectra were extracted from both MOS CCDs and the PN chip. The MOS spectra were combined and all spectra were grouped into bins such that each energy bin contained a minimum of 20 counts.

We then began fitting both spectra simultaneously using xspec. We began with simple

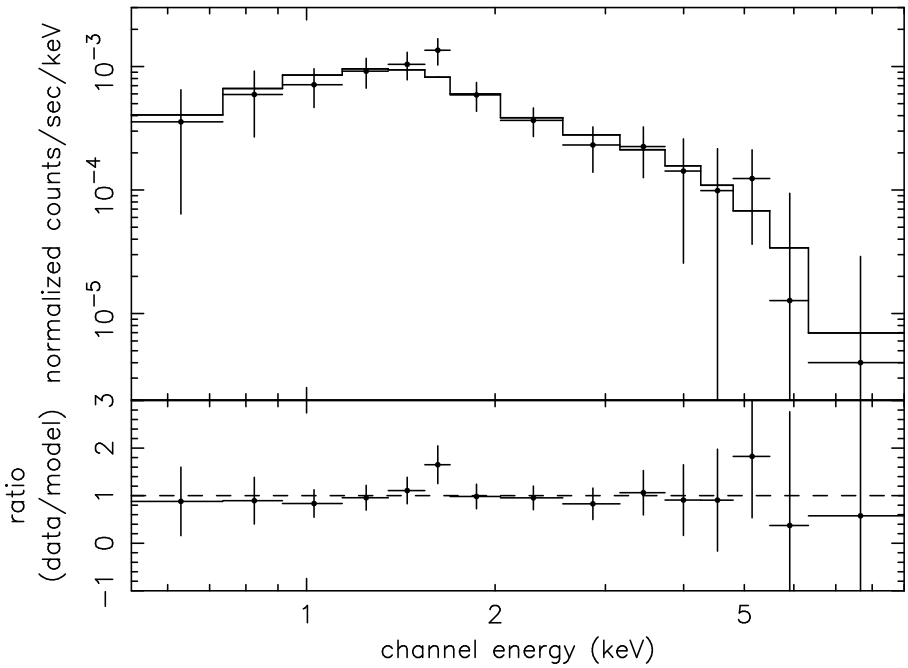



Figure 5.6 XMM spectrum of source 1. This spectrum utilized one of several background regions shown in Figure 5.5.

power law model. Although the $\chi^2$ value was good (70.91/92 dof), the model was high at the soft end of the spectrum. NGC 6300 is a very dusty galaxy, so it would stand to reason that there would be additional absorption due to the dust within the galaxy. We added another absorption component to the fit to see if there was an improvement in the fit (66.11/91 dof). We then tried the multicolor blackbody (*diskbb*). The fit was statistically worse than that of the powerlaw model. The results of all fits are tabulated in Table 5.1

### 5.3.2 Ultraviolet Analysis

Along with the X-ray data, we received data from the OM. After detecting the X-ray sources we began to look for UV counterparts. In the region around source 2, there is no detectable

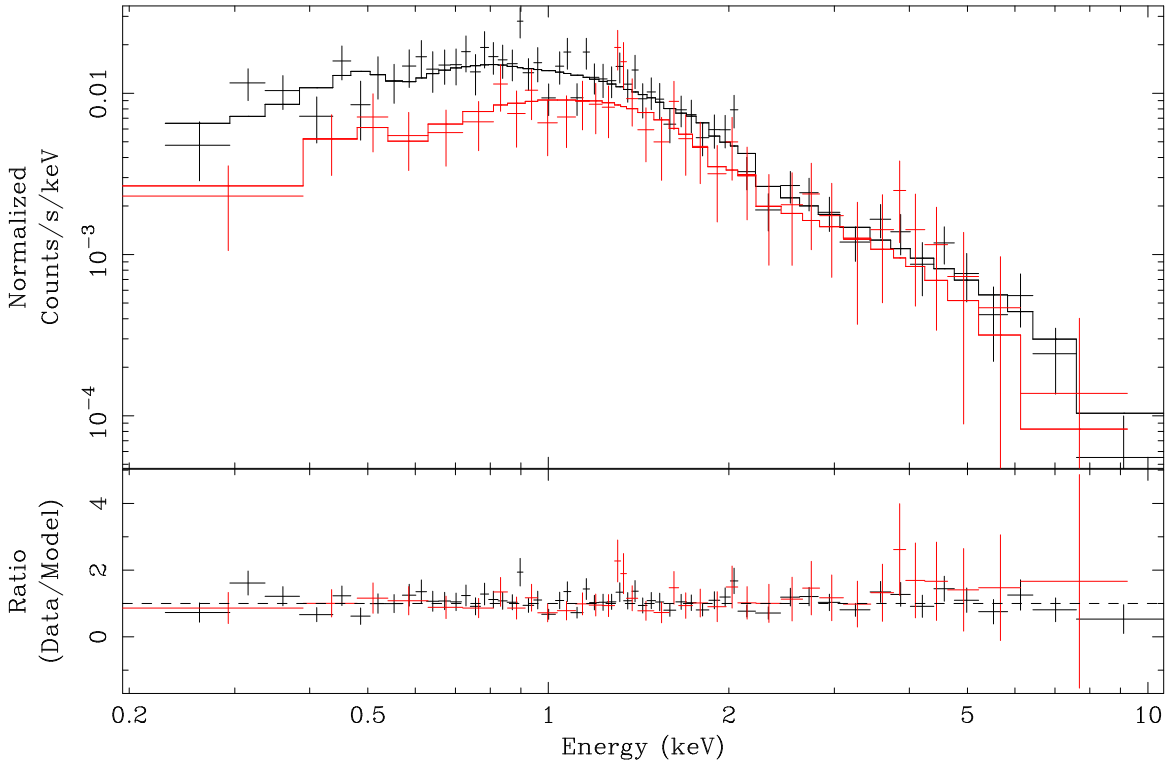



Figure 5.7 MOS ( *red*) and PN (*black*) spectra of Source 2. Solid lines denote model fits. Spectra are grouped such that there are 20 counts per bin.

Table 5.1 Model Fit Parameters for Sources 1 and 2

| Source | Model | $T_{in}$ (keV) | $\Gamma$ | $N_H$ ($10^{20}$ $cm^{-2}$) | $\chi^2$/d.o.f |
|---|---|---|---|---|---|
| 1 | PL | ··· | $1.30^{+0.32}_{-0.30}$ | ··· | 6.64/13 |
| | diskbb | $1.48^{+0.96}_{-0.47}$ | ··· | ··· | 4.09/13 |
| 2 | PL | ··· | $1.76^{+0.08}_{-0.07}$ | ··· | 70.91/92 |
| | PL+Abs. | ··· | $1.92^{+0.16}_{-0.14}$ | $4.26^{+3.69}_{-3.26}$ | 66.11/91 |
| | diskbb | $0.88^{+0.12}_{-0.10}$ | ··· | ··· | 123.3/92 |

source. Using the recipe for computing flux rates from OM count rates[7], we computed an upper limit of $1.07 \times 10^{-28}$ erg s$^{-1}$ cm$^{-2}$ Hz$^{-1}$ ($\nu = 1.03 \times 10^{15}$ Hz).

Although there appears to be a UV source near the position of source 1, the region is very confused, so at this time no UV measurements have been made.

### 5.3.3 Optical Analysis

For source 1, we had better prospects. Figure 5.3 shows the region around source 1. The overlayed X-ray contours indicate that several optical sources may contribute to the elongated shape of the emission. As noted previously, the extended shelf of X-ray emission is due to the presence of a few faint X-ray sources near source 1. The optical sources lie along a prominent dust lane that follows the ring.

We performed photometry on the source closest to the X-ray center of source 1. We obtained magnitudes of 17.94 and 17.63 in B and V, respectively. At the distance of NGC 6300, this yields absolute magnitudes $M_B = -13.41$ and $M_V = -13.63$.

While the WFPC2 field was large enough contain the ring of NGC 6300, it was not wide enough to extend to the region around source 2. For this reason we were unable to do any optical analysis on this source.

### 5.3.4 IR Analysis

After determining the flux scale for the IRIS2 observations, we turned our attention to searching for IR counterparts to sources 1 and 2. Figure 5.4 shows the region of NGC 6300 near source 2 in H-band. There is no apparent source at the peak of the X-ray emission.

[7] http://xmm.vilspa.esa.es/sas/documentation/watchout/uvflux.shtml

Table 5.2 IRIS2 Upper Limits and Fluxes for Region Around Source 2

| | | Upper Limit | Flux |
|---|---|---|---|
| Band | $\nu$ ($10^{14}$ Hz) | (erg s$^{-1}$ cm$^{-2}$ Hz$^{-1}$) | (erg s$^{-1}$ cm$^{-2}$ Hz$^{-1}$) |
| $K_s$ | 1.390 | $4.30 \times 10^{-27}$ | $1.24 \times 10^{-25}$ |
| $H$ | 1.783 | $5.00 \times 10^{-27}$ | $5.66 \times 10^{-26}$ |
| $J$ | 2.482 | $2.00 \times 10^{-27}$ | $2.63 \times 10^{-26}$ |

There is, however, a faint source $\sim 1\farcs2$ to the north and east of the center of source 2.

Due to uncertainties in the pointing of *XMM-Newton*, which can be as high as $2''$ (*XMM-Newton* User' Handbook[8]), we did photometry measurements on this source as well as setting upper limits on the flux for the likelihood that this was not a counterpart. The measured values are presented in Table 5.2.

We did not detect an IR counterpart to source 1. While several star clusters are visible in the HST image at the location of source 1, none of the clusters are bright in IR. For this reason, the upper limits calculated for source 2 are also applied to source 1.

### 5.3.5 Radio Analysis

Figure 5.8 shows the final ATCA images. The 20cm image, indicating extended galaxy emission, used natural weighting. To compare with the preliminary results of Mazzolini & Webster (1996), the peak nuclear flux density was measured using the AIPS task IMSTAT. For the uniformly weighted 20cm map, we measured a peak nuclear flux density of 10.8 mJy/Beam. This value is ∼3% higher than the reported peak in Mazzolini & Webster

[8]http://xmm.vilspa.esa.es/external/xmm_user_support/documentation/uhb_frame.shtml.

(1996), a difference that can be attributed to our slightly larger deconvolved beam. The 13cm peak was measured to be 5.49 mJy/Beam.

There are no radio sources within $4''$ of the *XMM-Newton* source positions. We must therefore estimate upper limits to the flux. Since the map noise levels are 0.14 mJy and 0.096 mJy at 20cm and 13cm, respectively, we place conservative $5\sigma$ upper limits of 0.70 mJy and 0.48 mJy on the radio flux density of these sources. These upper limits are plotted for source 2 (in energy units) in Figure 5.9.

## 5.4 Results

### 5.4.1 Source 1

With several spectral fits to source 1 pointing to a ULX-like nature, we wanted to see if it was a member of this class. As mentioned earlier, our fits produced a range of inner disk temperatures of $0.8-1.6$ keV, which are consistent with several ULXs studied by Makishima et al. (2000).

For the upper temperature bound, we get $0.2-10$ keV flux of $1.88\times10^{-14}$ erg s$^{-1}$ cm$^{-2}$. With a redshift $z = 0.0037$, this yields a luminosity in the same energy range of $L_{0.2-10\ \mathrm{keV}} = 5.37 \times 10^{38}$ erg s$^{-1}$ ($H_0 = 72$ km s$^{-1}$ Mpc$^{-1}$). At the lower temperature, the flux and luminosity are calculated to be $F_{0.2-10\ \mathrm{keV}} = 1.01 \times 10^{-14}$ erg s$^{-1}$ cm$^{-2}$, and $L_{0.2-10\ \mathrm{keV}} = 2.87 \times 10^{38}$ erg s$^{-1}$, respectively. These luminosities are below those of ULXs.

Optically, source 1 is located near several bright star clusters. Since these lie in the ring, they would be areas of high star formation. The lack of IR sources at the positions of the clusters suggests very blue emission that would be present in hot massive stars. As

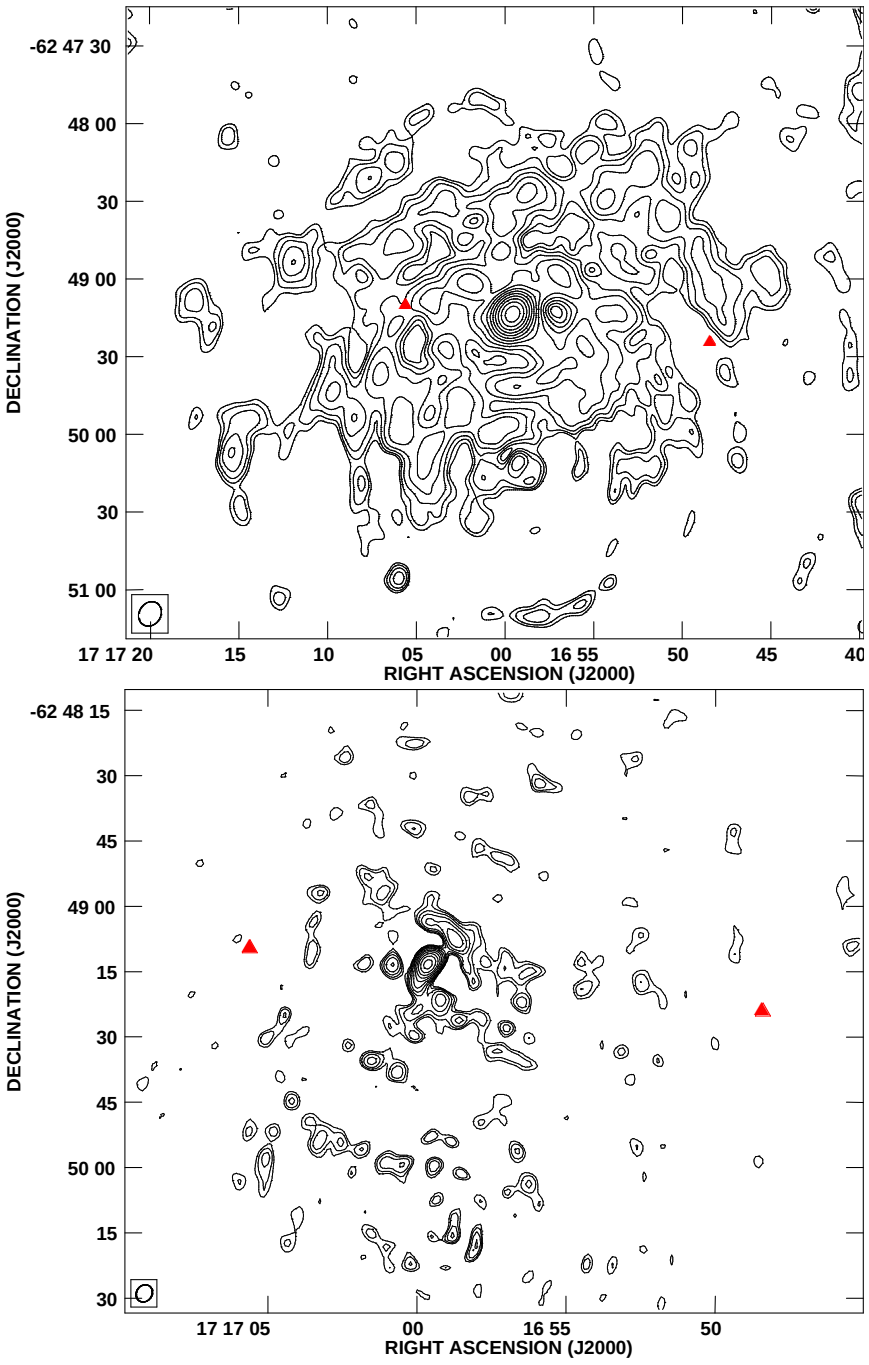



Figure 5.8 Radio contour maps of NGC 6300. The upper map shows 20cm emission and the lower shows 13cm emission. Contour levels are the multiple values (2.83, 4 5.66, 8, 11.31, 16, 22.63, 32, 45.25, 64, 90.51, 128, 181.0, and 256) of 0.05 mJy. Triangles show the position of the X-ray point sources. The size of the triangles reflect the 4.1″ resolution of *XMM-Newton*.

the most massive stars evolve, these areas would eventually produce XRBs. It looks as if source 1 is one of these binary systems.

### 5.4.2 Source 2

The higher photon count in source 2 made analysis somewhat easier than source 1. Our final model consisted of a power law with two absorption components. The first absorption component was due to Galactic column density ($9.38 \times 10^{20}$ cm$^{-2}$ in the direction of NGC 6300). The second was intrinsic absorption at the distance of NGC 6300. The derived intrinsic column was $4.26^{+3.68}_{-3.26} \times 10^{20}$ cm$^{-2}$. This value is consistent with the results of Ryder et al. (1996), as measured by 21 cm emission, for the region around source 2. Figure 5.7 shows the simultaneous fits for source 2. Our model flux in the $0.2 - 10$ keV band is $7.73 \times 10^{-14}$ erg s$^{-1}$ cm$^{-2}$ and the luminosity at the distance of NGC 6300 is $2.20 \times 10^{39}$ erg s$^{-1}$. If source 2 were in the galaxy this luminosity would classify it as a ULX.

The lack of counterparts seen in other wave bands leads us to postulate that source 2 is actually a background source that lies along the line of sight with NGC 6300. We do not detect line emission in the X-ray spectra so determining redshift is problematic. Using upper limits calculated from other wave bands, we have constructed a spectral energy distribution for source 2 (Figure 5.9). The proximity of the IR source in the IRIS2 data prompted us to include those points, though the flux measurements are much to high to be associated with the emission from source 2.

We had an idea that source 2 might be a BL Lac object. In order to test this we decided to compare the SED with those of confirmed BL Lacs. In a survey of BL Lac objects, Padovani & Giommi (1995) showed a bimodal distribution in the $\alpha_{ro}$-$\alpha_{ox}$ plane with the

break at $\alpha_{rx} = 0.75$. $\alpha_{ox}$ is the two-point power law index between 2500$\mathring{A}$ and 2 keV, assuming $f_\nu \propto \nu^{-\alpha_{ox}}$. Similarly, $\alpha_{ro}$ and $\alpha_{rx}$ are indices from 5 GHz to 2500$\mathring{A}$ and 5 GHz to 2 keV, respectively.

Since we were only able to determine upper limits on radio and UV fluxes, only a lower limit on $\alpha_{rx}$ can be established. From our data we were able to place a limit of $\alpha_{rx} \geq 0.81$. To compare with the distributions of BL Lacs, we plotted the limit on the $\alpha_{ro}$-$\alpha_{ox}$ plot of Padovani & Giommi (1995). Our object would within the distribution for X-ray selected BL Lacs. This is consistent with the fact that there is no definite radio detection for the source.

Foschini et al. (2002) recently reported the identification of a ULX in NGC 4698 with that of a background BL Lac. The spectral energy distribution (Figure 5.11) of this object is qualitatively similar to source 2, but the lack of detections at all other energies make a similar identification uncertain.

## 5.5 Conclusion and Future Work

We have presented multiwavelength analysis of two serendipitous X-ray sources from an *XMM-Newton* observation of NGC 6300. While no detections were made in radio, the combination of the other bands has given some insight as to the nature of the sources.

Source 1 had the same spectral shape and inner disk temperature as many ULXs. The luminosity range for the spectral fits eliminated this possibility. It is more likely an ordinary XRB. More detailed study is needed to verify this and to determine whether it is a HMXRB or LMXRB.

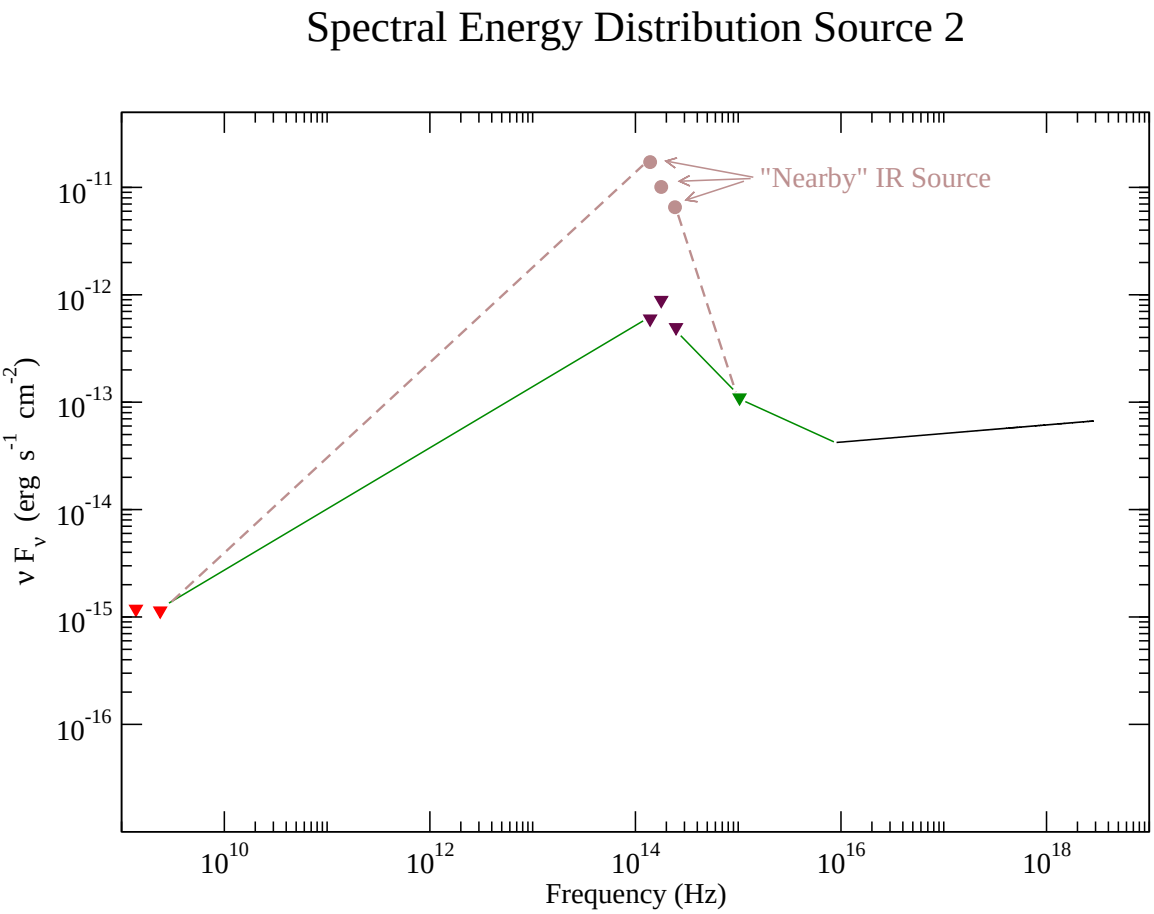



Figure 5.9 A constructed spectral energy distribution for Source 2. Triangles indicate measured upper flux limits. Red symbols are radio, maroon symbols are infrared points, green denotes OM point, and the black line denotes unabsorbed X-ray spectral model. Additionally, photometry points for a faint nearby IR source are shown. Colored lines have been added to guide the eye. The precipitous drop in the SED from the "nearby" IR source makes it highly unlikely that this source is associated with Source 2.

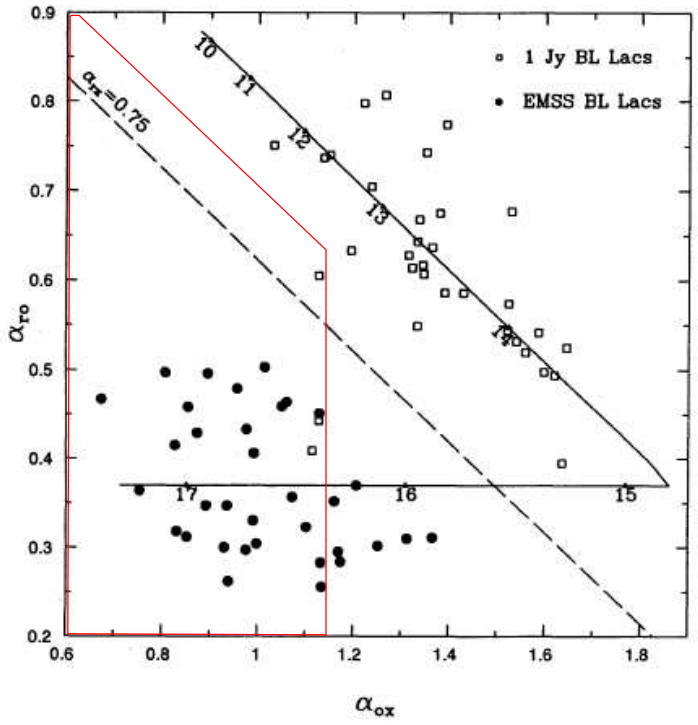



Figure 5.10 Distribution of BL Lac objects from Padovani & Giommi (1995). The shaded region denotes the range of $\alpha_{rx}$ for source 2.

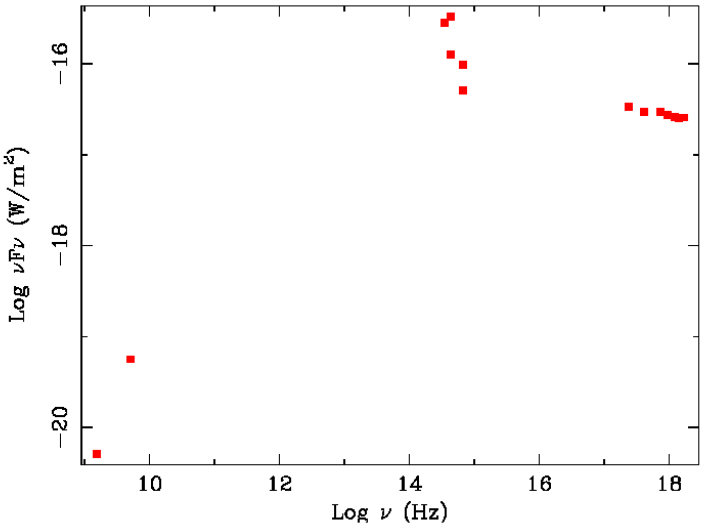



Figure 5.11 Observed spectral energy distribution of the ULX described in Foschini et al. (2002) (Figure 5). The object was identified as a $z = 0.43$ BL Lac object through optical spectra and observations at multiple frequencies.

Source 2 does fall into the category of a ULX if it lies at the distance of NGC 6300. Spectral fits and a lack of confirmed counterparts at other wavelengths suggest that it is a background object. The spectral energy distribution is consistent in shape with a BL Lac object, although to make such an identification would require at the least variability analysis. Rapid variability would all but rule out the BL Lac hypothesis. The presence of a faint IR source in the vicinity of source 2 may yet yield some kind of classification. Deeper optical observations at this position would also help.

More work must be done on this project. X-ray timing analysis must be done on both serendipitous sources to check for variability. The diffuse soft galaxy emission has yet to be approached. This requires modeling point sources at the positions of the nucleus and source 2 for subtraction. This may help to determine if the soft emission is confined to the ring or if it is constant throughout the galaxy.

Future *Chandra* observations will be proposed to resolve more point sources in order to compare the X-ray binary populations with more typical ringed, barred galaxies. High-mass XRBs should lag the onset of star formation by $\sim 10$ million years, the time required for the largest stars to evolve and die (e.g., Van Bever & Vanbeveren, 2000). The star clusters at the end of the ring may simply be too young to host many luminous XRBs. The difference in star formation may be a consequence of its peculiar geometry and dynamics. Thus *Chandra* may provide a sensitive probe of the evolution of star formation in this galaxy.

NGC 6300 is an excellent laboratory for the study of galaxy dynamics. The prodigious star formation and active nucleus provide insights into the evolution of this class of objects. Wider surveys of ringed, barred spiral galaxies may unlock more secrets to the evolution of spiral galaxies as a whole.

# Chapter 6

# Conclusions and Future Work

I have strived to present in this dissertation, the work that I have done on nearby spiral galaxies. To reiterate the primary conclusions reached in this work:

## 6.1 M83

• It was shown that SN 1957D has continued fading, consistent with an expanding shock through a circumstellar material that is decreasing in density. SN 1950B has apparently faded to the level of thermal HII regions that are near the position of the explosion. SN 1923A has faded to near the limits of detection of these observations. We continue to show no detection of SN 1983N after its initial radio detection, consistent with it having been a Type Ib supernova.

• About half of the radio sources are thermal HII regions, a result that is not surprising due to the high star formation activity of M83. The HII regions tend to be very large, exhibiting high excitation parameters. The largest regions are not detected due to the high resolution of our observations.

• It was found that ten sources were coincident with X-ray sources. The continuum spectral indices of these sources indicated that most were X-ray supernova remnants. We confirm that one of the coincident sources (source 28) is the nucleus of a background radio galaxy with two radio lobes (sources 27 and 29). Three of the X-ray sources are coincident with known optical supernova remnants.

• We note that the nuclear region of M83 has shown a slight increase in 20 cm emission in the radio peak. It is possible that there is an increase in accretion onto a supermassive black hole, which would be consistent with X-ray results. The 6 cm emission does not show this increase in flux. We confirmed that the reported optical/IR nuclear peak is not consistent with the radio nucleus, though there is evidence for a radio emission region at the position of the optical nucleus. It was seen that the nuclear radio peak was near the position of a second "dark" nuclear mass concentration that corresponds to the dynamical nucleus of the galaxy.

## 6.2 M51

• We detected emission from the Type Ic SN 1994I nearly a decade after explosion. We found the emission at this epoch to be consistent with light curve models for Type Ib/Ic supernovae. The SN was also detected in X-ray, though no optical counterpart was seen.

• Six of the associated H$\alpha$ sources are young SNRs with resolved shells. Most exhibit steep continuum radio spectra consistent with synchrotron emission. Based on a Cas A expansion velocity, we estimated the age of the SNRs to be $\sim 2000 - 3300$ yr.

• Thirteen radio sources have X-ray counterparts. Eight of the 13 sources have SNR-like X-ray spectra. Two of these X-ray/radio sources are coincident with resolved H$\alpha$ shells. Two of the remaining sources are highly absorbed. Source 12 is likely a background AGN, while Source 95, though there is no optical counterpart, could be a dust-embedded SNR or XRB.

• The result of our analysis of the nuclear region, including the XNC, bubble and nucleus, are consistent with previous studies that suggest a bipolar radio jet from the low luminosity

Seyfert 2 nucleus. The nucleus and XNC have identical continuum spectra, indicative of shock heated gas interacting with the jet.

## 6.3 M101 and NGC 3184

We detected 28 radio point sources in M101. Most lie along the spiral structure. None of the historical supernovae were detected as they lie outside the field of view.

Ten radio point sources were detected in NGC 3184. These include one confirmed background source. No supernova emission was detected in this galaxy.

X-ray analysis of both galaxies will be performed at a later time.

## 6.4 NGC 6300

The work performed on NGC 6300 yielded some insight in the nature of two non-nuclear X-ray point sources:

• Source 1 had the same spectral shape and inner disk temperature as many ULXs. The luminosity range for the spectral fits eliminated this possibility. It is more likely an ordinary XRB. More detailed study is needed to verify this and to determine whether it is a HMXRB or LMXRB.

• Source 2 does fall into the category of a ULX if it lies at the distance of NGC 6300. Spectral fits and a lack of confirmed counterparts at other wavelengths suggest that it is a background object. The spectral energy distribution is consistent in shape with a BL Lac object, although to make such an identification would require at the least variability analysis. Rapid variability would all but rule out the BL Lac hypothesis. The presence of a

faint IR source in the vicinity of source 2 may yet yield some kind of classification. Deeper optical observations at this position would also help.

## 6.5 General Conclusions

Our compact radio sources tend to be associated with large regions of ionized hydrogen. This is not a surprising result as many of the galaxies that are presented here are active star forming systems (with the possible exception of NGC 3184). The vast difference between the number of sources detected is largely a matter of distance to the observed objects coupled with the depth of the observations. M83 was resolution limited to $\sim 3''$. The remaining galaxies each had resolution on the order of $1''$. Most of the radio observations reached a luminosity depth of $10^{-24}$ erg s$^{-1}$ Hz$^{-1}$. NGC 3184 observations were not as deep by about one order of magnitude.

The majority of the radio sources with coincident X-ray emission are SNRs and background AGNs. This has been the case for many similar studies. The primary reason for this phenomenon is the emission mechanisms for each class of objects. For SNRs, X-ray emission arises due the shock-heated thermal plasma, and the radio arises to synchrotron emission in the expanding shock wave. The SNRs that do not exhibit both forms of emission are likely at different evolutionary stages of development.

For AGNs, X-ray emission is believed to arise from inverse compton scattering of photons off of the high energy electrons in the small region around the central engine. This region is likely the innermost area of the accretion disk. Radio emission can come from a variety a places within the AGN, but the primary mechanism is again synchrotron, though there can be some free-free interactions that contribute. Detailed modeling of the continuum

spectrum of radio sources tend to agree with this supposition.

What is presented here, and will be published in journals in the future, will be a rich catalog of radio properties that will be useful in multiwavelength studies of these and other nearby galaxies.

## 6.6 Future Work

There are still some tasks that must be performed to complete the work presented in this dissertation. I must finish the analysis of the diffuse galaxy emission in NGC 6300. This will involve modeling the nucleus and point sources to subtract their contribution to the galaxy emission. The background level needs to be carefully selected to determine if the diffuse X-ray emission is confined to the ring, or is present throughout the galaxy.

The presentation of the M101 and NGC 3184 data must be completed. A similar comparison to other wavelengths is planned, but time did not allow for that to be completed for this presentation. In the future, I believe that new instruments, discussed briefly below, will give us the sensitivity to give NGC 3184 a deeper look. Other than targeted looks for supernovae, there have been no deep observations of the galaxy as a whole. The sources contained in the galaxy will be extremely faint, but with new receivers and longer exposures, we should be able to detect some of them.

I will also be working on analyzing the nuclear emission of M83 at VLBI resolution. In collaboration with Steven Tingay, I was PI on a LBA proposal that was approved to observe M83 for the first time using a VLBI array. The observations have been performed and I am awaiting the final image. This high-resolution look into the nucleus will allow us to isolate individual radio sources in a previously unresolved area of emission. There are many X-ray

sources located in the nucleus, and we now have the ability to check for radio counterparts to that emission. If our results look promising, there is a chance we could receive future observations at multiple frequencies to probe the nature of these bright nuclear sources.

I would also like to expand my sample of galaxies to include up to ten more, all included in a mini-survey of nearby spirals observed by *Chandra*. The full X-ray catalog of sources has been presented in Kilgard et al. (2005). With Roy Kilgard, I was involved in the preparation of an archival HST proposal to get optical data for the galaxies in this sample. The goal is to characterize as fully as possible the full spectrum characteristics of compact X-ray sources.

I was also co-I on a proposal with Bill Blair and Knox Long for a deep multi-pointing HST observation of M83. The goal of this project is to determine the population of young SNRs in this active star-forming galaxy.

As for future employment, that chapter has not yet been written. I have several applications to a variety of open positions. I have been offered an interview at the Harvard-Smithsonian Center for Astrophysics to do work in X-ray SNR studies with Terry Gaetz and Paul Plucinsky. The interview is scheduled for late August.

If the CfA job does not happen, I intend to enter a proposal to the National Research Council in February to work in the Radio Astronomy Division of the Naval Research Laboratory. I am in contact with Namir Kassim to propose a extension of the work that I have done in my doctoral work to the long wavelength bands. Using the low frequency capabilities of the VLA and VLBA, I intend to propose morphological studies of spiral galaxies. With the resolutions achievable with the VLBA, I can pursue a study of nuclear outflows in M51 and M101. The outflows in M51 have been known for some time, but

only recently have optical observations given evidence for bipolar outflows in M101. The generally higher luminosity of the radio sources at low frequency, coupled with the high resolutions obtainable with modern instruments, make this an excellent area of study.

## 6.7 Future Prospects in Radio Astronomy

With the current development and construction of new interferometer arrays, astronomers will soon have many unprecedented opportunities to study the universe in radio bands. The Submillimeter Array (SMA) and the Combined Array for Millimeter wave Astronomy (CARMA) are online now, and are producing results. The Atacama Large Millimeter Array (ALMA) is in construction. With is maximum baseline of 10 km and 64 12-meter antennas, ALMA will provide the highest resolution and highest sensitivity that has been achieved to date in the 350 $\mu$m and 10 mm bands.

The VLA is receiving a major upgrade, including new, more sensitive receivers, a new correlator and the addition of eight dishes spread out to a maximum baseline of 350 km. The result will be an order of magnitude improvement in resolution and sensitivity.

Two new low-frequency interferometers are also in development: the Low Frequency Array (LOFAR) in Europe and the Long Wavelength Array in the United States. When completed, these instruments will provide astronomers with access to the last under observed window that can be observed from the ground.

Finally, the Square Kilometer Array (SKA) is in the earliest phases of planning. This instrument will provide the highest sensitivity in the radio bands that has ever been achieved. It will combine multi-beam capabilities with VLBI resolution capability.

Advancements in computer speed and storage capabilities will allow each of these in-

struments to have nearly continuous spectral coverage over their designed frequency ranges, giving us even more information about the objects we will be studying. The challenge is to develop new imaging algorithms that allow for parallelization and exploiting supercomputer technology. Without these new techniques, the processing time for the data sets would be prohibitive.

# Bibliography


Awaki, H., Murakami, H., Leighly, K. M., Matsumoto, C., Hayashida, K., & Grupe, D. 2005, ApJ, 632, 793

Baron, E., Hauschildt, P. H., Branch, D., Kirshner, R. P., & Filippenko, A. V. 1996, MNRAS, 279, 799

Berezhko, E. G., & Völk, H. J. 2004, A&A, 427, 525

Blair, W. P., & Long, K. S. 2004, ApJS, 155, 101

Boffi, F. R., Sparks, W. B., & Macchetto, F. D. 1999, A&AS, 138, 253

Buta, R. 1987, ApJS, 64, 383

—. 1995, ApJS, 96, 39

—. 1999, Ap&SS, 269, 79

Buta, R., Crocker, D. A., & Byrd, G. G. 1999, AJ, 118, 2071

Buta, R. J. 1984, Ph.D. Thesis

Calzetti, D., et al. 2005, ApJ, 633, 871

Cecil, G. 1988, ApJ, 329, 38

Chevalier, R. A. 2006, ArXiv Astrophysics e-prints

Cohen, M., Wheaton, W. A., & Megeath, S. T. 2003, AJ, 126, 1090

Colbert, E. J. M., Heckman, T. M., Ptak, A. F., Strickland, D. K., & Weaver, K. A. 2004, ApJ, 602, 231

Cowan, J. J., & Branch, D. 1982, ApJ, 258, 31

—. 1985, ApJ, 293, 400

Cowan, J. J., Roberts, D. A., & Branch, D. 1994, ApJ, 434, 128

Crane, P. C., & van der Hulst, J. M. 1992, AJ, 103, 1146

Crocker, D. A., Baugus, P. D., & Buta, R. 1996, ApJS, 105, 353

Cutri, R. M., et al. 2003, VizieR Online Data Catalog, 2246, 0

de Vaucouleurs, G. 1956, *Mem. Com. Mt. Stromlo*, 3, 13

—. 1979a, AJ, 84, 1270

—. 1979b, ApJ, 227, 729

de Vaucouleurs, G., Pence, W. D., & Davoust, E. 1983, ApJS, 53, 17

Dickey, J. M., & Lockman, F. J. 1990, ARA&A, 28, 215

Eck, C. R., Cowan, J. J., & Branch, D. 2002, ApJ, 573, 306

Eck, C. R., Roberts, D. A., Cowan, J. J., & Branch, D. 1998, ApJ, 508, 664

Elmegreen, D. M., Chromey, F. R., & Warren, A. R. 1998, AJ, 116, 2834

Fabbiano, G. 2004, in Revista Mexicana de Astronomia y Astrofisica Conference Series, 46–49

Feldmeier, J. J., Ciardullo, R., & Jacoby, G. H. 1997, ApJ, 479, 231

Ford, H. C., Crane, P. C., Jacoby, G. H., Lawrie, D. G., & van der Hulst, J. M. 1985, ApJ, 293, 132

Foschini, L., Ho, L. C., Masetti, N., Cappi, M., Dadina, M., Bassani, L., Malaguti, G., Palazzi, E., Di Cocco, G., Martini, P., Ravindranath, S., Stephen, J. B., Trifoglio, M., & Gianotti, F. 2002, A&A, 396, 787

Freedman, W. L., Madore, B. F., Gibson, B. K., Ferrarese, L., Kelson, D. D., Sakai, S., Mould, J. R., Kennicutt, Jr., R. C., Ford, H. C., Graham, J. A., Huchra, J. P., Hughes, S. M. G., Illingworth, G. D., Macri, L. M., & Stetson, P. B. 2001, ApJ, 553, 47

Gonzaga, S. 2002, WFPC2 Data Analysis: A Tutoral (Baltimore, STSCI)

Gopal-Krishna, & Irwin, J. A. 2000, A&A, 361, 888

Hjellming, R. M. 1982, NEWSLETTER. NRAO NO. 4, P. 5, 1982, 4, 5

Immler, S., Wilson, A. S., & Terashima, Y. 2002, ApJ, 573, L27

Jenkins, L. P., Roberts, T. P., Warwick, R. S., Kilgard, R. E., & Ward, M. J. 2004, MNRAS, 349, 404

Kennicutt, Jr., R. C., Armus, L., Bendo, G., Calzetti, D., Dale, D. A., Draine, B. T., Engelbracht, C. W., Gordon, K. D., Grauer, A. D., Helou, G., Hollenbach, D. J., Jarrett, T. H., Kewley, L. J., Leitherer, C., Li, A., Malhotra, S., Regan, M. W., Rieke, G. H., Rieke, M. J., Roussel, H., Smith, J.-D. T., Thornley, M. D., & Walter, F. 2003, PASP, 115, 928

Kilgard, R. E., Cowan, J. J., Garcia, M. R., Kaaret, P., Krauss, M. I., McDowell, J. C., Prestwich, A. H., Primini, F. A., Stockdale, C. J., Trinchieri, G., Ward, M. J., & Zezas, A. 2005, ApJS, 159, 214

Kilgard, R. E., Kaaret, P., Krauss, M. I., Prestwich, A. H., Raley, M. T., & Zezas, A. 2002, ApJ, 573, 138

Kilgard, R. E., Prestwich, A. H., Ward, M. J., & Roberts, T. P. 2006, in IAU Symposium, ed. E. J. A. Meurs & G. Fabbiano, 189–192

Kloehr, W., Muendlein, R., Li, W., Yamaoka, H., & Itagaki, K. 2005, IAU Circ., 8553, 1

Kowal, C. T., & Sargent, W. L. W. 1971, AJ, 76, 756

Kuntz, K. D., Snowden, S. L., Pence, W. D., & Mukai, K. 2003, ApJ, 588, 264

Leonard, D. C., Filippenko, A. V., Li, W., Matheson, T., Kirshner, R. P., Chornock, R., Van Dyk, S. D., Berlind, P., Calkins, M. L., Challis, P. M., Garnavich, P. M., Jha, S., & Mahdavi, A. 2002, AJ, 124, 2490

Lewin, W. H. G., van Paradijs, J., & Van Den Heuvel, E. P. J., eds. 1995, X-ray Binaries

Long, K. S., Blair, W. P., & Krzeminski, W. 1989, ApJ, 340, L25

Long, K. S., Winkler, P. F., & Blair, W. P. 1992, ApJ, 395, 632

Longair, M. S. 1994, High energy astrophysics. Vol.2: Stars, the galaxy and the interstellar medium (Cambridge: Cambridge University Press, —c1994, 2nd ed.)

Maddox, L. A., Cowan, J. J., Kilgard, R. E., Lacey, C. K., Prestwich, A. H., Stockdale, C. J., & Wolfing, E. 2006, AJ, 132, 310

Maddox, L. A., Stockdale, C. J., & Cowan, J. J. 2003, American Astronomical Society Meeting, 203,

Makishima, K., Kubota, A., Mizuno, T., Ohnishi, T., Tashiro, M., Aruga, Y., Asai, K., Dotani, T., Mitsuda, K., Ueda, Y., Uno, S., Yamaoka, K., Ebisawa, K., Kohmura, Y., & Okada, K. 2000, ApJ, 535, 632

Mast, D., Díaz, R. J., & Aguero, M. P. 2005, ArXiv Astrophysics e-prints

Mathewson, D. S., & Ford, V. L. 1996, ApJS, 107, 97

Matsumoto, C., Nava, A., Maddox, L. A., Leighly, K. M., Grupe, D., Awaki, H., & Ueno, S. 2004, ApJ in press

Mazzolini, M., & Webster, R. 1996, Publications of the Astronomical Society of Australia, 13, 107

Mezger, P. G., & Henderson, A. P. 1967, ApJ, 147, 471

Moody, J. W., Roming, P. W. A., Joner, M. D., Hintz, E. G., Geisler, D., Durrell, P. R., Scowen, P. A., & Jee, R. O. 1995, AJ, 110, 2088

Nipoti, C., Blundell, K. M., & Binney, J. 2005, MNRAS, 361, 633

Padovani, P., & Giommi, P. 1995, ApJ, 444, 567

Pannuti, T. G., Duric, N., Lacey, C. K., Ferguson, A. M. N., Magnor, M. A., & Mendelowitz, C. 2002, ApJ, 565, 966

Pierce, M. J. 1994, ApJ, 430, 53

Prestwich, A. H., Irwin, J. A., Kilgard, R. E., Krauss, M. I., Zezas, A., Primini, F., Kaaret, P., & Boroson, B. 2003, ApJ, 595, 719

Puckett, T., et al. 1994, IAU Circ., 5961, 1

Reber, G. 1944, ApJ, 100, 279

Reynolds, J. H. 1921, MNRAS, 81, 598

Rots, A. H., Bosma, A., van der Hulst, J. M., Athanassoula, E., & Crane, P. C. 1990, AJ, 100, 387

Rudnick, L. 1982, in IAU Symp. 97: Extragalactic Radio Sources, ed. D. S. Heeschen & C. M. Wade, 47–49

Rumstay, K. S., & Kaufman, M. 1983, ApJ, 274, 611

Ryder, S. D., Buta, R. J., Toledo, H., Shukla, H., Staveley-Smith, L., & Walsh, W. 1996, ApJ, 460, 665

Sakamoto, K., Matsushita, S., Peck, A. B., Wiedner, M. C., & Iono, D. 2004, ApJ, 616, L59

Sandage, A. 1978, AJ, 83, 904

Sandage, A., & Tammann, G. A. 1974, ApJ, 194, 559

—. 1987, A revised Shapley-Ames Catalog of bright galaxies (Carnegie Institution of Washington Publication, Washington: Carnegie Institution, 1987 , 2nd ed.)

Schraml, J., & Mezger, P. G. 1969, ApJ, 156, 269

Scowen, P. A., Dufour, R. J., & Hester, J. J. 1992, AJ, 104, 92

Soria, R., Cropper, M., & Motch, C. 2004, ArXiv Astrophysics e-prints, astro-ph/0409130

Soria, R., & Wu, K. 2002, A&A, 384, 99

—. 2003, A&A, 410, 53

Stockdale, C. J., Cowan, J. J., Maddox, L. A., Lacey, C. K., Rupen, M. P., Prestwich, A. H., Kilgard, R., Krauss, M. I., & Zezas, A. 2001a, Bulletin of the American Astronomical Society, 33, 1338

Stockdale, C. J., Goss, W. M., Cowan, J. J., & Sramek, R. A. 2001b, ApJ, 559, L139

Stockdale, C. J., Kelley, M., van Dyk, S. D., Sramek, R. A., Weiler, K. W., & Panagia, N. 2005a, IAU Circ., 8603, 2

Stockdale, C. J., Maddox, L. A., Cowan, J. J., Prestwich, A., Kilgard, R., & Immler, S. 2006, AJ, 131, 889

Stockdale, C. J., Sramek, R. A., Weiler, K. W., Van Dyke, S. D., Pangia, N., Montes, M. J., & Rupen, M. P. 2005b, in IAU Colloq. 192: Cosmic Explosions, On the 10th Anniversary of SN1993J, ed. J.-M. Marcaide & K. W. Weiler, poster presentation

Strüder, L., et al. 2001, A&A, 365, L18

Talbot, R. J., Jensen, E. B., & Dufour, R. J. 1979, ApJ, 229, 91

Terashima, Y., & Wilson, A. S. 2001, ApJ, 560, 139

Thatte, N., Tecza, M., & Genzel, R. 2000, A&A, 364, L47

Thim, F., Tammann, G. A., Saha, A., Dolphin, A., Sandage, A., Tolstoy, E., & Labhardt, L. 2003, ApJ, 590, 256

Tingay, S. J. 2004, AJ, 127, 10

Turner, M. J. L., et al. 2001, A&A, 365, L27

Van Bever, J., & Vanbeveren, D. 2000, A&A, 358, 462

van de Hulst, H. C. 1951, AJ, 56, 144

Walter, F., Brinks, E., de Blok, E., Bigiel, F., Thornley, M., & Kennicutt, R. C. 2005, American Astronomical Society Meeting Abstracts, 207, #64.09

Weiler, K. W., Panagia, N., Montes, M. J., & Sramek, R. A. 2002, ARA&A, 40, 387

Weiler, K. W., Sramek, R. A., Panagia, N., van der Hulst, J. M., & Salvati, M. 1986, ApJ, 301, 790

Zaritsky, D., Hill, J. M., & Elston, R. 1990, AJ, 99, 1108

# Appendix A

# The Very Large Array and the Processing Radio Interferometry Observations

## A.1 The VLA

The Very Large Array is an aperture synthesis radio telescope with a resolving power similar most ground-based optical telescopes. The VLA is able to observe the entire northern sky and has a limited capability to observe some southern objects (Declination $> -30$ deg). For sources below this declination, observations have limited resolution. The VLA consists of 27 individual antennae, with diameters of 25 m, arranged in a large "Y" pattern (9 antennae per arm). The antennae are linked together electronically and, in the largest configuration, have a resolving power equivalent to a telescope with a diameter of 36 km with sensitivity of a 130 m telescope.

The principles by which the 27 single elements of the VLA are able to act as one large receiver are interferometry and aperture synthesis. A pair of antennae with cross-correlated signals observing the same source is called an interferometer. With the 27 antennae of the VLA, there are 351 pairs of interferometers with different baseline spacings (antenna separation). The cross-correlation of the signals from each baseline pair provides information about the intensities of each source in the beams of the antennae and their positions in the sky relative to the pointing of the baseline pairs. In order to make sense of this information, it becomes essential to accurately measure the time delays and location of each antenna

(Hjellming, 1982). The distribution of radio emission in an antenna beam can be considered as the superposition of many components of varying size, position and orientation. One can describe the relation between intensity distributions and individual components in terms of a Fourier integral relationship, where baseline pair measures a single Fourier component of the apparent angular distribution of the sources in the antenna beam. Many such components are needed to reconstruct a spatially-accurate image of the sources. These are "provided" by the Earth's rotation, as the geometric configuration between the antennae on the Earth and the source in the sky are constantly changing, i.e. aperture synthesis (Hjellming, 1982).

The VLA has four main configurations: A (0.68 km $\leq b \leq$ 36.4 km), B (0.21 km $\leq b \leq$ 11.4 km), C (0.035 km $\leq b \leq$ 3.4 km), and D (0.035 km $\leq b \leq$ 1.03 km) The antennae are moved by a large loader on railroad tracks to specific concrete pads for each configuration. Each configuration is specifically designed to provide optimal resolution at different wavelengths, ( beginning with the A-configuration) 20 cm, 6 cm, 2 cm, and 1.3 cm. Each array configuration provides comparable resolution with its primary observing wavelength due to its relationship between observed wavelength and the distances between each baseline pair of antennae.

Because the geometry of each array is very well known, it is possible to determine the precise time delay ($\sim$ 0.5 pico-seconds for 1.5 cm) between signals received at each antenna in a baseline pair as a function of the pointing direction for the array. This delay be can be as large as 125 $\mu$s for the longest baselines in the A configuration (Hjellming, 1982). Figure A.1 illustrates the basic concept of the delay time as function of the geometry between a baseline pair of antennae. Because the required timing accuracy of 0.5 ps is too difficult to achieve, the raw radio frequency (RF) signals are mixed with a local oscillator signal and

then converted into intermediate frequencies (IFs) which convey the phase and amplitude information from the raw signal. The signal from the "closer" antenna is then delayed by the appropriate time factor to insure proper phase coherence, and now the information from each baseline pair can be cross-correlated (multiplied and filtered). Because of the range in time delays for each baseline pair and the number of baselines in the VLA, it is extremely complicated (although by no means impossible) to convert the incoming signals into measurements of the amplitude and phase of the incoming wavefront. Hjellming (1982) provides a detailed discussion of the processes involved in converting the raw data into a more useful format. The VLA antennae also have two feeds of orthogonal polarizations for each frequency which are normally circular (right and left) but can also be converted to linear polarization with the insertion of linear polarizers. Most observations only use right-right (R-R) and left-left (L-L) polarizations, but it is useful to request cross polarization be applied to observations if interested in whether the emission is polarized and to what extent. The observations discussed in the dissertation do not include such measurements, as the sources were all very faint and do not produce sufficient emission for useful polarization studies. Typical VLA continuum observations are centered on two IFs separated by 100 MHz about the central wavelength with band passes of 50 MHz, with R-R and L-L polarizations for each IF.

## A.2 Processing VLA Data

The purpose of this section is to sketch out the steps required to calibrate and a continuum observation from the VLA. Where necessary, I will include entries from the history of a

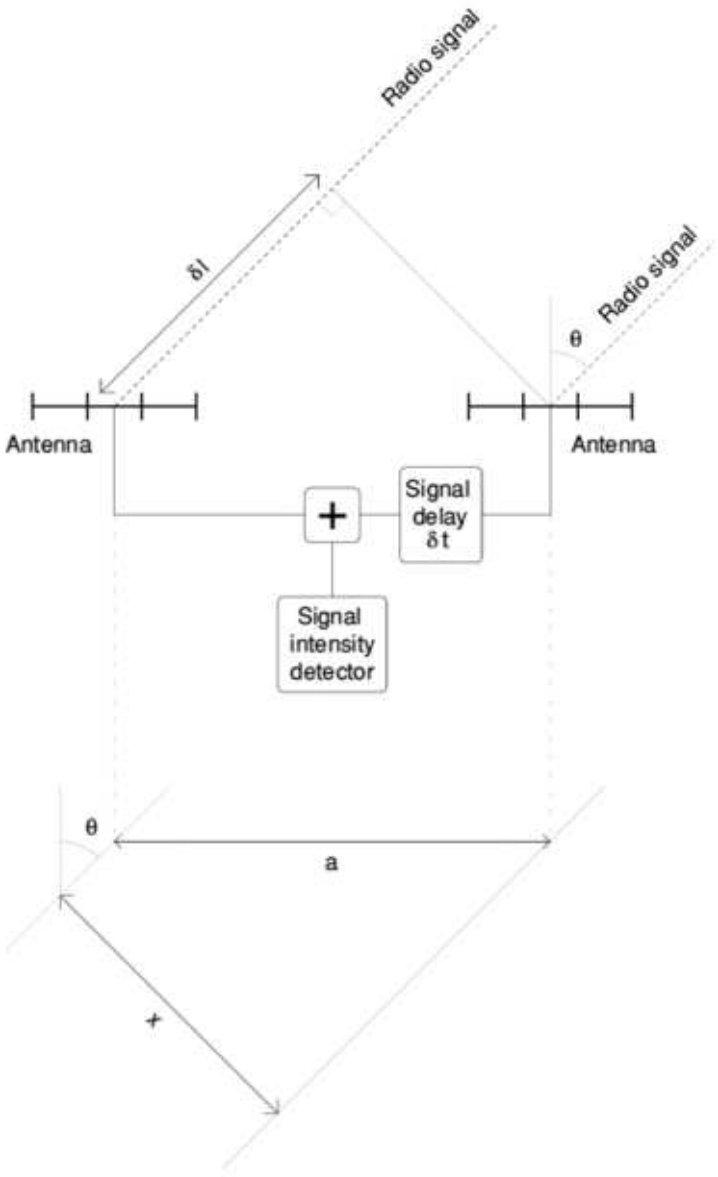



Figure A.1 Schematic of a basic two dish radio interferometer. a is the antenna separation, $\delta l$ denotes the path difference the wavefront travels between receivers.

processed data set. What needs to be kept in mind is that the process will not work for all data sets. Spectral line sets and observations from other telescopes (like the Australia Telescope Compact Array) will require different tasks and techniques. There are resources online, freely available from the observatories, that will assist in the processing of these observations. I have additionally provided Dr. Cowan with the primary documentation references for AIPS and MIRIAD (Multi-channel Image Reconstruction Image Analysis and Display). With the MIRIAD documentation, I have a guide to reducing ATCA data in AIPS (provided by Neil Killeen of ATNF). For detailed information on individual AIPS tasks, you may use the verbs HELP and EXPLAIN within an AIPS session.

Once the observations have been taken and the correlated data have been obtained (the observer received instructions on how to retrieve the files from the VLA), the data must be converted into a format that can be manipulated. The software suite that is used throughout is the Astronomical Image Processing System (AIPS).

The task that is used for reading unprocessed data into the system is called FILLM. The inputs are straight forward, and the task is easy to call. An example of a FILLM input setup is as follows:

```
>tget FILLM
>inp
AIPS 1: FILLM     Task to read a VLA archive tape
AIPS 1: Adverbs     Values                Comments
AIPS 1: ------------------------------------------------------------
AIPS 1: INTAPE        1                   Tape drive number
```

```
AIPS 1: INFILE     'FITS:AS723_B020405.xp' Non-blank: disk file name
AIPS 1: NFILES        0                    Number of files to advance
AIPS 1:                                    Also applies to ON-LINE!
AIPS 1: BAND       ' '                     Freq. band (4,P,L,C,X,U,K,Q)
AIPS 1: QUAL         -1                    Source qualifier -1=>all
AIPS 1: CALCODE    ' '                     Calibrator code
AIPS 1: VLAOBS     ' '                     VLA obs. pgm. name ('AZ99')
AIPS 1: VLAMODE    ' '                     VLA obs. mode ('  '=any)
AIPS 1: REFDATE    ' '                     Reference date. 'yyyymmdd'
AIPS 1: TIMERANG   *all 0                  Timerange selected
AIPS 1: BCHAN         1                    First spectral channel
AIPS 1: ECHAN         0                    Highest spectral channel
AIPS 1: OUTNAME    ' '                     Output UV file name (name)
AIPS 1: OUTSEQ        0                    Output UV file name (seq. #)
AIPS 1: OUTDISK       1                    Output UV file disk unit #.
AIPS 1: DOUVCOMP      1                    1 (T) => compressed data
AIPS 1: DOALL        -1                    1 (T) => write all data.
AIPS 1: DOCONCAT     -1                    1 (T) => append data to old
AIPS 1:                                    files
AIPS 1: NCOUNT        2                    Number of files to read
AIPS 1: DOWEIGHT      1                    Use nominal sensitivity to
AIPS 1:                                    scale weights?
AIPS 1:                                    = 10, use Memo 108 weights
```

```
AIPS 1: DOACOR       -1                  Load autocorrelation data?
AIPS 1: CPARM      *all 0                User options.
AIPS 1:                                  1 => Avg. time (seconds)
AIPS 1:                                  2 => bitmap    (see help)
AIPS 1:                                       = 16 for planets & Sun
AIPS 1:                                  3 => Max. OK IF status
AIPS 1:                                       <=3 => 3
AIPS 1:                                  4 => Control dropping of
AIPS 1:                                       shadowed data
AIPS 1:                                       < 0 => no shadow check
AIPS 1:                                       0 => 25 m limit
AIPS 1:                                       > 0 => Shadow limit is
AIPS 1:                                             CPARM(4) in meters
AIPS 1:                                  5 = channel code (see HELP)
AIPS 1:                                  6 => Subarray number-see HELP
AIPS 1:                                  7 => FQ entry tolerance (kHz)
AIPS 1:                                       (see HELP)
AIPS 1:                                  8 => CL table time incr. min
AIPS 1:                                  9 => TY table time incr. min
AIPS 1:                                  10=> Calibrator avg. time
AIPS 1: DPARM      *all 0                Selection by Frequency
AIPS 1:                                  1+2 => A Frequency (Hz)
AIPS 1:                                  3+4 => B Frequency (Hz)
```

```
AIPS 1:                                    5+6 => C Frequency (Hz)
AIPS 1:                                    7+8 => D Frequency (Hz)
AIPS 1:                                    9 => tolerance for A&C
AIPS 1:                                    10 => tolerance for B&D
AIPS 1: BPARM      *all 0                  Opacity and Gain curve
AIPS 1:                                    control (see help)
AIPS 1: IN2FILE    *all ' '                Antenna gains file
```

For the most part, the default parameters can be used. The exceptions are INFILE (the filename with the end number removed), NFILES (the number of files to advance), and NCOUNT (the number of files to read). As long as all of the files to be read have identical root names, they may be read with one run of FILLM.

Now that the data is in the system, we need a summary of the observation, as well as the configuration information. These are obtained using the tasks LISTR and PRTAN. The former, with appropriate inputs, will provide a scan table listing all of the sources and positions, along with internal designations that will be used in later processing.

An example of LISTR output is shown in Figure A.2. To produce this type of output, the user must set the adverb OPTYP='SCAN'.

The task PRTAN produces detailed information about the relative position of each antenna in the array (displayed in $[x, y, z]$ form, in units of meters), and a diagram of the array showing the antenna designations. The diagram is useful at calibration time, for selecting antennae to calibrate over. A sample output of PRTAN in shown in Figure A.3.

The next step in the process is to do an initial inspection of the data. Even before

```
      aragorn    LISTR(31DEC06)      51               21-JUN-2006   10:13:51               Page    1
File = 20031220    .CH 0  .   1 Vol = 1  Userid =   51
Freq =  4.885100000 GHz   Ncor =  2   No. vis =    215466
Scan summary listing

Scan      Source      Qual  Calcode Sub         Timerange          FrqID   START VIS  END VIS
   1 1331+305        : 0000  A        1  0/11:17:20 -   0/11:22:30     1       1      10375
   2 1331+305        : 0000  A        1  0/11:23:00 -   0/11:25:10     1   10376      14925
   3 1327+434        : 0000  A        1  0/11:26:00 -   0/11:27:00     1   14926      16856
   4 M51             : 0000           1  0/11:27:40 -   0/11:42:30     1   16857      46056
   5 1327+434        : 0000  A        1  0/11:43:10 -   0/11:44:00     1   46057      47981
   6 M51             : 0000           1  0/11:44:40 -   0/11:59:30     1   47982      77181
   7 1327+434        : 0000  A        1  0/12:00:00 -   0/12:01:00     1   77182      79134
   8 M51             : 0000           1  0/12:01:30 -   0/12:16:30     1   79135     108365
   9 1327+434        : 0000  A        1  0/12:17:10 -   0/12:18:00     1  108366     110315
  10 M51             : 0000           1  0/12:18:40 -   0/12:34:30     1  110316     141515
  11 1327+434        : 0000  A        1  0/12:35:10 -   0/12:36:00     1  141516     143465
  12 M51             : 0000           1  0/12:36:40 -   0/12:52:30     1  143466     174640
  13 1327+434        : 0000  A        1  0/12:53:10 -   0/12:54:00     1  174641     176590
  14 M51             : 0000           1  0/12:54:40 -   0/13:10:30     1  176591     207715
  15 1327+434        : 0000  A        1  0/13:11:10 -   0/13:12:10     1  207716     209990
  16 1331+305        : 0000  A        1  0/13:13:30 -   0/13:16:10     1  209991     215466

Source summary
Velocity type = '        '    Definition = '        '

  ID Source           Qual  Calcode RA(2000.0)     Dec(2000.0)   IFlux   QFlux   UFlux   VFlux  No. vis
   1 1331+305        : 0000   A     13:31:08.2879  30:30:32.958   7.462   0.000   0.000   0.000   20401
           IF( 2)                                                7.510   0.000   0.000   0.000
   2 1327+434        : 0000   A     13:27:20.9789  43:26:27.989   0.370   0.000   0.000   0.000   13934
           IF( 2)                                                0.372   0.000   0.000   0.000
   3 M51             : 0000         13:29:52.3870  47:11:43.455   0.000   0.000   0.000   0.000  181131
           IF( 2)                                                0.000   0.000   0.000   0.000

  ID Source           Freq(GHz) Velocity(Km/s) Rest freq (GHz)
   1 All Sources         4.8851         0.0000          0.0000
     IF(  2)             4.8351         0.0000          0.0000

Frequency Table summary
FQID IF#      Freq(GHz)      BW(kHz)   Ch.Sep(kHz)  Sideband
   1   1       4.88510000   25000.0020  15625.0010      1
       2       4.83510000   25000.0020  15625.0010      1
```

Figure A.2 Printed output of AIPS task LISTR with OPTYPE='SCAN'.

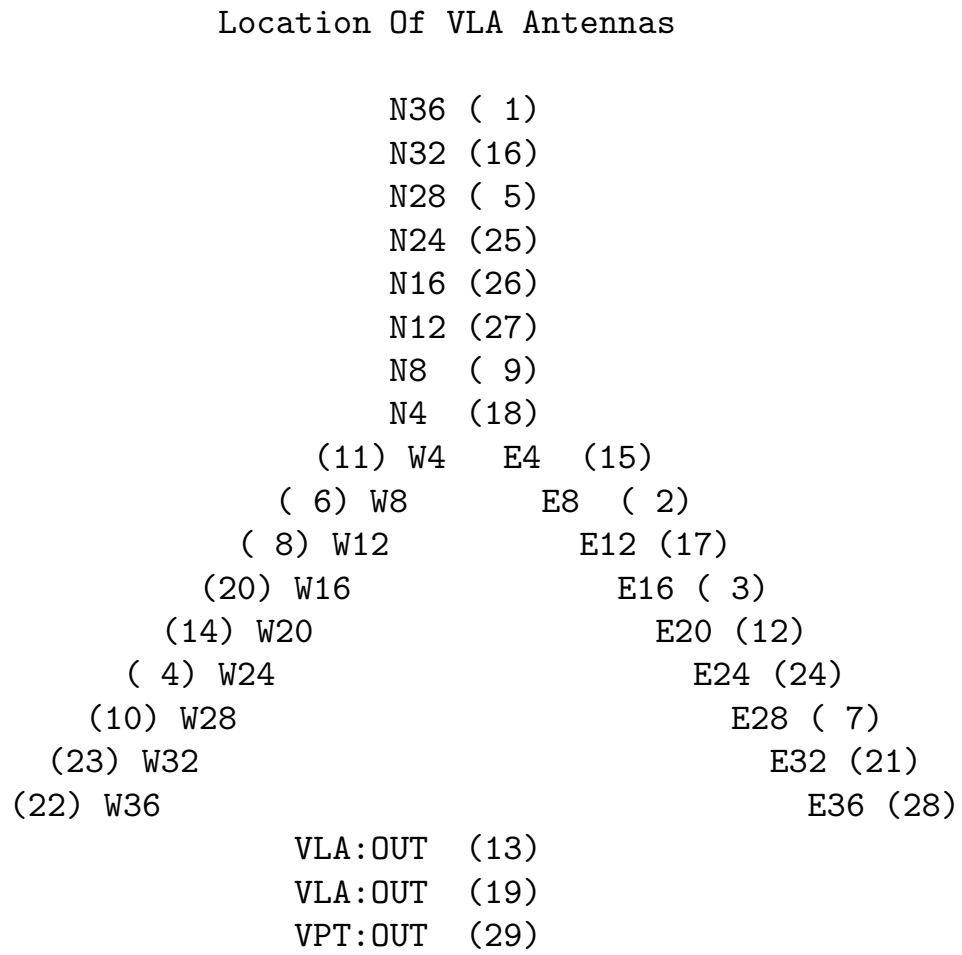



Figure A.3 Antenna layout from PRTAN. The data file this is from is the same as the LISTR output above. The antenna numbers are in parentheses while the associated antenna pad (e.g., N36 for antenna 1) is listed beside it.

calibration there may be obvious bad points in the data. It is not usually necessary to inspect the program source at this point, as any bad data will be apparent after calibration.

Most data inspection and editing can be done with the task TVFLG, an interactive task that allows the user to view the observation in a variety of ways to detect bad data. The most common configuration used in TVFLG is the "Baseline-Time" order. An example of screen shot of a TVFLG session is shown in Figure A.4.

After editing the data on the calibrators, we may begin the process of calibrating the antenna gains in order to create an accurate radio map of the program source. The first step is to establish the flux scale on a known, well-observed flux calibrator source. These sources are typically bright ($>$ 1 Jy), and compact enough to be point-like. The most common primary calibrators are 3C 286 and 3C 48 for VLA observations. In the southern hemisphere, the source PKS 1934-638 is the most common. Flux calibrators are observed for a few minutes at the beginning of an observation, and if the session is considerably long, one more time either in the middle or the end of the observing run.

The task used to set the flux scale is SETJY. Has contains a set of calibrator models that are used to determine the flux value of the primary calibrator that depends on the array configuration, observing band, and epoch of observation. The history file listed in the next section shows the typical parameters used in an SETJY run.

The next step in the process is to actually compute antenna gain corrections for each calibrator. This is achieved using the task CALIB, or the procedure VLACALIB (which contains a set of modest defaults that are useful for VLA data). The user must be careful to only use data that would yield a point source profile for the source being calibrated. This is achieved through setting limits on the *uv* coverage, and excluding antennae outside

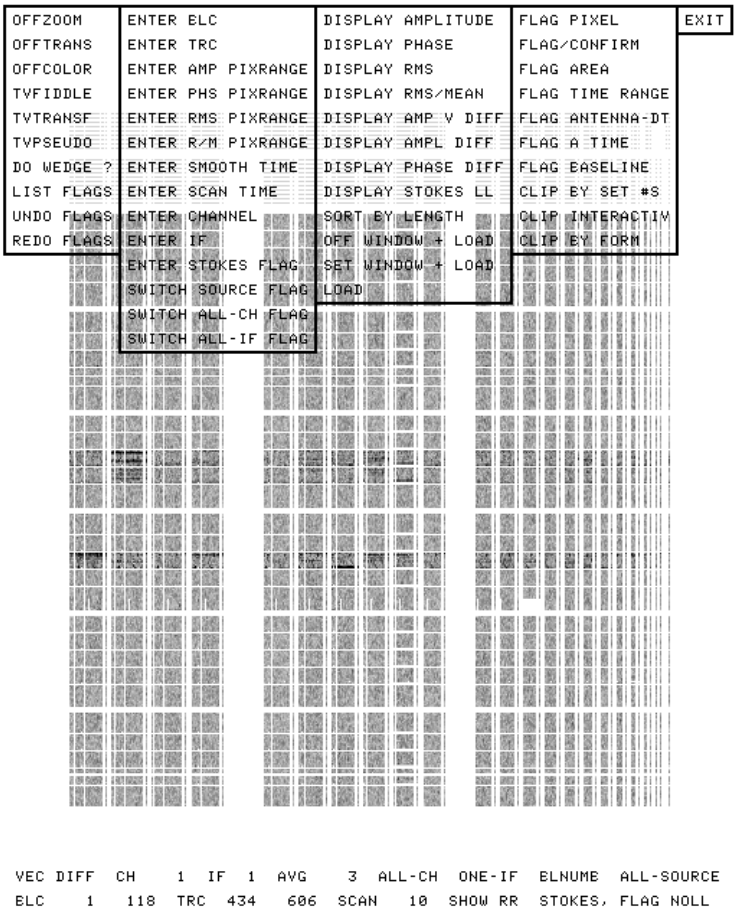



Figure A.4 An example of a TVFLG run. The menu (in the boxes) and status lines (at the bottom) are displayed in a graphics plane which is normally colored light green. Data along the horizontal axis is baseline order, and time runs from bottom to top. The horizontal gaps in the display are times when the telescope was slewing to a new pointing position. The vertical bars correspond to baselines associated with each antenna, beginning with 01-02 (antenna 1 to antenna 2). Each bar is narrower as to prevent over counting of baselines.

of a distance from the center of the array. Calibrators that have the same constraint requirements may be used a single run of CALIB. Each calibrator with different constraints must be processed in separate runs.

After satisfactory gain solutions are obtained, the flux scale needs to be bootstrapped to the secondary calibrator, which will be used to transfer the flux scale to the program source. The task that is used to accomplish this is GETJY. See the history for the result of this task.

Finally, all of the gain solutions must be collected so that they may be applied to the individual sources for imaging. This is done through the creation of a CL table, using CLCAL. The CL table is used for viewing the calibrated data during secondary inspection, and is also used to apply the gain solutions when creating images from the multi-source data set.

After the initial calibration is complete, it is time to inspect the calibration solution. The task that provides the quickest look, is UVPLT.

If the solutions are not satisfactory in the calibration sources, then the data must be edited further. The user would then return to TVFLG to achieve this. In this case we want to set DOCALIB=1 and GAINUSE=N, where N is the version of the CL table containing the calibration solutions. By doing this, we see only the points that were not calibrated correctly. Once we are satisfied with the editing, we may delete the calibration tables and recalibrate as before. Another inspection of the solutions with UVPLT will, hopefully, show a good calibration.

Finally, we need to apply the calibration to the program source and separate it from the multi-source set. We do this with the task SPLIT.

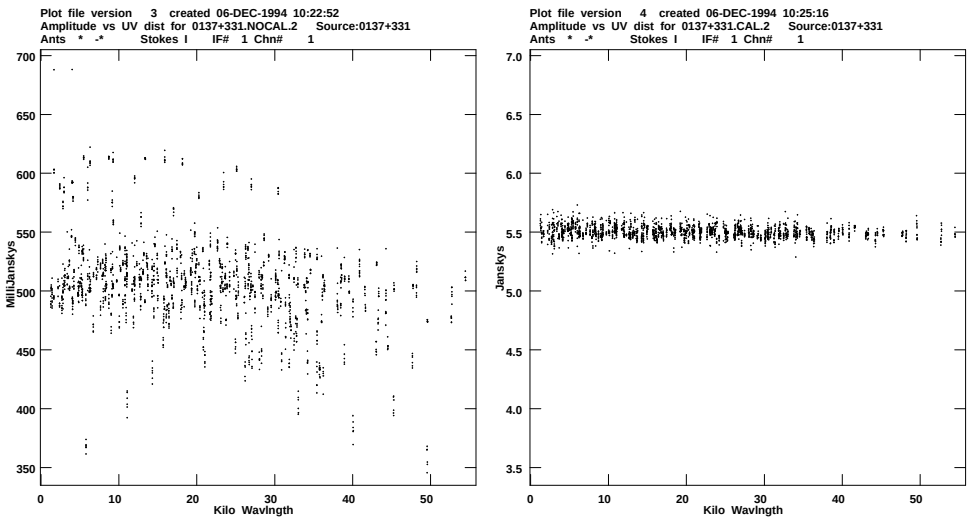



Figure A.5 *(left)* Un-calibrated *uv*-data and *(right)* calibrated *uv*-data from a C-band snapshot of 3C 48. Default VLA gains are a tenth of the actual gains and can show significant scatter. Only wild *uv* points $\sim 50\%$ greater than the average can be detected before calibration.

At this time we may run any of the AIPS imaging routines in order to produce an image. For more information on imaging and deconvolution, I refer the reader to Chapter 5 of the current version of the AIPS Cookbook, provided with any up-to-date AIPS installation.

## A.3 AIPS History File

What follows is the full listing of an AIPS history file from an observation of M51 at 20 cm. The task used is listed at the beginning of each line along with important inputs. In many cases, the default inputs were used, but the user must read the documentation on each task to determine when this is appropriate.

```
aragorn   AIPS (31DEC06)     51     21-JUN-2006  09:57:53    Page    1
```

```
History file for NGC5194     .PBCOR .    1 with    431 entries


 1  ------------------------------------------------------------------
      2  /Begin "HISTORY" information found in fits tape header by IMLOD
      3  BLOCKED =                    T /Tape may be blocked
      4  ------------------------------------------------------------------
      5  /Begin "HISTORY" information found in fits tape header by IMLOD
      6  BLOCKED =                    T /Tape may be blocked
      7  ------------------------------------------------------------------
      8  /Begin "HISTORY" information found in fits tape header by IMLOD
 9  BLOCKED =                    T /Tape may be blocked
10  /------------------------------------------------------------------
11  /Begin "HISTORY" information found in FITS tape header by UVLOD
12  BLOCKED =                    T /Tape may be blocked
13   / Where baseline = 256*ant1 + ant2 + (array#-1)/100
14  FILLM / Image created by user   33 at 06-APR-2002   19:18:23
15  FILLM OUTNAME='AS723.020405'   OUTCLASS='CH 0  '
16  FILLM OUTSEQ=    1   OUTDISK=  7
17  FILLM  INTAPE =  3, NFILES =    0
18  FILLM  BAND = 'L', QUAL =     0,  CALC = '     '
19  FILLM  VLAMODE ='  '
20  FILLM  / Control program ID =
21  FILLM  / VLA conf. = A
```

```
22  FILLM  / correlator mode = 4
23  FILLM  / AP options =
24  FILLM /TIMERANG =    0/00:19:10.00 to    1/10:16:30.00
25  FILLM  TIMERANG =   1.331019E-02  1.428125E+00  / days
26  FILLM  BCHAN =    1 ECHAN =    1 / Spectral channels
27  FILLM  CPARM(1) =  0.000 / Integration (sec)
28  FILLM  CPARM(3) =   3. / Max. IF stat. to pass
29  FILLM  CPARM(4) =   0. / .lt. 0 => no shadow flag
30  FILLM  CPARM(6) =   0. / Subarray
31  FILLM  CPARM(7) =     0.000 / FQ entry tolerance
32  FILLM  CPARM(8) =   5.00 / CL table time increment
33  FILLM  CPARM(9) =   0.00 / TY table time increment
34  FILLM  / Telescope = VLA      Program = AS723
35  FILLM / Weighted with nominal sensitivities
36  FILLM / Data not compressed, no loss of weight info
37  FILLM  RELEASE = '31DEC02 '
38        / Where T means TIME (IAT)
39        / Where B means BASELINE NUM
40  /End FITS tape header "HISTORY" information
41  UVLOD RELEASE= '31DEC02 ' /----------------------------------------
42  UVLOD OUTNAME='AS723.020405'   OUTCLASS='CH 0  '
43  UVLOD OUTSEQ=    1   OUTDISK=  1
44  UVLOD RELEASE= '31DEC02 ' /----------------------------------------
```

```
45  SETJY release ='31DEC02 '  /********* Start 12-JUN-2002   09:19:13
46  SETJY / Flux calculated using known spectrum
47  SETJY BIF =  1 EIF =  2 /Range of IFs
48  SETJY '0137+331        ' IF =  1 FLUX =15.4935 (Jy calcd)
49  SETJY '0137+331        ' IF =  2 FLUX =16.1955 (Jy calcd)
50  SETJY / Using (1999.2) VLA or Reynolds (1934-638) coefficients
51  TVFLG RELEASE ='31DEC02 '  /********* Start 12-JUN-02  10:20:34
52  TVFLG SOURCES='0137+331        '         / Source name included
53  TVFLG /TIMERANG =    0/00:19:15.45 to    0/00:23:15.45
54  TVFLG  TIMERANG =   1.337332E-02  1.615109E-02  / days
55  TVFLG STOKES='HALF'  SUBARRAY=  0
56  TVFLG BIF=   1  EIF=   2     / Range of IF axis
57  TVFLG UVRANGE =   0.00000E+00  1.00000E+10     / Range of uv kilo lambda
58  TVFLG FLAGVER=  1     / FLAG table used
59  TVFLG / All antennas
60  TVFLG / with all antennas
61  TVFLG / Included   20444 points in the grid
62  TVFLG  REASON = 'TVFLG 12-JUN-02 10:20:34'
63  TVFLG RELEASE ='31DEC02 '  /********* Start 12-JUN-02  10:42:13
64  TVFLG SOURCES='1327+434        '         / Source name included
65  TVFLG /TIMERANG =    0/01:28:05.45 to    0/09:01:25.46
66  TVFLG  TIMERANG =   6.117424E-02  3.759891E-01  / days
67  TVFLG STOKES='HALF'  SUBARRAY=  0
```

```
68  TVFLG BIF=   1  EIF=   2     / Range of IF axis
69  TVFLG UVRANGE =   0.00000E+00  1.00000E+10     / Range of uv kilo lambda
70  TVFLG FLAGVER=  1     / FLAG table used
71  TVFLG / All antennas
72  TVFLG / with all antennas
73  TVFLG / Included  169572 points in the grid
74  TVFLG  REASON = 'TVFLG 12-JUN-02 10:42:13'
75  TVFLG RELEASE ='31DEC02 '  /********* Start 12-JUN-02  11:01:50
76  TVFLG SOURCES='NGC5194         '         / Source name included
77  TVFLG /TIMERANG =    0/01:30:05.45 to    0/05:15:15.45
78  TVFLG  TIMERANG =   6.256313E-02  2.189289E-01  / days
79  TVFLG STOKES='HALF'  SUBARRAY=  0
80  TVFLG BIF=   1  EIF=   2     / Range of IF axis
81  TVFLG UVRANGE =   0.00000E+00  1.00000E+10     / Range of uv kilo lambda
82  TVFLG FLAGVER=  1     / FLAG table used
83  TVFLG / All antennas
84  TVFLG / with all antennas
85  TVFLG / Included 1634056 points in the grid
86  TVFLG  REASON = 'TVFLG 12-JUN-02 11:01:50'
87  TVFLG RELEASE ='31DEC02 '  /********* Start 12-JUN-02  11:37:24
88  TVFLG SOURCES='NGC5194         '         / Source name included
89  TVFLG /TIMERANG =    0/05:16:45.45 to    0/08:59:15.46
90  TVFLG  TIMERANG =   2.199705E-01  3.744844E-01  / days
```

```
91  TVFLG STOKES='HALF'  SUBARRAY=  0
92  TVFLG BIF=   1  EIF=   2     / Range of IF axis
93  TVFLG UVRANGE =   0.00000E+00  1.00000E+10     / Range of uv kilo lambda
94  TVFLG FLAGVER=  1     / FLAG table used
95  TVFLG / All antennas
96  TVFLG / with all antennas
97  TVFLG / Included 1166264 points in the grid
98  TVFLG  REASON = 'TVFLG 12-JUN-02 11:37:24'
99  CALIB RELEASE   ='31DEC02 '  /******* Start 12-JUN-2002   11:43:55
100  CALIB N SOURCES=    1 /Following Sources included:
101  CALIB CALSOUR  = '0137+331        ','                '
102  CALIB QUAL     =   -1 CALCODE =
103  CALIB FLAGVER  =    1 /Flagging table used
104  CALIB /TIMERANG = beginning to end
105  CALIB SOLINT   =  144.00 /Soln. inter. (min)
106  CALIB SUBARRAY =    0 REFANT  =   22 /Reference Ant.
107  CALIB APARM(1) =    4 /Min. no antennas
108  CALIB APARM(3) =   -1 />0 => avg. RR,LL
109  CALIB APARM(5) =   -1 />0 => average IFs
110  CALIB APARM(7) =  5.0 /SNR cutoff
111  CALIB SOLTYPE  ='    '/Solution type
112  CALIB SOLMODE  ='A&P '/Solution mode
113  CALIB CPARM(2) =   -1 /1 => Normalize gain
```

```
114  CALIB CPARM(5) =    1 /1 => Scalar average
115  CALIB SNVER    =    1 /Output SN table version
116  CALIB UVRANGE  =    0.000E+00, 4.000E+01 /Min, Max Baseline
117  CALIB /Antennas included:
118  CALIB ANTENNAS = 26  27   9   1  18  19  15  22  23   4  20  11
119  CALIB             8  14   6  21  24  12   2  17   3
120  CALIB ANTWT    =  1.0 /Weight same for all Ant
121  CALIB /Found           80 good solutions
122  CALIB RELEASE   ='31DEC02 '  /******* Start 12-JUN-2002   11:47:27
123  CALIB N SOURCES=    1 /Following Sources included:
124  CALIB CALSOUR  = '1327+434        ',                '
125  CALIB QUAL     =   -1 CALCODE =
126  CALIB FLAGVER  =    1 /Flagging table used
127  CALIB /TIMERANG = beginning to end
128  CALIB SOLINT   =  144.00 /Soln. inter. (min)
129  CALIB SUBARRAY =    0 REFANT  =   22 /Reference Ant.
130  CALIB APARM(1) =    4 /Min. no antennas
131  CALIB APARM(3) =   -1 />0 => avg. RR,LL
132  CALIB APARM(5) =   -1 />0 => average IFs
133  CALIB APARM(7) =  5.0 /SNR cutoff
134  CALIB SOLTYPE  ='    '/Solution type
135  CALIB SOLMODE  ='A&P '/Solution mode
136  CALIB CPARM(2) =   -1 /1 => Normalize gain
```

```
137  CALIB CPARM(5) =    1 /1 => Scalar average
138  CALIB SNVER    =    1 /Output SN table version
139  CALIB UVRANGE  =    6.000E+00, 1.000E+15 /Min, Max Baseline
140  CALIB ANTENNAS =    0 /All antennas selected
141  CALIB ANTWT    =  1.0 /Weight same for all Ant
142  CALIB /Found         1456 good solutions
143  GETJY RELEASE ='31DEC02 '  /********* Start 12-JUN-2002   11:49:21
144  GETJY INNAME='AS723.020405'   INCLASS='CH 0  '
145  GETJY INSEQ=    1   INDISK=  1
146  GETJY  /Sources included:
147  GETJY  SOURCES = '1327+434        ','                '
148  GETJY  SOUCODE ='    ' /Source Cal code
149  GETJY  /Calibrators included:
150  GETJY  CALSOUR = '0137+331        ','                '
151  GETJY  QUAL =    0 CALCODE =
152  GETJY  BIF =   1, EIF =   2 / IF range
153  GETJY /TIMERANG = beginning to end
154  GETJY  SUBARRAY =   0
155  GETJY  ANTENNAS = 0     /All antennas selected
156  GETJY  SNVER =    1 /SN version, 0=> all
157  CLCAL RELEASE ='31DEC02 '  /********* Start 12-JUN-2002   11:52:40
158  CLCAL OPCODE ='CALI' / MERG, CALI or SMOO
159  CLCAL  /Sources included:
```

```
160  CLCAL SOURCES = '1327+434        ','NGC5194         '
161  CLCAL           ,'0137+331       ','                '
162  CLCAL SOUCODE ='    ' /Source Cal code
163  CLCAL  /Calibrators included:
164  CLCAL CALSOUR = '1327+434        ','0137+331        '
165  CLCAL QUAL =   -1 CALCODE = '    '
166  CLCAL /TIMERANG = beginning to end
167  CLCAL SUBARRAY =   0
168  CLCAL ANTENNAS = 0     /All antennas selected
169  CLCAL SNVER =    1 /SN version, 0=> all
170  CLCAL GAINVER =  1, GAINUSE =  2 / CL table
171  CLCAL INTERPOL = '2PT ' / Interpolation type
172  CLCAL INTPARM =    0.00000   0.00000   0.00000 / Interpolation parms
173  CLCAL CUTOFF =  0.0 minutes / Interpolation limit
174  CLCAL SMOTYPE = '    ' / Data to be smoothed
175  CLCAL REFANT =   22 / Reference antenna used
176  TVFLG RELEASE ='31DEC02 '  /********* Start 12-JUN-02  13:47:54
177  TVFLG SOURCES='NGC5194         '         / Source name included
178  TVFLG /TIMERANG =    0/06:50:55.45 to    0/08:59:15.46
179  TVFLG  TIMERANG =   2.853641E-01  3.744844E-01  / days
180  TVFLG STOKES='HALF'  SUBARRAY=  1
181  TVFLG BIF=   1  EIF=   2     / Range of IF axis
182  TVFLG UVRANGE =   0.00000E+00  1.00000E+10     / Range of uv kilo lambda
```

```
183  TVFLG FLAGVER=  1     / FLAG table used
184  TVFLG GAINUSE=  2     / CL table used
185  TVFLG / All antennas
186  TVFLG / with all antennas
187  TVFLG / Included  917816 points in the grid
188  TVFLG  REASON = 'TVFLG 12-JUN-02 13:47:54'
189  TVFLG RELEASE ='31DEC02 '  /********* Start 12-JUN-02  14:03:36
190  TVFLG SOURCES='NGC5194         '         / Source name included
191  TVFLG /TIMERANG =    0/07:55:35.45 to    0/08:59:15.46
192  TVFLG  TIMERANG =   3.302715E-01  3.744844E-01  / days
193  TVFLG STOKES='HALF'  SUBARRAY=  1
194  TVFLG BIF=   1  EIF=   2     / Range of IF axis
195  TVFLG UVRANGE =   0.00000E+00  1.00000E+10     / Range of uv kilo lambda
196  TVFLG FLAGVER=  1     / FLAG table used
197  TVFLG GAINUSE=  2     / CL table used
198  TVFLG / All antennas
199  TVFLG / with all antennas
200  TVFLG / Included  460880 points in the grid
201  TVFLG  REASON = 'TVFLG 12-JUN-02 14:03:36'
202  SPLIT RELEASE ='31DEC02 '  /********* Start 12-JUN-2002   14:09:29
203  SPLIT INNAME='AS723.020405'   INCLASS='CH 0  '
204  SPLIT INSEQ=    1   INDISK=  1
205  SPLIT OUTNAME='NGC5194     '   OUTCLASS='SPLIT '
```

```
206  SPLIT OUTSEQ=    1   OUTDISK=  1
207  SPLIT /TIMERANG = beginning to end
208  SPLIT STOKES = '    ' / Stokes type
209  SPLIT BIF =   1, EIF =   2/ IF range
210  SPLIT BCHAN =   1, ECHAN =   1/ Chan range
211  SPLIT SUBARRAY =   0
212  SPLIT FLAGVER=   1  / Edited using FG table version #
213  SPLIT / Output data in compressed format
214  SPLIT GAINUSE =  2 / CL table
215  SPLIT / Weights not calibrated
216  SPLIT /            Previously flagged   flagged by gain         kept
217  SPLIT / Partially           61575                   0          61575
218  SPLIT / Fully                   0                   0         630309
219  UVPLT  VERSION=  1  / plot file created 13-JUN-2002 17:26:01
220  UVPLT  VERSION=  2  / plot file created 13-JUN-2002 17:26:18
221  UVPLT  VERSION=  3  / plot file created 13-JUN-2002 17:26:51
222  IMAGR RELEASE ='31DEC02 '  /********* Start 14-JUN-2002   03:21:13
223  IMAGR INNAME ='NGC5194'
224  IMAGR INCLASS ='SPLIT'
225  IMAGR INSEQ =       1
226  IMAGR QUAL =      -1
227  IMAGR SELBAND =-1.00000E+00
228  IMAGR SELFREQ =-1.00000E+00
```

```
229  IMAGR FREQID =      -1
230  IMAGR DOPOL =      -1
231  IMAGR BLVER =      -1
232  IMAGR FLAGVER =       1
233  IMAGR DOBAND =      -1
234  IMAGR BPVER =      -1
235  IMAGR STOKES ='I'
236  IMAGR BCHAN =       1
237  IMAGR ECHAN =       1
238  IMAGR NCHAV =       1
239  IMAGR CHINC =       1
240  IMAGR BIF =       1
241  IMAGR EIF =       2
242  IMAGR OUTNAME ='NGC5194'
243  IMAGR CELLSIZE(  1) = 3.00000E-01
244  IMAGR CELLSIZE(  2) = 3.00000E-01
245  IMAGR NFIELD =      55
246  IMAGR UVRANGE(  1) = 7.00000E+00
247  IMAGR UVBXFN =       1
248  IMAGR XTYPE =       5
249  IMAGR YTYPE =       5
250  IMAGR OVERLAP =       2
251  IMAGR NGAUSS =       1
```

```
252  IMAGR ROBUST =   0.000 / Weighting robustness parm
253  IMAGR NITER =   50000
254  IMAGR GAIN = 1.00000E-01
255  IMAGR MINPATCH =     121
256  IMAGR IMSIZE(*, 1)  =  2048 ,  2048
257  IMAGR FLDSIZE(*, 1) =  2036 ,  2036
258  IMAGR RASHIFT( 1)   =  6.95254E-11
259  IMAGR DECSHIFT( 1)  =  2.55795E-11
260  IMAGR NBOXES( 1)    = **
261  IMAGR WIN(*, 1, 1) =  208,  736,  262,  796
262  IMAGR WIN(*, 2, 1) =   -1,   12,  403,  823
263  IMAGR WIN(*, 3, 1) =   -1,   12,  604,  802
264  IMAGR WIN(*, 4, 1) =   -1,   12,  694,  649
265  IMAGR WIN(*, 5, 1) =   -1,   12,  949,  562
266  IMAGR WIN(*, 6, 1) = 1306,  751, 1330,  775
267  IMAGR WIN(*, 7, 1) =   -1,    9, 1525, 1105
268  IMAGR WIN(*, 8, 1) =  775,  916,  796,  934
269  IMAGR WIN(*, 9, 1) =   -1,    9,  727, 1255
270  IMAGR WIN(*,10, 1) = 1036, 1216, 1069, 1243
271  IMAGR WIN(*,11, 1) =   -1,   12, 1135, 1222
272  IMAGR WIN(*,12, 1) = 1057, 1102, 1072, 1120
273  IMAGR WIN(*,13, 1) = 1057, 1078, 1075, 1093
274  IMAGR WIN(*,14, 1) = 1087, 1051, 1108, 1072
```

```
IMAGR WIN(*,15, 1) = 1075, 1060, 1096, 1084
IMAGR WIN(*,16, 1) = 1114,  967, 1126,  994
IMAGR WIN(*,17, 1) = 1099,  967, 1117, 1024
IMAGR WIN(*,18, 1) = 1099,  952, 1117,  967
IMAGR WIN(*,19, 1) = 1111,  946, 1126,  964
IMAGR WIN(*,20, 1) = 1009, 1006, 1036, 1033
IMAGR WIN(*,21, 1) = 1003, 1036, 1054, 1075
IMAGR WIN(*,22, 1) = 1045,  991, 1066, 1024
IMAGR WIN(*,23, 1) =  913, 1024,  925, 1042
IMAGR WIN(*,24, 1) =  919, 1009,  934, 1033
IMAGR WIN(*,25, 1) =  931,  988,  946, 1021
IMAGR WIN(*,26, 1) =  940,  970,  958, 1009
IMAGR WIN(*,27, 1) =  910, 1048,  925, 1072
IMAGR WIN(*,28, 1) = 1072, 1126, 1099, 1138
IMAGR WIN(*,29, 1) =   -1,    9, 1279,  673
IMAGR WIN(*,30, 1) =   -1,   12,  790, 1480
IMAGR WIN(*,31, 1) =   -1,   15,  928, 1489
IMAGR WIN(*,32, 1) = 1117, 1474, 1153, 1492
IMAGR WIN(*,33, 1) =   -1,    9, 1285, 1390
IMAGR WIN(*,34, 1) =   -1,   12, 1783, 1252
IMAGR WIN(*,35, 1) =  775, 1864,  820, 1897
IMAGR WIN(*,36, 1) = 1165, 1162, 1183, 1180
IMAGR WIN(*,37, 1) = 1015,  946, 1033,  961
```

```
298  IMAGR WIN(*,38, 1) =   -1,    9, 1723,  961
299  IMAGR WIN(*,39, 1) =   -1,   12,  934, 1087
300  IMAGR WIN(*,40, 1) =   -1,   12, 1147, 1276
301  IMAGR WIN(*,41, 1) =   -1,    9,  409,  619
302  IMAGR WIN(*,42, 1) =  967,  979,  982,  991
303  IMAGR WIN(*,43, 1) =  997, 1207, 1015, 1225
304  IMAGR WIN(*,44, 1) = 1228, 1102, 1276, 1114
305  IMAGR WIN(*,45, 1) = 1222, 1111, 1267, 1132
306  IMAGR WIN(*,46, 1) =  919, 1108,  940, 1129
307  IMAGR WIN(*,47, 1) = 1039,  958, 1057,  985
308  IMAGR WIN(*,48, 1) =  880,  826,  928,  853
309  IMAGR WIN(*,49, 1) =  847,  880,  865,  898
310  IMAGR WIN(*,50, 1) =  718, 1069,  739, 1087
311  IMAGR WIN(*,51, 1) =  742, 1000,  763, 1018
312  IMAGR WIN(*,52, 1) =  733, 1051,  751, 1072
313  IMAGR WIN(*,53, 1) =  736, 1288,  766, 1321
314  IMAGR WIN(*,54, 1) =  517, 1351,  532, 1366
315  IMAGR WIN(*,55, 1) = 1210, 1411, 1228, 1426
316  IMAGR WIN(*,56, 1) =   -1,    9,  880, 1408
317  IMAGR WIN(*,57, 1) = 1087, 1429, 1111, 1441
318  IMAGR WIN(*,58, 1) =  637, 1786,  649, 1804
319  IMAGR WIN(*,59, 1) =  373, 1126,  397, 1141
320  IMAGR WIN(*,60, 1) = 1468,  406, 1492,  433
```

```
321  IMAGR WIN(*,61, 1) =  766, 1318,  805, 1360
322  IMAGR WIN(*,62, 1) =  943, 1150,  967, 1171
323  IMAGR WIN(*,63, 1) = 1234, 1048, 1279, 1099
324  IMAGR WIN(*,64, 1) = 1297,  949, 1321, 1036
325  IMAGR WIN(*,65, 1) = 1039,  850, 1063,  886
326  IMAGR WIN(*,66, 1) = 1192, 1135, 1243, 1156
327  IMAGR WIN(*,67, 1) =  781,  958,  808, 1030
328  IMAGR WIN(*,68, 1) = 1081, 1453, 1114, 1492
329  IMAGR WIN(*,69, 1) =  859,  844,  910,  880
330  IMAGR WIN(*,70, 1) =  598, 1276,  625, 1303
331  IMAGR WIN(*,71, 1) =  706, 1153,  730, 1213
332  IMAGR WIN(*,72, 1) = 1009, 1075, 1057, 1111
333  IMAGR WIN(*,73, 1) = 1078,  904, 1117,  934
334  IMAGR WIN(*,74, 1) =  706, 1087,  739, 1129
335  IMAGR WIN(*,75, 1) =  994, 1024, 1009, 1075
336  IMAGR WIN(*,76, 1) = 1036, 1024, 1060, 1033
337  IMAGR WIN(*,77, 1) = 1027,  991, 1048, 1033
338  IMAGR WIN(*,78, 1) = 1081, 1012, 1099, 1039
339  IMAGR WIN(*,79, 1) = 1141, 1168, 1168, 1189
340  IMAGR WIN(*,80, 1) = 1021,  835, 1042,  865
341  IMAGR WIN(*,81, 1) =  928,  823,  949,  847
342  IMAGR WIN(*,82, 1) =  721, 1210,  742, 1243
343  IMAGR WIN(*,83, 1) =  274, 1129,  289, 1147
```

```
344  IMAGR WIN(*,84, 1) =  976,  658,  991,  670
345  IMAGR WIN(*,85, 1) =  949, 1066,  970, 1096
346  IMAGR WIN(*,86, 1) = 1093, 1027, 1117, 1060
347  IMAGR WIN(*,87, 1) =  961,  949,  985,  973
348  IMAGR WIN(*,88, 1) = 1105, 1204, 1141, 1222
349  IMAGR WIN(*,89, 1) = 1240,  772, 1261,  787
350  IMAGR WIN(*,90, 1) =  640,  529,  664,  556
351  IMAGR WIN(*,91, 1) =   -1,   12,  550,  538
352  IMAGR WIN(*,92, 1) =   -1,   12,  937, 1468
353  IMAGR WIN(*,93, 1) =   -1,   12,  754, 1252
354  IMAGR WIN(*,94, 1) =  949, 1165,  985, 1186
355  IMAGR WIN(*,95, 1) =  970, 1180, 1012, 1210
356  IMAGR WIN(*,96, 1) =   -1,    9,  556,  721
357  IMAGR WIN(*,97, 1) =   -1,    9,  112, 1333
358  IMAGR WIN(*,98, 1) =   -1,    9,  628, 1477
359  IMAGR WIN(*,99, 1) =   -1,    9,  862,  811
360  IMAGR WIN(*,**, 1) =   -1,   12, 1231,  361
361  IMAGR WIN(*,**, 1) =   -1,    9,  898,  574
362  IMAGR WIN(*,**, 1) =   -1,   12,  661,  619
363  IMAGR WIN(*,**, 1) =   -1,   12, 1531,  280
364  IMAGR WIN(*,**, 1) =   -1,   12,  814, 1513
365  IMAGR WIN(*,**, 1) =   -1,   12,  907, 1513
366  IMAGR WIN(*,**, 1) =   -1,   12,  955, 1207
```

```
IMAGR WIN(*,**, 1) =   -1,   12, 1096,  631
IMAGR NCOMP( 1) =    5905
IMAGR TFLUX =  2.24716E-01         / Total cleaned flux
IMAGR CFLUX( 1) =  1.09797E-01     / Cleaned flux in field
STARS  Version=  1 Lines=    1  / Star file created 14-JUN-2002 08:16:39
/END FITS tape header "HISTORY" information
----------------------------------------------------------------
IMLOD OUTNAME ='
IMLOD OUTSEQ =    0     INTAPE = 1     OUTDISK= 3
IMLOD INFILE = 'FITS:GANDALF/NGC5194.ICL001.2                    '
IMLOD RELEASE = '31DEC00'
KNTR   VERSION=  1  / plot file created 28-JUN-2002 11:16:07
KNTR   VERSION=  2  / plot file created 28-JUN-2002 11:16:52
KNTR   VERSION=  3  / plot file created 28-JUN-2002 11:18:59
KNTR   VERSION=  4  / plot file created 28-JUN-2002 11:19:38
KNTR   VERSION=  5  / plot file created 28-JUN-2002 11:23:21
STARS  Version=  2 Lines=    1  / Star file created 15-JUL-2002 15:48:56
GREYS  VERSION=  6  / plot file created 23-JAN-2004 14:00:35
GREYS  VERSION=  7  / plot file created 23-JAN-2004 15:25:33
GREYS  VERSION=  7  / plot file created 23-JAN-2004 15:26:13
KNTR   VERSION=  8  / plot file created 26-JAN-2004 13:52:30
KNTR   VERSION=  9  / plot file created 26-JAN-2004 13:54:32
KNTR   VERSION= 10  / plot file created 26-JAN-2004 13:54:59
```

```
390  KNTR   VERSION=  8  / plot file created 26-JAN-2004 13:59:43
391  /END FITS tape header "HISTORY" information
392  ------------------------------------------------------------------
393  IMLOD OUTNAME =’
394  IMLOD OUTSEQ =    0     INTAPE = 1     OUTDISK= 3
395  IMLOD INFILE = ’FITS:M51.ICL001.2                                  ’
396  IMLOD RELEASE = ’31DEC05’
397  PBCOR RELEASE =’31DEC05 ’  /********* Start 23-AUG-2005   16:05:04
398  PBCOR INNAME=’NGC5194     ’   INCLASS=’ICL001’
399  PBCOR INSEQ=    0   INDISK=  3
400  PBCOR OUTNAME=’NGC5194     ’   OUTCLASS=’PBCOR ’
401  PBCOR OUTSEQ=    0   OUTDISK=  3
402  PBCOR  BLC=   1,   1,   1,  1,  1, 1, 1 TRC=2048,2048,   1,  1,  1, 1, 1
403  PBCOR  PRA=  13 29 52.700  PDec=  47 11 43.00
404  PBCOR  Beamcut=  0.10000   /Clip outside this beam value
405  PBCOR  / Beam =  1.000000E+00 +     / Beam  model
406  PBCOR  /        -1.343000E+00 * X +
407  PBCOR  /         6.579000E+00 * X*X +
408  PBCOR  /        -1.186000E+00 * X*X*X +
409  PBCOR  /         0.000000E+00 * X*X*X*X
410  PBCOR  /         0.000000E+00 * X*X*X*X*X
411  PBCOR  / Where X = [Angle(arcmin) * f(GHz)]**2
412  AIPS   IMNAME=’NGC5194     ’ IMCLASS=’PBCOR ’ IMSEQ=   1     /
```

```
413  AIPS   USERNO=    2           /
414    FITS (Flexible Image Transport System) format is defined in 'Astronomy
415    and Astrophysics', volume 376, page 359; bibcode: 2001A&A...376..359H
416  AIPS   CLEAN BMAJ=  4.1720E-04 BMIN=  3.3519E-04 BPA=  78.05
417  AIPS   CLEAN NITER=     5905 PRODUCT=1   / NORMAL
418  /END FITS tape header "HISTORY" information
419  ----------------------------------------------------------------------
420  IMLOD OUTNAME ='
421  IMLOD OUTSEQ =    0     INTAPE = 1     OUTDISK= 2
422  IMLOD INFILE = 'FITS:M51.PBCOR.1                                    '
423  IMLOD RELEASE = '31DEC06'
424  STARS  Version=  3 Lines=   13  / Star file created 02-JAN-2006 08:55:34
425  KNTR   VERSION=  1  / plot file created 02-JAN-2006 09:04:42
426  KNTR   VERSION=  2  / plot file created 02-JAN-2006 09:05:07
427  KNTR   VERSION=  3  / plot file created 02-JAN-2006 09:09:30
428  KNTR   VERSION=  4  / plot file created 02-JAN-2006 09:11:13
429  KNTR   VERSION=  5  / plot file created 02-JAN-2006 09:12:58
430  KNTR   VERSION=  6  / plot file created 02-JAN-2006 09:14:03
431  STARS  Version=  4 Lines=  112  / Star file created 27-MAR-2006 11:09:42
```

## Appendix B

# The *Chandra* X-ray Observatory

The treatment given here for the *Chandra* X-ray Observatory was generously provided by Roy Kilgard and further information can be obtained in Kilgard (2006). The *Chandra* X-ray Observatory is the third mission of four in the *NASA* Great Observatories program, whose aim was to cover many different wavelengths with simultaneous space-based observatories. The other missions are the *Hubble Space Telescope*, the *Compton Gamma Ray Observatory* (now defunct), and the *Spitzer Space Telescope*. *Chandra* was launched on 23 July, 1999 by *NASA*'s space shuttle Columbia and placed into a highly elliptical orbit by n inertial upper stage booster. *Chandra* features two primary focal plane instruments: *ACIS*, the Advanced CCD Imaging Spectrometer, and *HRC*, the High Resolution Camera. The X-ray data discussed in this dissertation used the *ACIS* instrument, so *HRC* will not be discussed in this appendix. A schematic of the observatory is presented in Figure B.1.

*Chandra* is in a highly elliptical 64 hr orbit with perigee at 16,000 km and apogee at 160,000 km. This allows for a maximum amount of time above the radiation belts for continuous observing of up to 55 hr and overall observing efficiency of around 70%.

The most outstanding feature of *Chandra* is the HRMA, or mirror assembly. The Wolter type grazing incidence reflection mirrors (see Figure B.2) are the most precisely polished mirrors ever constructed. The *Chandra* HRMA allows for resolution of objects smaller than $0.5''$. Combined with the excellent aspect solution *Chandra*, source positions can be determined with absolute astrometric accuracy to better than $0.3''$, which is comparable to

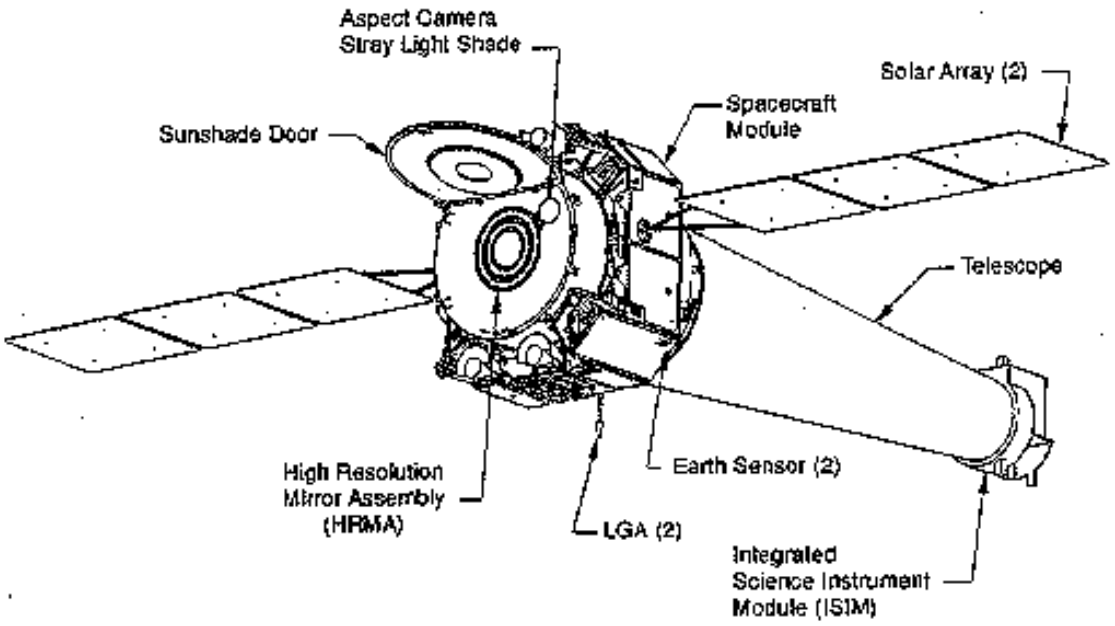



Figure B.1 The *Chandra* Observatory with certain subsystems labeled. LGA is an acronym for the Low Gain Antenna. From the *Chandra* Proposer's Observatory Guide, v8.0.

that achieved with the *Hubble Space Telescope*.

## B.1 *ACIS*: the Advanced CCD Imaging Spectrometer

The *ACIS* instrument consists of two separate CCD arrays: the *ACIS-I*, intended for imaging, and the *ACIS-S*, intended for dispersed grating spectroscopy (Figure B.3). Each array is made of $1024 \times 1024$ pixel CCDs; four arranged in a $2 \times 2$ grid (*ACIS-I*). Any combination of up to 6 CCDs may be read out simultaneously. In imaging mode, the default is to read out chips I0–I3 and S2–S3 for *ACIS-I* and chips I2–I3 and S1–S4 for *ACIS-S*. The ACIS pixels are $\sim 0.49'' \times 0.49''$, slightly larger than the on-axis PSF of the HRMA. The PSF degrades with off-axis angle however, due both to the differentiation of CCD layout from the ideal focal surface and to the intrinsic increase in PSF with off-axis angle due to mirror

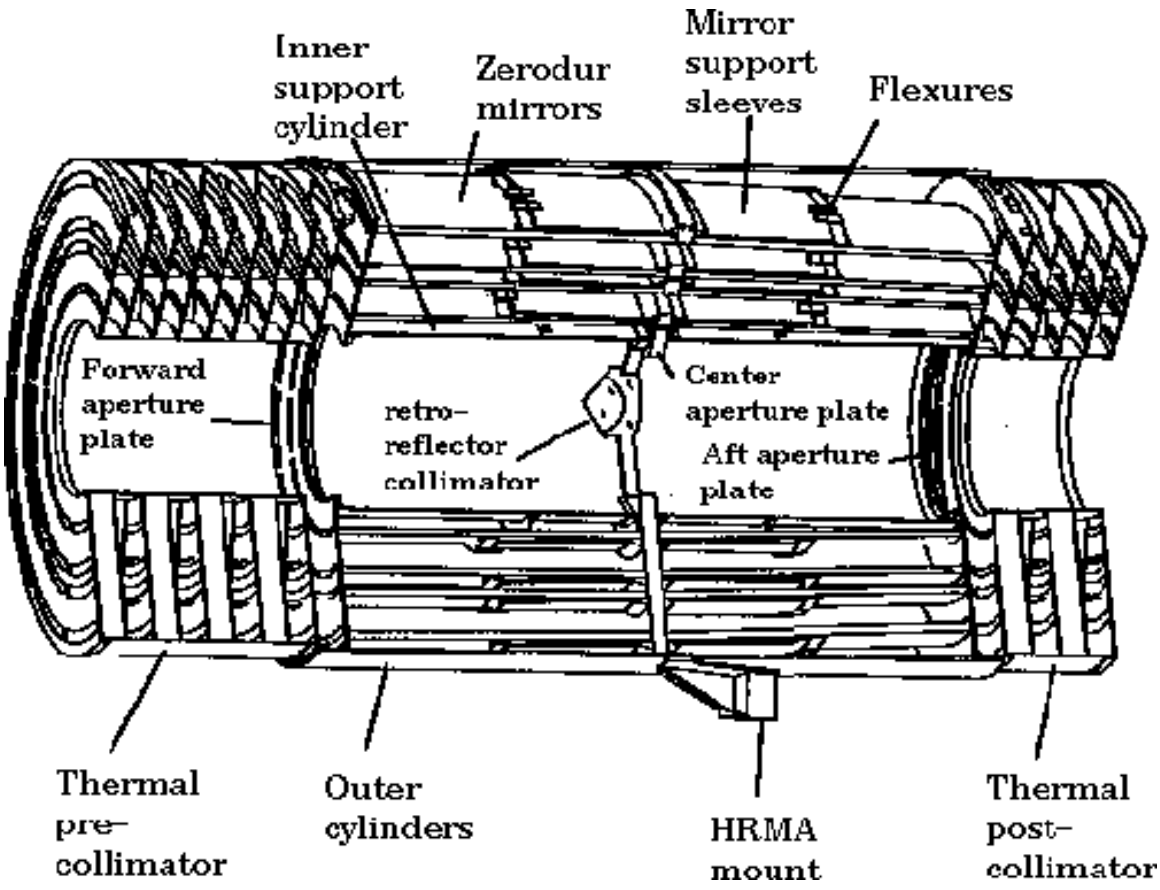



Figure B.2 The *Chandra* High Resolution Mirror Assembly (HRMA) is a set of 4 nested grazing -incidence mirrors. From *Chandra Proposer's Observatory Guide, v.8.0*

# ACIS FLIGHT FOCAL PLANE

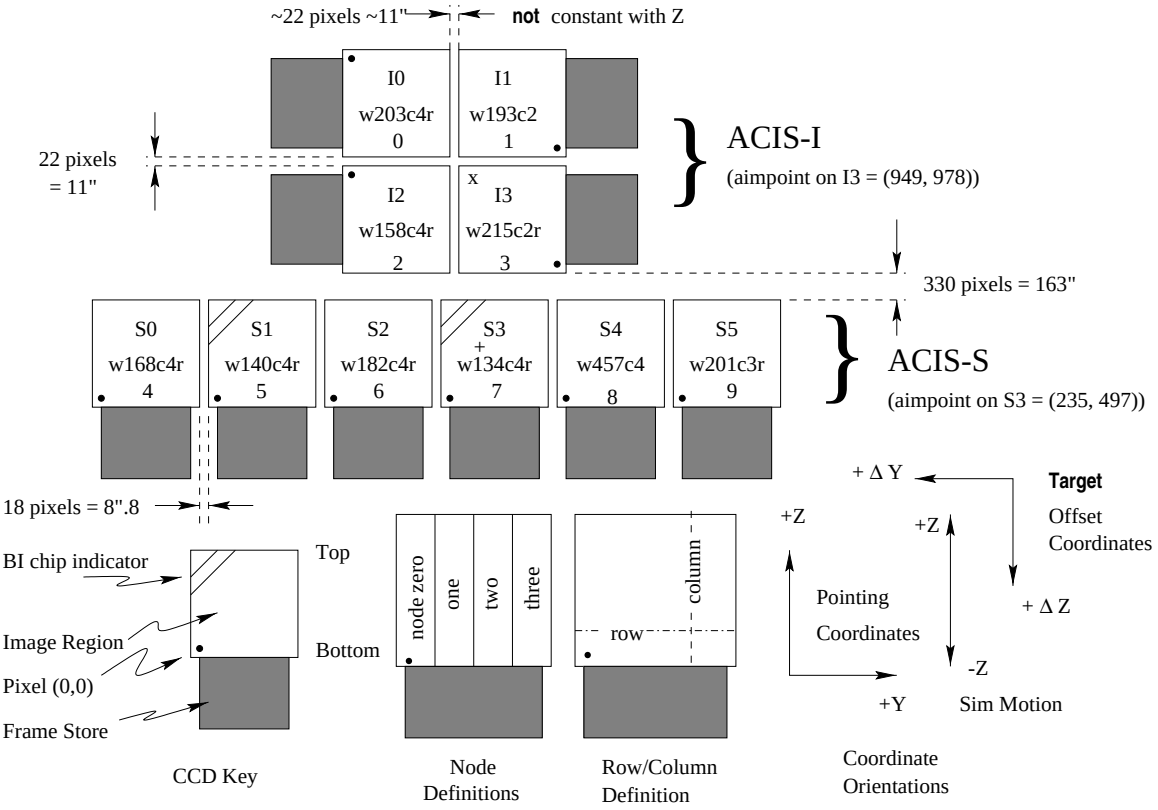



Figure B.3 Diagram of the *ACIS* instrument. At top is the *ACIS-I* array and at bottom the *ACIS-S*. The X and + symbols denote the nominal aimpoints of each array in imaging mode. From POG (2006), figure 6.1

aberrations (it should be noted that the latter is energy dependent).

The CCDs have intrinsic energy resolution determined by measuring the pulse height amplitude of the charge displaced by each incident photon. The calibrated energy range is $\sim 0.3 - 10$ keV, with resolution on the order of $\sim 100$ eV at 1 keV.

The *ACIS* detector has two CCDs which are back-illuminated (BI) and 8 that are front-illuminated (FI). The BI CCDs (chips S1 and S3) have had a treatment applied to the back side of the chip to remove insensitive, bulk silicon and leave the photo-sensitive region

exposed. These chips are then installed with the back of the chip facing the optical bench. This configuration allows for a much higher sensitivity at a low photon energies as compared with the FI CCDs, since less X-rays are absorbed or scattered by the detector material before striking the photo-sensitive surface. Most of the data discussed in this dissertation comes from the *ACIS* S3 chip, though some data makes use of the FI CCDs. As time has progressed, the *ACIS* detector has developed a contaminated build-up on the optical blocking filter. This contaminant severely effects the low-energy effective area of *ACIS*; however, since most of the data discussed here was taken early in the *Chandra* mission, the contamination presents minimal difficulty for our work.

Each *ACIS* CCD has an active region which is exposed to incident photons and an inactive frame store region, which is shielded. After a single exposure (nominally 3.2 s for the full chip), the data is transferred to the frame store in 41 ms. The next exposure the begins and the data transferred from the frame store to a processor that records the position and amplitude of the event along with information from the surrounding pixels (used for grading), and passes the data into the telemetry stream.

One can choose to read out a portion if an *ACIS* chip or chips in a subarray. Since the exposure time is largely dictated by the processing time of events from the frame store, using a subarray allows one to reduce the frame time, and hence increase the timing resolution, of the data. The frame time is given by the following equation:

$$T(\text{ms}) = 41 \times m + 2.84 \times n + 5.2 + 0.040 \times (m \times q) \tag{B.1}$$

where $m$ is the number of active CCDs, $n$ is the number of rows in the subarray, and $q$ is the number of rows separating the subarray from the frame store region.

During on-board processing, each *ACIS* event is assigned a grade using the *ASCA* grading scheme. This method examines the information in the $3 \times 3$ pixel region surrounding the event and utilizes that information to determine whether the event is a real incident photon, a cosmic ray, detector noise, etc. For further details on grading, see the *Chandra* Proposer's Observatory Guide (POG 2006). For each of the *ACIS* modes, one can also choose graded, faint, or very faint telemetry format. The difference between these formats is in what is telemetered to the ground. In very faint mode, a $5 \times 5$ event island is telemetered to the ground rather than the standard $3 \times 3$. This allows the expert user to perform further grade rejection in post-processing but has the disadvantage of requiring more bits of data and therefore cannot be used for very bright sources without risking a saturation of the telemetry stream. Graded mode only transfers the event grade and not the $3 \times 3$ island, so events cannot be regarded on the ground. Graded mode allows for 375.0 events $s^{-1}$, faint mode 170.2 event $s^{-1}$, and very faint mode allows only 68.8 event $s^{-1}$. Nominal operating mode for *ACIS* is TE/Faint mode.

*ACIS* also has a few problems that diverge from optimal operation. These are: pileup, increased charge transfer inefficiency, and contamination. Each will be discussed briefly, as each impacts some of the data to be discussed.

• Pileup occurs when two or more photons are detected in a single pixel during a single frame. The detector cannot register each as a separate event, but rather registers the sum of the charge displaced by each event, roughly equal to the sum of the incident photon energies. This naturally has an impact on the spectrum of the source. The more "piled" photons there are, the harder the spectrum appears.

• The FI CCDs on *ACIS* have had an increase in the charge transfer inefficiency (CTI)

since launch, resulting in a loss of energy resolution. This CTI increase was due to radiation damage caused by low energy protons, encountered when *Chandra* was passing through the Earth's radiation belts. The protons were reflected off the X-ray telescope and onto the focal plane. Once this degradation was discovered, procedures were changed to remove *ACIS* from the focal plane while passing through the radiation zone. The BI CCDs were not affected by the proton flux. A correction for the energy resolution changes has been implemented in the standard data processing and all data discussed herein have been reprocessed to perform this correction.

• Since the *ACIS* CCDs are sensitive to both optical and X-ray photons, optical blocking filters are positioned between the CCDs and the mirrors. Observations of calibration sources have determined that the *ACIS* effective area has been slowly but steadily decreasing since launch. This has now been attributed to a buildup of contamination on the outside (opposite the detector) of the optical blocking filters. The effect is seen primarily at event energies below 1 keV. There are two models for the contamination available to users: one from the *Chandra* Science Center, and the other from Pennsylvania State University, the co-developers of the *ACIS* CCDs. The *Chandra* Science Center model was chosen for this analysis and has been applied to all data discussed herein.

## Appendix C

# Rules of Reasoning in Philosophy

What follows are the rules for natural reasoning as set by Isaac Newton in Book III of the *Principia Mathematica*. These rules govern the process of scientific investigation in all natural science fields. They are included here as a reminder to all of the standard set for scientific pursuits since the seventeenth century.

### Rule I

*We are to admit no more causes of natural things than such as are both true and sufficient to explain their appearances.*

To this purpose the philosophers say that Nature does nothing in vain, and more is in vain when less will serve; for Nature is pleased with simplicity, and affects not the pomp of superfluous causes.

### Rule II

*Therefore to the same natural effects we must, as far as possible, assign the same causes.*

As to respiration in a man and in a beast; the descent of stones in Europe and in America; the light of our culinary fire and of the sun; the reflection of light in the earth, and in the planets.

### Rule III

*The qualities of bodies, which admit neither intensification nor remission of degrees, and which are found to belong to all bodies within the reach of our experiments, are to be*

*esteemed the universal qualities of all bodies whatsoever.*

For since the qualities of bodies are only known to us by experiments, we are to hold for universal all such as universally agree with experiments; and such as are not liable to diminution can never be quite taken away. We are certainly not to relinquish the evidence of experiments for the sake of dreams and vain fictions of our own devising; nor are we to recede from the analogy of Nature, which is wont to be simple, and always consonant to itself. We no other way know the extension of bodies than by our senses, nor do these reach it in all bodies; but because we perceive extension in all that are sensible, therefore we ascribe it universally to all others also. That all bodies are impenetrable, we gather not from reason, but from sensation. The bodies which we handle we find impenetrable, and thence conclude impenetrability to be an universal property of all bodies whatsoever. That all bodies are movable, and endowed with certain powers (which we call inertia) of persevering in their motion, or in their rest, we only infer from the like properties observed in the bodies which we have seen. The extension, hardness, impenetrability, mobility, and inertial of the whole, result from the extension, hardness, impenetrability, mobility, and inertial of the parts; and hence we conclude the least particles of all bodies to be also all extended, and hard and impenetrable, and movable, and endowed with their proper inertia. And this is the foundation of all philosophy. Moreover, that the divided but contiguous particles of bodies may be separated from one another, is matter of observation; and, in the particles that remain undivided, our minds are able to distinguish yet lesser parts, as is mathematically demonstrated. But whether the parts so distinguished and not yet divided, may, by the powers of Nature, be actually divided and separated from one another, we cannot certainly determine. Yet, had we the proof of but one experiment that any undivided particle, in

breaking a hard and solid body, suffered a division, we might by virtue of this rule conclude that the undivided as well as the divided particles may be divided and actually separated to infinity.

Lastly, if it universally appears, by experiments and astronomical observations, that all bodies about the earth gravitate towards the earth, and that in proportion to the quantity of matter which they severally contain; that the moon likewise, according to the quantity of its matter, gravitates towards the earth; that, on the other hand, our sea gravitates towards the moon; and all the planets one towards another; and the comets in like manner towards the sun; we must, in consequence of this rule, universally allow that all bodies whatsoever are endowed with a principle of mutual gravitation. For the argument from the appearances concludes with more force for the universal gravitation of all bodies than for their impenetrability; of which, among those in the celestial regions, we have no experiments, nor any manner of observation. Not that I affirm gravity to be essential to bodies: by their vis insita I mean nothing but their inertia. This is immutable. Their gravity is diminished as they recede from the earth.

## Rule IV

*In experimental philosophy we are to look upon propositions inferred by general induction from phenomena as accurately or very nearly true, notwithstanding any contrary hypotheses that may be imagined, till such time as other phenomena occur, by which they may either be made more accurate, or liable to exceptions.*

This rule we must follow, that the arguments of induction may not be evaded by hypotheses.